Controlled Cellular Perforation by Photoabsorber-Mediated Laser Irradiation: From Targeted Delivery to Selective Ablation

(光吸収体媒介レーザ照射による調整型細胞穿孔：標的デリバリから選択的除去まで)

July, 2025

Doctor of Philosophy (Engineering)

Aniket Mishra

アニケット ミシュラ

Toyohashi University of Technology

Department of Mechanical Engineering	Student ID	D205109	Supervisor	Moeto Nagai Takayuki Shibata
Applicant's name	Aniket Mishra			

Abstract

Controlled laser irradiation methods have emerged as a powerful tool in the field of modern biomedical engineering, offering precise administration of foreign molecules such as genetic material, drugs, and functional proteins in the intracellular microenvironment, changing the phenotype of cells, and enabling selective ablation of cancer cells to offer site-specific cancer therapy. Traditional methods cannot, however, target cells precisely at a site-specific location with high throughput. Photoabsorber-assisted laser irradiation methods overcome these drawbacks by uniquely combining the application of light-absorbing materials for converting light energy from laser to heat to create both temporary and permanent pores on the cell membrane to facilitate intracellular delivery and cell necrosis. This thesis discusses the development of site-specific cell perforation methods for creation of transient and permanent pores on the cell membrane for the application in the field of intracellular delivery, photothermal therapy, and cell patterning.

Chapter 2 presents the development of a micropattern-assisted method to perform controlled intracellular delivery of Fluorescein Isothiocyanate (FITC) Dextran into cells. The system utilizes motorized stages to locate the target site of irradiation. The findings in the chapter highlight the importance of the size of the micropatterns and cell-specific properties in the determination of cellular response to laser-induced shockwave upon irradiation on a microstructure surface. This approach presents a robust distance-dependent method to systematically optimize the shockwave-mediated intracellular delivery, which balances delivery efficiency and cell viability.

Chapter 3 introduces a new approach to parallelize the method introduced in Chapter 2. We used a micropattern on the top setup, which facilitates the intracellular delivery of Fluorescein Isothiocyanate (FITC) Dextran in a massively parallel fashion. The shockwave induced from laser irradiation of the micropattern surface causes bio-effects on cells by creating transient and permanent pores, which results in intracellular

delivery, cell peeling, and cell necrosis. Each of which contributes to either intracellular delivery or cell ablation. We have investigated the effect of varying laser fluence and micropattern pitch on the shockwave response of HeLa cells. This approach highlights the importance of processing parameters for desired outcomes on cells.

Chapter 4 shifts the focus of photoabsorber-assisted laser irradiation methods into the field of photothermal therapy. This chapter explores the combination of visible laser irradiation to plasmonic gold nanoparticles, which facilitates the formation of vapor nanobubbles at the interface of nanoparticle and cell medium, whose collapse results in the formation of permanent pores on the cell membrane, resulting in cell death. The chapter further explores the applicability of the system for spot laser irradiation and scanning laser irradiation at specific sites to kill cells. Further, we explored the effect of varying concentrations of gold nanostars on the cell killing efficiency and applicability of the system for three cell types of HeLa, HEK, and SAOS-2.

Chapter 5 explores the applicability of Prussian blue nanoparticle clusters (PBNCCs) for application into intracellular delivery and photothermal ablation for patterning cells. First, we explored the effect of varying process parameters such as PBNCCs concentration and laser fluence for intracellular delivery of Fluorescein Isothiocyanate (FITC) Dextran into HeLa cells. Moreover, we check the applicability of the same setup for site-specific ablation of HeLa cells, which assists in the formation of precise cell patterns. We optimized similar process parameters for cell patterning. We further formed cell micropatterns of target size at the optimized parameters and analyzed the accuracy and precision of pattern formation. This chapter highlights that a similar photoabsorber setup can be used for creating both transient and permanent pores in cell membrane.

In summary, this thesis presents four different approaches for creating site-specific cell perforation in cell monolayers. The experiments conducted in this thesis highlight that careful selection of photoabsorber material and laser parameters facilitates obtaining a deterministic outcome of cell perforation in the form of transient pores to help in intracellular delivery and permanent pores for killing cells to apply for the application of photothermal therapy and cell patterning.

Table of Contents

List of Figures

List of Tables

List of Abbreviations

CAR: Chimeric Antigen Receptor

iPS: Induced Pluripotent Stem Cells

DNA: Deoxyribonucleic Acid

RNA: Ribonucleic Acid

UVB: Ultraviolet B

NB-UVB: Narrowband Ultraviolet B

PUVA: Porslan Ultraviolet A

PDL: Pulsed Dye Laser

LITT: Laser-Induced Interstitial Thermotherapy

ROS: Reactive Oxygen Species

PDT: Photodynamic Therapy

PTT: Photothermal Therapy

NIR: Near-Infrared

PDMS: Polydimethylsiloxane

mRNA: Messenger Ribonucleic Acid

CRISPR: Clustered Regularly Interspaced Short Palindromic Repeats

PR254: Pigment Red 254

FITC: Fluorescein Isothiocyanate

FESEM: Field Emission Scanning Electron Microscope

PI: Propidium Iodide

IPA: Isopropyl Alcohol

HMDS: Hexamethyldisiloxane

CMOS : Complementary Metal-Oxide-Semiconductor

FBS: Fetal Bovine Serum

DMEM: Dulbecco's Modified Eagle Medium

EDTA: Ethylenediaminetetraacetic Acid

PBS: Phosphate-Buffered Saline

GNS: Gold Nanostars

CW NIR: Continuous Wave Near-Infrared

HEPES: 4-(2-hydroxyethyl)-1-piperazineethanesulfonic acid

PVP: Polyvinylpyrrolidone

DI water: Deionized Water

XRD: X-ray Diffractometer

FCC: Face-Centered Cubic

PBNPs: Prussian Blue Nanoparticles

PBNCCs: Prussian Blue Nanocube Clusters

Chapter 1: Introduction

1.1 Cell Therapy and Regenerative Medicine: Current Challenges

In cell therapy, approximately 10^6 T cells (immune cells that originate in the thymus and help detect and destroy infected or abnormal cells through targeted immune responses) from the patient's immune system are collected and genetically modified to express a Chimeric Antigen Receptor (CAR), transforming them into CAR-T cells capable of recognizing and attacking cancer cells (Figure 1.1). These engineered cells are then expanded in large numbers and reintroduced into the patient's body to target tumor-specific antigens. However, for such therapy to be safe and effective, it is critical to ensure that only properly modified and functional CAR-T cells are reintroduced, while eliminating any cells with unintended functions that could cause off-target effects or immune complications. Therefore, high safety standards demand that the presence of non-functional or misdirected cells be minimized—ideally reduced to zero. Achieving this level of precision requires not only robust selection and purification methods but also highly efficient and reliable gene delivery technologies. The success of CAR-T cell therapy thus heavily depends on the development and optimization of safe, efficient, and scalable techniques for introducing CAR genes into patient-derived T cells [1–7].

Next-generation medical treatment, such as regenerative medical treatment, is being realized (Figure 1.1). However, the popularization is difficult because it requires several months and tens of millions of yen for the treatment based on the present functional modification and selection technology of the cell. In regenerative medicine, the patient's skin cells are extracted, converted into Induced Pluripotent Stem Cells (iPS) cells by gene transfer, and processed and cultured into a sheet composed of $10^4 \sim 10^5$ retinal cells for transplantation. Hence, intracellular delivery of foreign molecules into cells to produce either sheet of iPSc cells is of paramount importance [8–12].

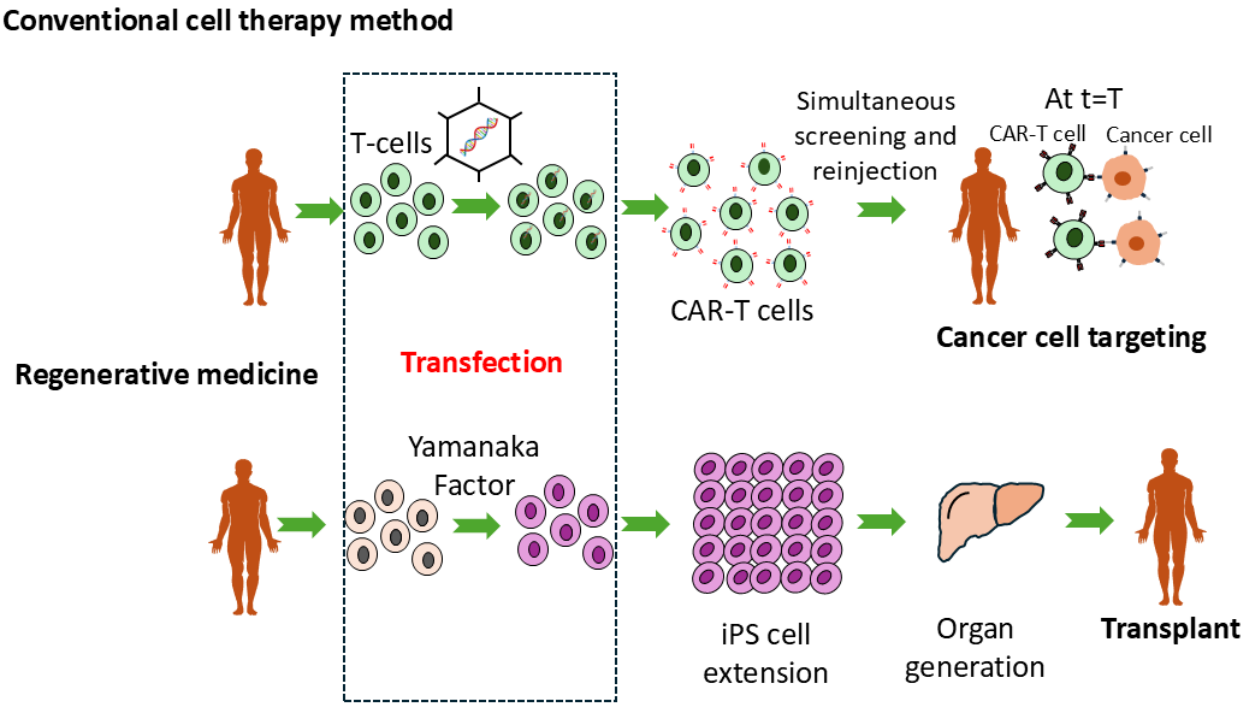

Figure 1.1 Process flow in cell therapy and regenerative medicine.

Delivery of foreign molecules, however, into the cell cytosol presents various complex challenges due to biological, translational, and clinical constraints surrounding the intracellular delivery process. Usually arising due to the variable nature of foreign molecules required to be delivered, the heterogeneity among the target cell types, and variability in the delivery outcomes, etc.

The variability and biological intricacy of cargo materials such as genetic materials (DNA and RNA molecules), protein molecules, and gene-editing tools (Cas9 enzymes, etc.) are often very large in size and require gentle delivery into cells due to their fragile nature. It is of utmost importance in methods like cell therapy, where the change in cell function directly depends on the precise activity of certain biomolecules within the cell.

Cell heterogeneity adds to the challenge of intracellular delivery because target cells in various modern biomedical technologies, such as cell therapy and regenerative medicines, include variety of cell types, such as immune cells, stem cells of cells derived from specific patients, which possess

different physiological properties. Each cell has different endocytic activity, whereas differences in membrane composition render variable responses to applied external stress. Furthermore, among the cells themselves, heterogeneity exists, requiring targeted uniform processing of cells considering the variation in properties of each cell. Hence, these reasons pose a challenge to the generalization of the developed intracellular delivery methods.

Another important aspect is the viability of cells post-intracellular delivery treatment. For example, in the autologous therapy methods, since the supply of cells is limited, it is of utmost importance to preserve the cell viability with stable cell function and genetic expression. Any disturbance in the above-mentioned properties hinders the efficacy of the therapeutic effort and hence poses the challenges of efficient intracellular delivery, introducing a foreign molecule into the cells without change in any physiological behaviors of cells and alterations of cell behavior, such as unwanted differentiation.

Moreover, the intracellular environment also poses difficulty in efficient delivery, as once the cargo material is inside the cells, the molecules need to navigate in the complicated intracellular compartments to reach their target site of action, such as the nucleus or a specific cell organelle. However, the crowded intracellular environment is tightly regulated and responds to any external disturbance caused by to entry of cargo material into the intracellular environment. The response in the cell microenvironment can cause the rerouting of the target molecule and might result in off-target outcomes, which can result in a drastic reduction in the efficacy of the applied theranostic strategy even if the delivery of the intracellular molecule was successfully achieved.

Furthermore, the clinical translation further complicates the intracellular delivery process because the therapies must be produced in a standardized, scalable, and highly reproducible manner with strict regulatory requirements. Hence, variability in delivery outcomes arises due to patient-specific factors, inconsistencies in the batches, and environmental conditions. Reproducibility across

a large-scale population, patient-specific, consistent outcomes are paramount for gaining regulatory approval and ensuring the safety of therapeutic outcomes.

Finally, in the physiological context in which the cells are planned to be replanted upon intracellular delivery also plays a great role in determining the success of the development of intracellular delivery methods. The nature of the environment where cells are introduced is often complex, such as aging tissues, inflammatory sites, and biomedically engineered scaffolds, which can play a role in influencing cell behavior, the uptake dynamics, and overall efficacy of the treatment. Hence, a lot of effort is required to be put into ensuring that delivered cells maintain their consistent desired function, get used to the new physiological environment, and contribute effectively to the given task.

In sum, intracellular delivery in the context of cell therapy and regenerative medicine is challenged by a combination of factors encompassing biological fragility, cell population heterogeneity, barriers inside the cell, and demands of clinical scalability. These challenges must be holistically addressed to realize the full potential of the modern intracellular delivery strategies.

1.2 Evolution of Phototherapy Techniques: From Conventional to Advanced Approaches

The concept of phototherapy dates to ancient times when sunlight was used for restorative effects on various skin conditions and ailments, known as Heliotherapy. However, around the 20th century, phototherapy emerged as one of the clinical treatment modalities with the discovery of the ultraviolet light's response on biological tissues [13]. Earlier, rickets were treated with UV lamps, and neonatal jaundice was treated with blue light [14], where application of light enabled the breakdown of bilirubin in the infants. This success in the application of light energy for biomedical applications laid the foundation for the use of light as more refined, evidence-based techniques for treatment applications.

Conventional phototherapy methods included the utilization of broad-spectrum or narrow-band UV radiation to manage disorders such as psoriasis, vitiligo, and atopic dermatosis. Treatments like broadband UVB and Narrowband UVB (NB-UVB) were not invasive, relatively cost-effective, and had easy accessibility [15]. PUVA therapy, combined with psoralen (a photosensitizing drug) with UVA light, became one of the prominent methods for treating skin conditions [16]. Even though these techniques were popular, they brought with them the risk of skin cancer and immune suppression. Additionally, these methods lack the precision and accuracy required to treat areas specifically, hence affecting healthy tissues alongside the target site of treatment.

The next benchmark in the advancement of phototherapy was the advent of laser introduction in the medical field. With a laser being a monochromatic coherence source of light with the capability of focusing, it became easier for medical professionals to focus the laser on the target tissue locations, hence increasing the precision of the overall process. Pulsed dye lasers (PDLs), Nd: YAG lasers, and CO_2 lasers became essential tools in dermatology, ophthalmology, and surgery [17]. Their ability to coagulate blood vessels, resurface skin, and ablate tissue with minimal thermal damage improved both therapeutic outcomes and patient recovery times. In oncology, laser-induced interstitial thermotherapy (LITT) emerged as a method to thermally ablate tumours under image guidance, offering a minimally invasive alternative to traditional surgery [18].

Moving forward, phototherapy was advanced by integrating the photosensitizers, which, once activated by a specific wavelength of light, these photosensitizers produce reactive oxygen species (ROS) that induce cell death in the targeted tissues, such as tumours or various infections. This method was called Photodynamic therapy (PDT) [19–22]. Now it has become a well-known treatment for certain kinds of cancers, such as esophageal, lung, and skin cancers. It offers selective toxicity and repeatable results without the development of any resistance. It is a very versatile method often used for treating acne, bacterial infections, and muscular degeneration. Even though it is a versatile method,

challenges remain in optimizing the penetration of laser light in deep tissues and minimizing the photosensitivity side effects.

The advancement of nanotechnology opened new avenues for the advancement of a new class of phototherapy called photothermal therapy (PTT) [23–30]. In Photothermal Therapy, a photoabsorber molecule is used, such as gold nanoparticles (nanospheres, nanoshells, nanorods, nanostars), Prussian blue nanoparticles (nanocubes), or carbon nanoparticles (nanotubes). When irradiated with a laser beam, these particles absorb the energy of the laser and convert it into thermal energy in the form of heat, thus destroying the target tissue by ablation without harming the off-target tissues. PTT holds promise in treating tumors that are hard to treat with surgery. Furthermore, the nanoparticles offer properties such as tunability of nanoparticle wavelength, permitting the control of laser absorption, biodegradability, and targeting efficiency, making it a highly customizable method for treating cancers with photothermal methods.

1.3 Cell Patterning Methods and Their Importance in Modern Biomedical Engineering Applications

Cell patterning refers to the precise control of cells over cell arrangements on the cell culture substrates and is a foundational requirement in modern biomedical and bioengineering applications. The ability to organize the cells in a predefined architecture enables a broad range of applications, such as the fabrication of tissue-engineered constructs [31], development of organ-on-a-chip models [32] and investigation of cell-cell, cell-matrix interactions [33] (Figure 1.2).

In tissue engineering applications, cell patterning can be used to mimic structural and functional tissue units by guiding the organization of various cell types that recreate the natural tissue structure. For example, spatially patterned cardiac cells, neural, and hepatic cells have been utilized to construct the engineered tissue patches capable of integrating with the host tissue and restoring the function of the host tissue. In regenerative medicine, organizing the stem cells in defined zones in

scaffolds can promote direct differentiation and contribute to the enhancement of the tissue regeneration process.

Cell patterning plays a pivotal role in the advancement of organ-on-a-chip platforms, where an engineered system integrates patterned cells with microfluidic structures to mimic organ-level function. These kinds of models allow for real-time monitoring of the biological response of cells and are increasingly getting popular in the field of drug testing and disease modelling.

In addition to this, a patterned arrangement of cells is necessary for studying cell interaction, communication, and cell signalling. The spatial context of cells affects the response of cells to external stimulations, neighbouring cell interaction, and organization into physical networks. By controlling the relative position of the cell types, we were able to study the contribution of the spatial context of cells to various processes such as differentiation, proliferation, and immune response

Furthermore, in drug discovery and screening, patterning of cells allows for high-content, high-throughput experimental layouts that are highly reproducible and quantifiable. It also allows for uniform exposure of cells to test compounds and support automation in various assay platforms, increasing efficiency and consistency across experiments.

In summary, cell patterning is a pivotal technique that underpins many of the most modern biomedical engineering techniques. By enabling the spatial organization of cells, cell patterning enables physiologically relevant models and contributes to precise functional studies for further therapeutic developments. Its incorporation into the next generation of biomedical technologies continues to expand the frontier of modern biomedical technologies, such as tissue engineering and precision diagnostics.

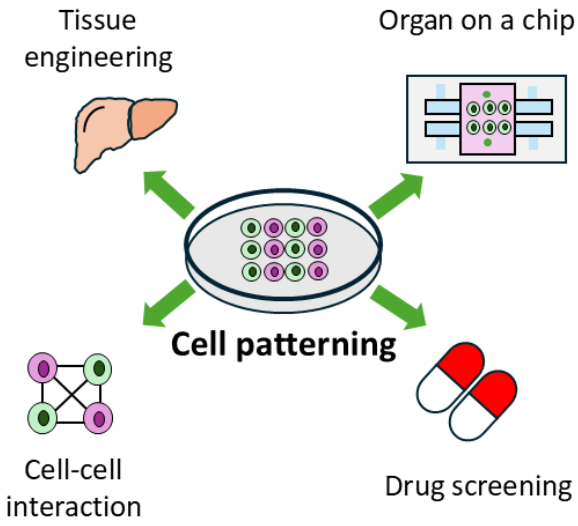

Figure 1.2 Applications of cell patterning.

1.4 Photoabsorber Mediated Cell Perforation by Laser Irradiation

Intracellular delivery, photothermal therapy, and cell patterning methods are unified by the fundamental requirement of highly precise spatial manipulation of cells to achieve desired therapeutic or engineering outcomes by creating highly controlled pores on the cell membranes of either transient or permanent nature. This precise perforation capability is essential for regulating the transport of biomolecules, controlling cellular responses, and enabling spatially selective therapeutic interventions. In intracellular delivery, transient nanoscale pores allow functional molecules such as nucleic acids, proteins, or drugs to enter cells without compromising their viability or physiological behavior, which is critical for applications like CAR-T engineering and regenerative medicine. In photothermal therapy, localized and often permanent disruption of cell membranes facilitates selective ablation of diseased or malignant cells while sparing surrounding healthy tissue, thereby improving treatment specificity and safety. In cell patterning, controlled perforation enables spatially defined molecular uptake and modulation of cell adhesion or signalling pathways, allowing cells to be organized into pre-determined architectures for tissue engineering, organ-on-a-chip systems, and high-throughput drug screening platforms. The shared challenge across these domains lies in achieving uniform, site-specific, and

minimally invasive pore formation despite biological heterogeneity, varying cell membrane properties, and the need for scalability.

In recent years, the demand for high-precision, minimally invasive techniques for the above-mentioned research fields has driven the exploration of photonic techniques for cellular manipulation. Photoabsorber-assisted laser irradiation has emerged as a promising platform for achieving site-specific cell membrane perforation outcomes in the form of a permanent or transient change in the integrity of the cell membrane. The unique spatial precision offered by the combination of photoabsorbers and laser irradiation promises the possibility of utilization in applications ranging from intracellular delivery to targeted cell ablation and dynamic cell patterning.

The principle underpinning this approach involves the use of photoabsorbers—materials capable of absorbing incident laser energy and converting it into localized thermal energy. These photoabsorbers, which may be in the form of nanoparticles (NPs) suspended in the culture medium or structured micropatterns fabricated on a substrate, are introduced in proximity to biological cells. When irradiated with a laser of appropriate wavelength and fluence, the absorbed energy results in localized phenomena such as photothermal heating or photoacoustic shockwave generation. These effects transiently or permanently disrupt the integrity of the cell membrane, thereby enabling controlled molecular delivery or inducing cell death. This technique offers a significant advantage over conventional biochemical or mechanical delivery systems, which often suffer from issues such as poor targeting specificity, low transfection efficiency, and systemic toxicity. In intracellular delivery, for instance, traditional methods rely heavily on chemical carriers such as liposomes or polymers, which frequently lead to off-target effects and cytotoxicity. In contrast, laser-based optoporation using photoabsorbers enables spatially precise membrane permeation, allowing for the selective introduction of functional molecules—such as nucleic acids, proteins, or drugs—into targeted cells without harming surrounding populations. Similarly, in cancer therapy, conventional treatment modalities such as chemotherapy and radiation are limited by poor selectivity and the inability to penetrate hypoxic tumor

cores. Photoabsorber-mediated photothermal therapy (PTT) circumvents these challenges by inducing localized heating within malignant cells, leading to precise ablation with minimal damage to adjacent healthy tissue. Beyond delivery and therapy, photoabsorber-assisted laser techniques also facilitate dynamic cell patterning, a critical tool in tissue engineering and regenerative medicine. Unlike traditional patterning methods, which require complex lithographic fabrication and lack real-time adaptability, laser-based patterning enables contactless, in situ manipulation of cell arrangements, thus offering unprecedented control over cellular microenvironments. Cells, when combined with photoabsorbers in the form of nanoparticles or structured micropatterns, are irradiated with a pulsed laser. This results in membrane permeation, which can be tuned to be either transient (allowing molecular delivery) or permanent (inducing cell death), depending on the application, as represented in Figure 1.3.

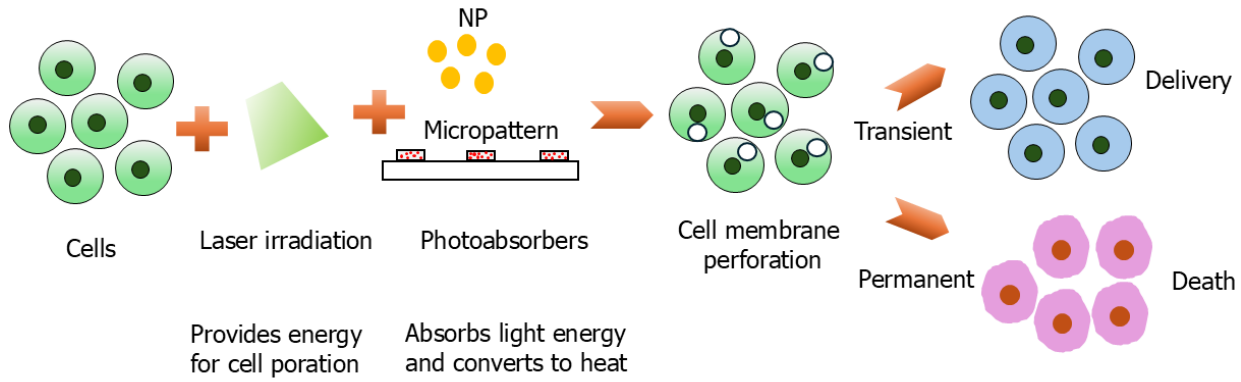

Figure 1.3 Photoabsorber-assisted laser irradiation for cell perforation.

Analysis of conventional biomedical methods and photoabsorber-assisted strategies highlights the latter's superiority in terms of spatial precision, therapeutic specificity, and real-time adaptability. Taken together, these attributes make photoabsorber-assisted laser irradiation a versatile and powerful tool in modern biomedical science. The current thesis is motivated by the need to explore and optimize this technique for a wide range of cellular applications, from therapeutic delivery to localized cancer ablation and live cell patterning. By systematically evaluating the physical interactions between laser

light, photoabsorbers, and cells, this study aims to establish a robust framework for the development of next-generation photonic bio-intervention platforms. In the next section 1.5, we will first discuss the drawbacks of conventional methods of the above-mentioned biomedical fields, and in section 1.6, we will discuss how photoabsorber-assisted cell perforation methods can collectively overcome the drawbacks in the fields.

1.5 Limitations of Contemporary Methods for Intracellular Delivery, Photothermal Therapy, and Cell Patterning

A wide array of intracellular delivery techniques exists, including carrier-based methods such as chemical transfection, viral vectors [34,35] and physical energy-based methods such as electroporation [36–39], sonoporation [40–42], microinjection [43] and mechanoporation [44]. Even though they are useful in certain applications, these methods suffer shortcomings in terms of throughput, cell viability, spatial precision, and adaptability for certain applications (Figure 1.4). These shortcomings have motivated the emergence of optoporation as a next-generation strategy that uniquely addresses many of the constraints associated with traditional approaches.

Even though viral methods do not create pores on the cell membrane, they are the most popularly used state of method for intracellular delivery of foreign molecules into the cells. They are found to be achieving high efficiency in achieving long-term gene expression. However, they are often reported to be inducing concerns related to immunogenesis, mutagenesis, and limitations in terms of cargo size. Moreover, the production of viral vectors is a highly costly and labour-intensive process that should be performed in strictly regulated environments. Furthermore, the integration of viral DNA into the host genome can result in unpredictable gene expression or oncogenesis.

Chemical transfection methods, on the other hand, include molecules such as liposomes and cationic polymers and mainly depend on cellular uptake pathways such as endocytosis. These methods often suffer from endosomal entrapment and are very inefficient for non-dividing cells, and suffer from degradation of cargo material. Their efficiency is highly variable across different cell types and can

trigger unwanted cytotoxicity or immunogenicity due to the chemical nature of the transfection agents. Moreover, these methods are often not suitable for the delivery of large molecules such as plasmids or protein complexes.

Electroporation is one of the most prominently used state-of-the-art methods for introducing foreign molecules into the cell cytosol. However, this method indiscriminately exposes all the cells to a similar stimulus, regardless of their size or membrane composition. Hence, leading to a significant loss in cell viability of the population of cells. Moreover, this method heavily lacks spatial selectivity; hence, it is usually unable to process a subpopulation of cells within a larger population of cells. The heavy loss of cell viability often renders this method inappropriate for specific types of cells, such as neurons, stem cells, or immune cells, which are delicate and often irreversibly rupture the cell membrane, causing cell death.

Microinjection is another method for creating pores in the cell membrane. The method achieves high precision and accuracy, but even with its high spatial accuracy, it fails to process cells in parallel and thus is unsuitable for high-throughput applications. The technique requires very sophisticated micromanipulation of cells and takes a very long time to process even a small number of cells. Automation of this process is highly challenging, and thus, it becomes impractical for clinical translation with automated workflows.

Sonoporation relies on ultrasound waves to create microbubble cavitation and suffers from very inconsistent formation of pores in the cell membrane. Furthermore, the mechanical force involved can damage the surrounding tissue or alter gene expression. Due to the highly random nature of produced cavitation bubbles, the results are often poorly reproducible.

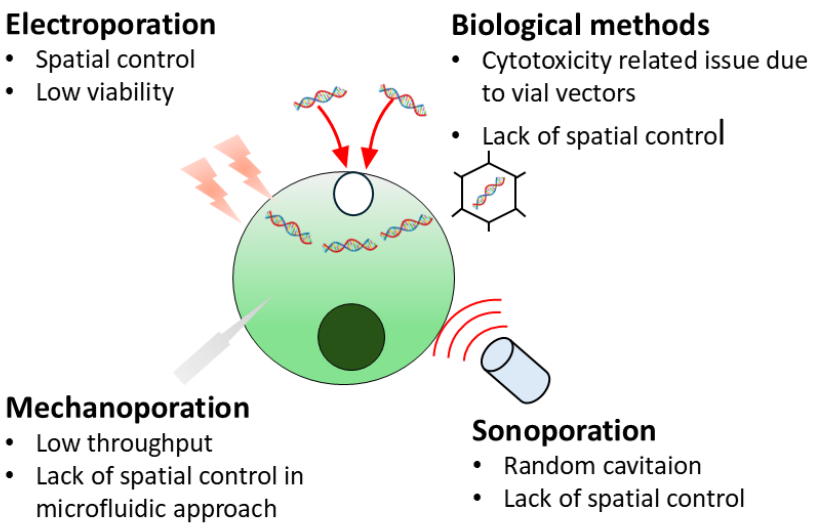

Figure 1.4 Perforation methods for intracellular delivery.

Furthermore, in the context of Photothermal therapy, A wide array of cancer treatment modalities exists, ranging from traditional methods like chemotherapy [45], radiotherapy [46], and surgery [47] to emerging techniques such as immunotherapy [48], gene therapy [49], and photodynamic therapy (PDT) [19, 20]. While each method offers specific benefits in certain clinical contexts, they suffer from notable limitations in terms of precision, off-target effects, systemic toxicity, and effectiveness against certain tumor types (Figure 1.5). These limitations have prompted the development of next-generation treatment strategies, with photothermal therapy (PTT) emerging as a particularly promising modality that leverages the unique advantages of nanotechnology and light-based interventions to overcome the drawbacks of conventional therapies.

Chemotherapy, although widely used, is plagued by non-specific toxicity. Chemotherapeutic agents indiscriminately affect both healthy and cancerous cells, often leading to severe side effects such as immunosuppression, nausea, and organ damage. Moreover, the development of multidrug resistance in tumors limits the long-term efficacy of these agents. Additionally, repeated dosing is required to maintain therapeutic concentrations, which can burden the patient and reduce quality of life.

Radiotherapy, another frontline treatment, also suffers from collateral damage to healthy tissues due to its limited spatial selectivity. The generation of ionizing radiation can cause DNA damage not only in cancer cells but also in surrounding normal cells, resulting in long-term complications such as fibrosis, secondary malignancies, or impaired organ function. Moreover, tumors located near critical structures such as the brain or spinal cord pose challenges in dose delivery without harming adjacent tissues.

Surgical resection remains a mainstay in solid tumor management; however, it is inherently invasive and may not be feasible for deep-seated or highly vascularized tumors. Complete tumor excision is often challenging due to irregular tumor margins, and residual microscopic disease can lead to recurrence. The postoperative recovery and associated complications further limit the application of surgery, especially in frail or elderly patients.

Photodynamic therapy (PDT), a minimally invasive approach that relies on light-activated photosensitizers to generate cytotoxic reactive oxygen species (ROS), offers better spatial control than chemotherapy or radiotherapy. However, PDT is oxygen-dependent, making it less effective in hypoxic tumor environments—a common characteristic of many aggressive tumors. Additionally, the limited tissue penetration of the activating light (typically in the visible range) restricts its utility to surface or near-surface tumors. The ROS generated can also cause inflammation and unintended damage to adjacent tissues.

In contrast, photothermal therapy (PTT) utilizes near-infrared (NIR) laser light in combination with photoabsorbing agents such as gold nanorods, Prussian blue nanoparticles, or carbon nanomaterials. These agents convert absorbed light into localized heat, inducing rapid hyperthermia that selectively ablates tumor tissues while minimizing collateral damage. One of the key strengths of PTT lies in its spatial precision—the laser can be finely focused to target only the tumor area, and heat generation occurs only where the nanoparticles are present, sparing healthy tissues.

Moreover, PTT is oxygen-independent, making it highly suitable for hypoxic tumor cores where PDT fails. The wavelength of NIR light (typically 700–900 nm) allows deeper tissue penetration, enabling treatment of tumors located several centimeters beneath the skin. Unlike chemotherapy, PTT does not rely on systemic toxicity and can be used repeatedly with minimal side effects. Furthermore, many photothermal agents are engineered for biodegradability, surface functionalization for tumor targeting, and tunable optical properties, offering flexibility across a range of cancer types and patient-specific needs.

While PTT still faces challenges in clinical translation, such as efficient delivery of nanoparticles to tumors, control of overheating distribution, and potential thermal damage to sensitive tissues, its customizability, non-invasive nature, and ability to synergize with other therapies (e.g., immunotherapy or drug delivery) position it as a highly promising alternative. Continued advances in nanotechnology, real-time imaging, and treatment planning are expected to further enhance the precision and safety of photothermal approaches, making them a key component of next-generation cancer therapy platforms.

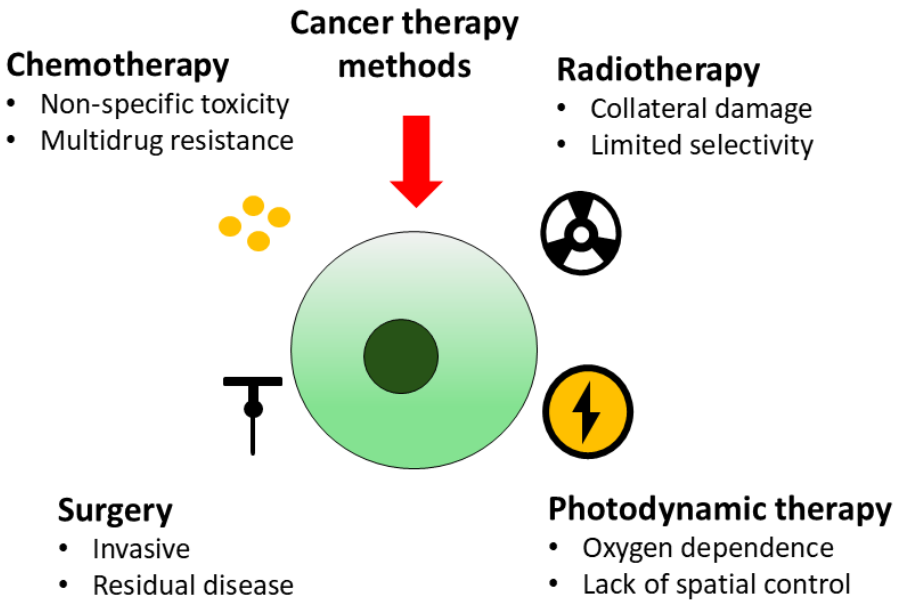

Figure 1.5 Strategies for cancer treatment.

Applicability of cell perforation methods extends beyond intracellular delivery and photothermal therapy. One of the interesting but challenging applications of the photoabsorber-assisted cell perforation method can be realized by patterning cells by selectively ablating and killing cells at specific sites. Cell patterning is an important field of biomedical and bioengineering and plays a crucial role in various fields such as tissue engineering, organ-on-a-chip development, and studying high-throughput cell heterogeneity. Despite its importance, current cell patterning methods face significant technical and pragmatic challenges in the realization of cell patterning methods with high scalability, precision, and application in clinical settings (Figure 1.6).

Microcontact printing is one of the prominent approaches of cell patterning and utilizes stamps made up of PDMS to transfer certain protein molecules and various cell adhesives to cell culture substrates in pre-designed micropatterns to enable site-specific growth of cells [50]. This method is simple and effective, but faces several challenges due to physical contact between the stamp and substrate, leading to deformation, variability in transferred microstructures eventually affecting the consistency of cell pattering. Moreover, the method is static, and the modification of patterns upon patterning is very challenging. Furthermore, this method suffers from a lack of ability to automate the process of cell patterning.

One more strategy to pattern cells is photolithography, a technique derived from the fabrication of semiconductor wafers, which utilizes selective exposure of photoresist on the cell culture substrate with UV light and prepares a substrate capable of culturing cells at specific sites [51, 52]. The spatial precision provided by this technique is excellent, but it requires cleanroom facilities, complicated fabrication protocols, and is limited to only a few types of substrates, such as glass or silicon wafers. Furthermore, the harsh chemicals applied during the fabrication process might remain on the cell culture substrate and cause cell toxicity.

Stencil and Physical confinement methods, such as microfluidic channels, use physical barriers to guide the spatial arrangement of cells. [53]. These methods also require a complicated fabrication process and cannot pattern cells in their natural cell culture petri dishes. Furthermore, the removal of the stencil can often result in disruption of the patterned cells. Inability to dynamically adjust cell position can also affect the utility of these methods in time-dependent studies such as cell migration and differentiation assays.

Dielectrophoresis-assisted cell patterning [54] and magnetic cell patterning [55] Offer label-free, contactless manipulation of cells based on their dielectric or magnetic properties. However, these methods require specialized equipment, precise control of external fields, and often introduce heterogeneity in cell responses due to variations in cellular properties. Additionally, concerns regarding potential damage from prolonged exposure to electric or magnetic fields raise questions about long-term biocompatibility.

Amongst these techniques for cell patterning, the major challenge is of scalability and low throughput of the process. Most of the methods are confined to small-scale experiments and are ill-suited for large area patterning and parallel processing of thousands of cells in parallel.

Finally, all the existing methods are mostly static; once the formation of a pattern is completed, it is highly challenging to alter the structure of the micropatterns, hence limiting the applicability of these micropatterns in the dynamic environments that mimic the real cell architecture rather closely. Furthermore, it limits the ability to conduct the experiments that require spatiotemporal control over the position of cells. Furthermore, the lack of automation and feedback integration precludes real-time pattern adjustment based on live-cell imaging or analysis.

These limitations highlight the need for innovative, dynamic, and scalable cell patterning technologies that can provide high spatial resolution, minimal invasiveness, real-time adaptability, and compatibility with live-cell environments. In this context, laser-assisted photothermal cell patterning,

particularly when combined with photoabsorbers like Prussian Blue nanoparticles, presents a compelling alternative that remains largely unexplored and warrants further investigation.

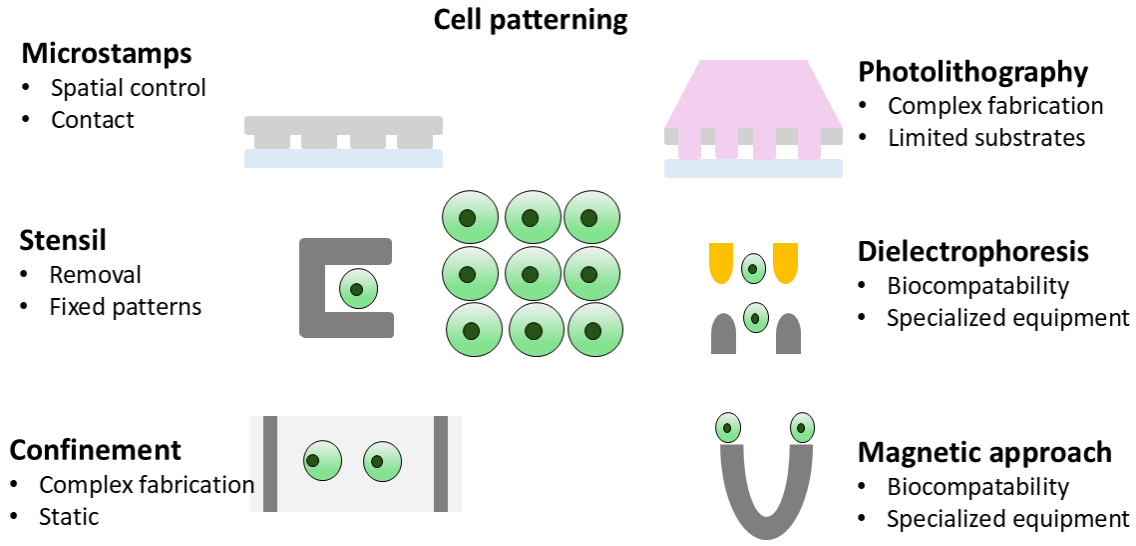

Figure 1.6 Cell patterning strategies and their drawbacks.

1.6 Objectives and Significance of Photoabsorber-Assisted Laser Technique for Intracellular Delivery, Photothermal Therapy, and Cell Patterning

Photoabsorber-assisted laser techniques, such as laser-induced shockwaves and photothermal therapy (PTT), have emerged as transformative tools in biomedical applications due to their unique combination of spatial precision, minimal invasiveness, and tunability. These approaches harness the rapid absorption of laser energy by photoabsorber materials to generate localized effects, such as shockwaves or heat, which can be directed with high specificity to biological targets.

1.6.1 Optoporation for Intracellular Delivery

One key application is optoporation, where laser-induced shockwaves are used to transiently permeabilize cell membranes for the intracellular delivery of therapeutic molecules. Unlike conventional methods such as electroporation or microinjection, optoporation offers site-specific

delivery, eliminating off-target effects and physical damage to surrounding tissues. The underlying mechanism involves the localized photothermal or photomechanical generation of vapor nanobubbles, which collapse and form shockwaves that create transient pores in the membrane, allowing passive diffusion of molecules into the cytosol. This method avoids complications related to carrier molecules, endosomal escape, or chemical toxicity and is particularly useful for delicate cargos like mRNA or CRISPR/Cas complexes. Moreover, optoporation is highly tunable—laser parameters such as wavelength, energy, and pulse duration can be adjusted to match specific photoabsorbers or tissue types. When combined with motorized stages and Galvano mirrors, this technique scales efficiently to high-throughput platforms that can process thousands of cells per minute. These advancements bridge the gap between single-cell precision and bulk-processing needs in areas like drug screening, cell reprogramming, and gene editing. Automation through machine vision and feedback-based laser control further allows integration with high-content analysis systems, enabling adaptive targeting and closed-loop experimentation for personalized therapy and large-scale studies.

1.6.2 Photothermal Therapy

In parallel, Photothermal Therapy (PTT) represents another powerful application of photoabsorber-assisted laser techniques. PTT utilizes targeted heat generation from photoabsorbers under laser irradiation to ablate cancerous tissues with high spatial precision. Compared to Photodynamic Therapy (PDT), which relies on oxygen to generate reactive oxygen species, PTT is effective even in hypoxic tumor environments, commonly seen in late-stage cancers. Furthermore, the ability to precisely control the thermal dose enables selective destruction of tumors while preserving adjacent healthy tissues. PTT also demonstrates advantages in terms of speed and versatility: the thermal effect leads to instantaneous and irreversible cell death through membrane disruption and protein denaturation, making it suitable for real-time or intraoperative applications. In contrast, PDT often requires multiple sessions to achieve similar outcomes. Additionally, photoabsorbers used in PTT can be co-functionalized with imaging agents and drugs, supporting theranostic approaches that

combine treatment and monitoring within a single platform. PDT's reliance on photosensitizers with narrow excitation windows and limited tunability makes it less adaptable in this regard.

1.6.3 Cell Patterning Application

In addition to therapeutic delivery and ablation, cell patterning via photothermal effects represents a promising yet underexplored application of photoabsorber-assisted laser techniques. Traditional cell patterning methods, such as soft lithography, microcontact printing, or stencil-based techniques, are limited by their complexity, poor scalability, and often static nature. In contrast, laser irradiation of cell monolayers incubated with photoabsorbers such as Prussian Blue or gold nanoparticles enable dynamic, non-contact, and high-throughput patterning through localized photothermal effects. Upon laser exposure, rapid heat generation leads to selective cell detachment, membrane perforation, or necrosis in predefined regions, effectively creating spatially controlled patterns of live and dead cells. This approach allows for precise manipulation of cell distributions on culture substrates without physical templates, offering significant flexibility in design and real-time adaptability. Moreover, by integrating laser scanning systems with automated stages and computer-controlled imaging feedback, it is possible to develop programmable, large-area cell patterning platforms suitable for tissue engineering, regenerative medicine, and in vitro model systems.

In conclusion, photoabsorber-assisted laser techniques such as optoporation and PTT address key limitations of traditional biomedical interventions—lack of spatial specificity, inability to scale, and limited tunability. By offering a highly adaptable, high-throughput, and precise platform for therapeutic delivery and tissue ablation, these technologies are well-suited for modern biomedical challenges, ranging from targeted drug delivery to personalized cancer therapy. Additionally, despite its clear potential, cell patterning via photothermal irradiation remains relatively unexplored, presenting a novel opportunity to leverage the scalability, precision, and speed of PTT-based systems

beyond therapeutic contexts. Table 1.1 concisely explains the significance of photoabsorber-assisted methods over conventional methods.

Table 1.1 Need and advantage of photoabsorber-assisted methods for biomedical applications.

Biomedical challenge	**Traditional approach limitations**	**Photoabsorber-assisted solution**	**Key advantages**
Intracellular delivery	Off-target effects, carrier toxicity, and low throughput	Site-specific optoporation	Spatial precision, carrier-free, scalable
Cancer therapy	Systemic toxicity, hypoxia limitations	Localized PTT	Precise thermal control
Cell patterning	Static patterns, complex fabrication	Dynamic laser patterning	Real-time adaptability, contactless

1.7 Thesis Organization

In the quest for the development of next-generation biological engineering therapeutic methods, to develop highly precise, minimally invasive, and spatially controlled cellular manipulation techniques, this thesis explores the photoabsorber-assisted laser irradiation for creating cell perforation at the center of the study as a versatile and tunable approach that allows disruption of the cell membrane through localized effects.

This thesis follows a strategically coherent framework characterized by materials diversification with application expansion, systematically exploring the versatility of photoabsorber-assisted laser techniques across a range of material platforms as depicted in Table 1.2. Rather than adhering to a purely sequential or purely parallel structure, the thesis adopts a hybrid exploration model. Each chapter investigates different photoabsorber materials—such as Pigment Red-254, Gold nanostars, and Prussian blue nanoparticles—applied to the core concept of site-specific laser-mediated cell perforation for creating either transient or permanent pores, while simultaneously expanding the scope of applications from intracellular delivery to photothermal therapy and spatial cell patterning. This progression reflects a parallel technological exploration aligned with a progressive application development strategy, moving from complex and costly methods toward simpler, more cost-effective solutions. Overall, the research demonstrates the broad adaptability and practical relevance of

photoabsorber-mediated laser irradiation for cell membrane pore creation, emphasizing its potential across multiple biomedical domains.

Table 1.2 Structure of thesis.

Cell perforation type explored	**Chapter number**	**Technical approach**	**Primary application**	**Key photoabsorber materials**	**Distinctive features & innovations**
Transient	**2**	Micropattern technology	Intracellular delivery	PR-254/SU-8 microdisks	Distance-dependent spatial analysis, size comparison, and cell-type-specific responses
Transient and permanent	**3**	Enhanced micropattern technology	Intracellular delivery and photothermal therapy	PR-254/SU-8 micropatterns	"Micropattern-on-top" configuration, high-throughput scalability, pitch optimization
Permanent	**4**	Gold nanostar technology	Photothermal therapy	Gold nanostars	Visible laser utilization, cancer cell selective killing, spot vs. scanning irradiation
Transient and permanent	**5**	Prussian Blue technology	Intracellular delivery and Cell patterning	Prussian Blue nanocube clusters	Cost-effective alternative, combined delivery + cell patterning capability

The first chapter of the thesis introduces the field of biomedical engineering, highlighting critical challenges in cell therapy, regenerative medicine, photothermal therapy, and cell patterning, where precise and efficient cellular manipulation is essential. It discusses the limitations of conventional intracellular delivery and therapeutic techniques, establishing the necessity for advanced approaches. The chapter then presents photoabsorber-assisted laser cell perforation as a unified, minimally invasive method capable of addressing these challenges by enabling controlled, site-specific transient or permanent membrane perforation. We first explored transient cell perforation with

micropattern-based substrate design functioning both as a photoabsorber and cell culture substrate to overcome the lack of spatial selectivity in conventional optoporation methods. The micropatterned substrate aids in monitoring the target area during the optoporation process (Figure 1.7). Upon laser irradiation, these defined patterns enabled parallel optoporation (Figure 1.7), effectively overcoming the limitations of conventional optoporation techniques that typically allow only single-cell treatment per laser pulse. Delivery of foreign molecules was successfully achieved with this technique, hence showing the Potential for application expansion.

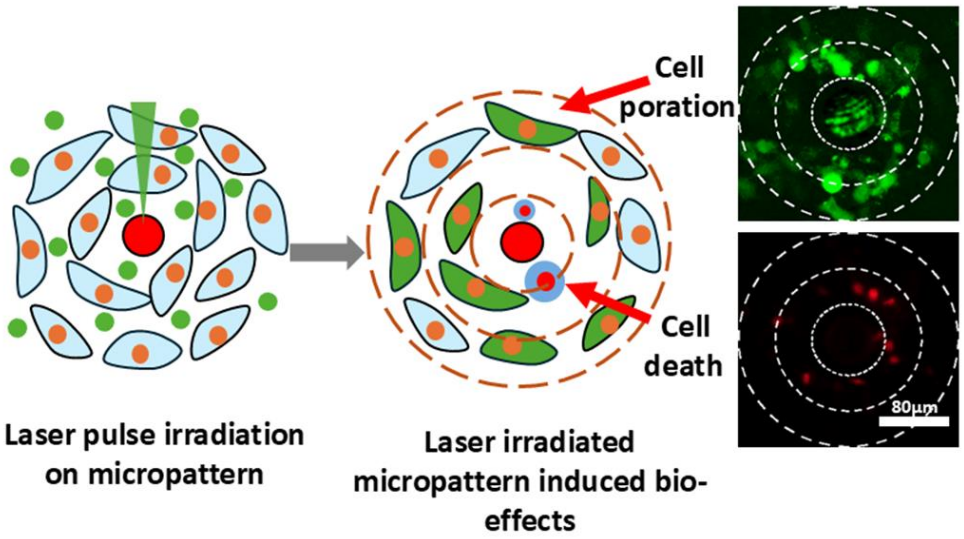

Figure 1.7 Micropattern-assisted site-specific optoporation for targeted intracellular delivery.

To expand the method described in Chapter 2, in Chapter 3, we introduce a novel micropattern-assisted, contactless cell perforation method as a technical enhancement. This setup eliminates the need for cells to be cultured directly on the micropatterned substrate. Instead, nanosecond laser scanning across the patterned chip enables site-specific, high-throughput cell processing (Figure 1.8). This advancement significantly increases the number of cells that can be processed in parallel, overcoming a key limitation of the traditional micropattern substrate-based approach. In this approach, we examine the response of HeLa cells to shockwaves generated by laser irradiation on a micropatterned surface. The cellular response is evaluated in terms of cell perforation, cell death, and

cell peeling—each of which contributes to the overall process of transient cell perforation and permanent cell perforation. Our "micropattern-on-top" strategy, combined with detailed parametric evaluation, provides a robust framework are optimizing biomedical applications in optoporation and photothermal therapy, balancing high delivery efficiency, spatial precision, and cellular viability to achieve desired therapeutic outcomes.

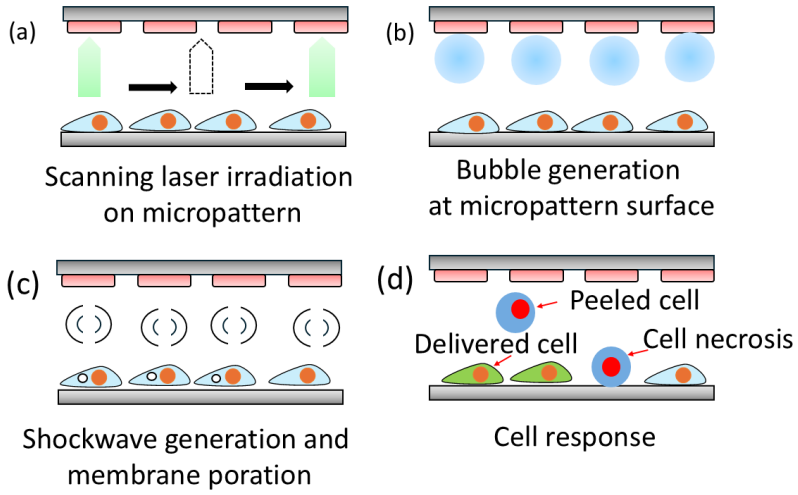

Figure 1.8 Optoporation with pr-254 micropatterns. (a) Laser Irradiation. (b) Micropattern laser interaction. (c) Shockwave generation. (d) Cell response.

Micropattern-assisted methods perform well for high-throughput applications requiring mass production of treated cells. However, creating micropatterns near each cell remains challenging. Therefore, in the next chapter, we focus on investigating a more localized approach, particularly aimed at achieving permanent cell perforation for photothermal therapy, where highly precise and targeted effects on cancer cells are essential. Hence, in Chapter 4, we investigate the potential of gold nanostars combined with visible laser irradiation. Most of the reports with gold nanostars used NIR lasers for photothermal therapy, and the usage of visible pulsed lasers in this application remains unexplored. It further explores the applicability of this system across different cell lines. The effectiveness of single-pulse spot irradiation and multiple-pulse laser scanning irradiation in inducing cell death was assessed

(Figure 1.9). Since the site of cell killing can be accurately chosen with a nanosecond pulse laser, this technique helps in minimizing damage to the cells around the target cells.

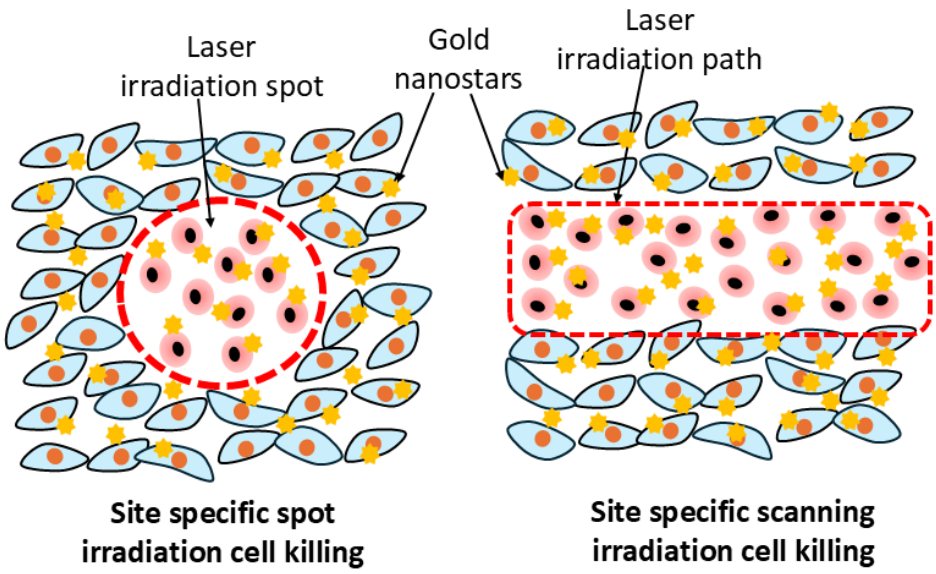

Figure 1.9 Site-specific cell killing with gold nanostars and laser irradiation.

Chapter 5 examines the feasibility of transient cell perforation and permanent cell perforation using Prussian blue nanoparticles. This study introduced Prussian Blue Nanocube Clusters (PBNCCs) as a cost-effective and biocompatible alternative to conventional gold nanoparticles and micropattern-based platforms for laser-assisted intracellular delivery and cell patterning (Figure 1.10). While existing approaches offer precision and efficiency, they face limitations due to high costs, fabrication complexity, and translational challenges. PBNCCs address these barriers with simple, scalable synthesis, adequate photothermal responsiveness, and low toxicity, enabling effective delivery of molecules like FITC-dextran into cells and site-specific cell ablation under nanosecond pulsed laser irradiation for cell patterning applications.

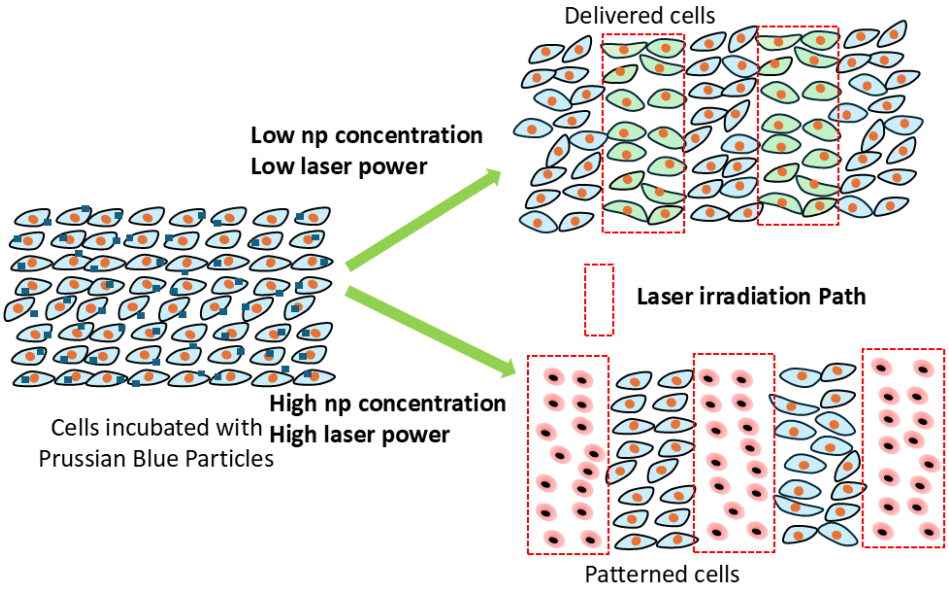

Figure 1.10 Intracellular delivery and cell patterning with Prussian blue nanoparticles.

Taken together, these four technologies represent a multi-dimensional expansion of the photoabsorber-assisted laser platform for creating pores on the cell membranes, each addressing key challenges in intracellular delivery, photothermal therapy, and cell patterning. Rather than functioning in isolation, these technologies can be integrated into a modular, adaptable system that leverages specific photoabsorber materials and geometries for tailored biomedical outcomes. Cells are interfaced with photoabsorbers—whether as nanoparticles, or spatial micropatterns—and then irradiated with nanosecond laser pulses. The interaction generates either transient or permanent membrane disruptions, facilitating controlled delivery or selective cell killing as depicted in Figure 1.11.

By systematically evaluating different photoabsorbers (micropatterned substrates, gold nanostars, and Prussian Blue nanocube clusters) under consistent laser conditions (532 nm wavelength, 5 ns pulse width), the outcome of the cell perforation can be mapped as represented in Figure 1.11. This unified model demonstrates how each platform occupies a distinct yet overlapping region within a continuous spectrum of bioeffects. For instance, micropattern-based methods generate smaller,

transient pores ideal for high-throughput molecular delivery and require larger laser fluence due to the non-metallic nature of the absorber, whereas gold nanostars produce larger, permanent disruptions suited for targeted cancer cell killing at lower laser fluences. Prussian Blue nanocube clusters offer a tunable intermediate behavior, enabling both delivery and controlled cell patterning. Indicating that by tuning the laser fluence desired outcome for cell membrane permeation can be achieved.

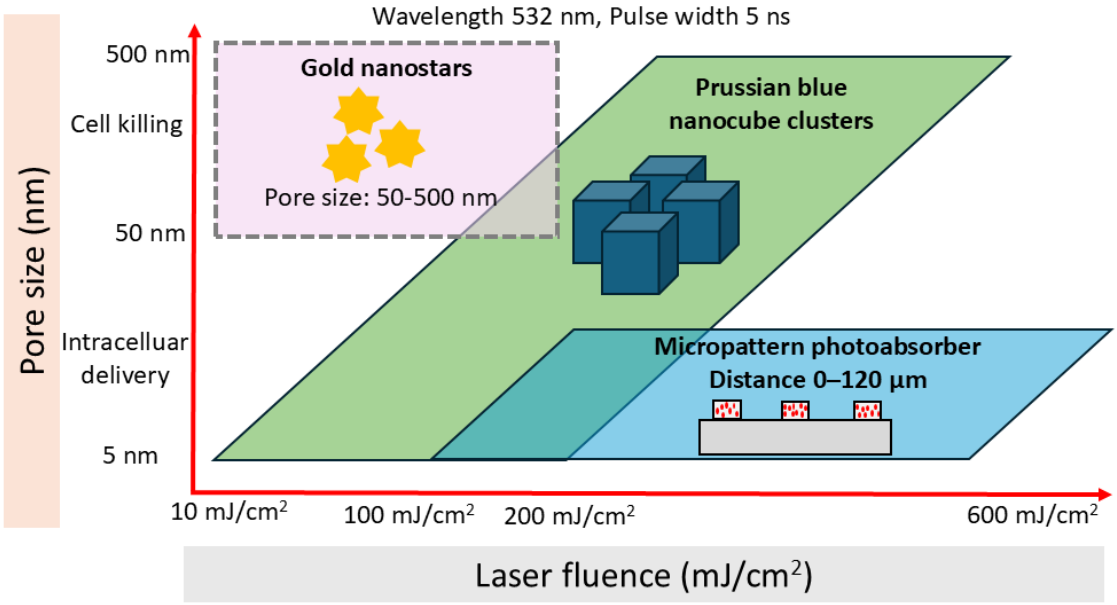

Figure 1.11 Unified framework for photoabsorber-mediated optoporation techniques.

This thesis is dedicated to the systematic development, integration, and optimization of emerging platforms for photoabsorber-assisted cell perforation technologies. By analyzing the interplay of laser parameters, photoabsorber properties, and biological responses, we aim to establish a generalized framework for next-generation photonic intervention technologies. These findings not only advance the fundamental understanding of light–material–cell interactions but also open new avenues for applications in targeted drug delivery, photothermal therapy, and cell patterning.

References

1. Bashor, C.J.; Hilton, I.B.; Bandukwala, H.; Smith, D.M.; Veiseh, O. Engineering the Next Generation of Cell-Based Therapeutics. Nat Rev Drug Discov 2022, 21, 655–675.

2. El-Kadiry, A.E.H.; Rafei, M.; Shammaa, R. Cell Therapy: Types, Regulation, and Clinical Benefits. Front Med (Lausanne) 2021, 8, PMID: 34881261.

3. Newick, K.; Moon, E.; Albelda, S.M. Chimeric Antigen Receptor T-Cell Therapy for Solid Tumors. Mol Ther Oncolytics 2016, 3, PMID: 27162934.

4. Bonifant, C.L.; Jackson, H.J.; Brentjens, R.J.; Curran, K.J. Toxicity and Management in CAR T-Cell Therapy. Mol Ther Oncolytics 2016, 3, 16011.

5. Maus, M. V; Grupp, S.A.; Porter, D.L.; June, C.H. Review Series Antibody Derivatives as New Therapeutics for Hematologic Malignancies Antibody-Modified T Cells: CARs Take the Front Seat for Hematologic Malignancies. 2014，123(17), 2625-35.

6. Sun, J.; Sadelain, M. The Quest for Spatio-Temporal Control of CAR T Cells. Cell Res 2015, 25, 1281–1282.

7. Fraietta, J.A.; Lacey, S.F.; Orlando, E.J.; Pruteanu-Malinici, I.; Gohil, M.; Lundh, S.; Boesteanu, A.C.; Wang, Y.; O'connor, R.S.; Hwang, W.T.; et al. Determinants of Response and Resistance to CD19 Chimeric Antigen Receptor (CAR) T Cell Therapy of Chronic Lymphocytic Leukemia. Nat Med 2018, 24, 563–571.

8. Kingham, E.; Oreffo, R.O.C. Embryonic and Induced Pluripotent Stem Cells: Understanding, Creating, and Exploiting the Nano-Niche for Regenerative Medicine. ACS Nano 2013, 7, 1867–1881.

9. Watari, K.; Yamasaki, S.; Tu, H.Y.; Shikamura, M.; Kamei, T.; Adachi, H.; Tochitani, T.; Kita, Y.; Nakamura, A.; Ueyama, K.; et al. Self-Organization, Quality Control, and Preclinical Studies of Human IPSC-Derived Retinal Sheets for Tissue-Transplantation Therapy. Commun Biol 2023, 6, 164.

10. Cerneckis, J.; Cai, H.; Shi, Y. Induced Pluripotent Stem Cells (IPSCs): Molecular Mechanisms of Induction and Applications. Signal Transduct Target Ther 2024, 9,112.

11. Matsumoto, E.; Koide, N.; Hanzawa, H.; Kiyama, M.; Ohta, M.; Kuwabara, J.; Takeda, S.; Takahashi, M. Fabricating Retinal Pigment Epithelial Cell Sheets Derived from Human Induced Pluripotent Stem Cells in an Automated Closed Culture System for Regenerative Medicine. PLoS One 2019, 14(3): e0212369.

12. Barabino, A.; Mellal, K.; Hamam, R.; Polosa, A.; Griffith, M.; Bouchard, J.-F.; Kalevar, A.; Hanna, R.; Bernier, G. Sub-Retinal Transplantation of Human IPSC-Derived Retinal Sheets: A Promising Approach for the Treatment of Macular Degeneration 2023 bioRxiv 2023.10.19.562811.

13. Holick, M.F. Biological Effects of Sunlight, Ultraviolet Radiation, Visible Light, Infrared Radiation and Vitamin D for Health. Anticancer Res. 2016, 36(3),1345-56.

14. Ennever, Blue Light, Green Light, White Light, More Light: Treatment of Neonatal Jaundice Clin Perinatol. 1990, 17, 467-481.

15. Berneburg, M.; Röcken, M.; Benedix, F. Phototherapy with Narrowband vs Broadband UVB. Acta Derm Venereol. 2005, 85, 98–108.

16. Farahnik, B.; Nakamura, M.; Singh, R.K.; Abrouk, M.; Zhu, T.H.; Lee, K.M.; Jose, M. V.; DaLovisio, R.; Koo, J.; Bhutani, T.; et al. The Patient's Guide to Psoriasis Treatment. Part 2: PUVA Phototherapy. Dermatol Ther (Heidelb) 2016, 6, 315–324.

17. Forbat, E.; Al-Niaimi, F. Nonvascular Uses of Pulsed Dye Laser in Clinical Dermatology. J Cosmet Dermatol. 2019, 18, 1186–1201.

18. Chen, C.; Lee, I.; Tatsui, C.; Elder, T.; Sloan, A.E. Laser Interstitial Thermotherapy (LITT) for the Treatment of Tumors of the Brain and Spine: A Brief Review. J Neurooncol. 2021, 151, 429–442.

19. García Calavia, P.; Bruce, G.; Pérez-García, L.; Russell, D.A. Photosensitiser-Gold Nanoparticle Conjugates for Photodynamic Therapy of Cancer. Photochem. Photobiol. Sci. 2018, 17, 1534–1552.

20. Li, X.; Lovell, J.F.; Yoon, J.; Chen, X. Clinical Development and Potential of Photothermal and Photodynamic Therapies for Cancer. Nat Rev Clin Oncol 2020, 17, 657–674.

21. Shang, L.; Zhou, X.; Zhang, J.; Shi, Y.; Zhong, L. Metal Nanoparticles for Photodynamic Therapy: A Potential Treatment for Breast Cancer. Molecules 2021, 26(21), 6532.

22. Yu, H.; Chen, J.; Chen, X.; Zhang, T.; Li, Y.; Chen, K.; Peng, Y.; Chen, L. Morpholinyl Silicon Phthalocyanine Nanoparticles with Lysosome Cell Death and Two-Photon Imaging Functions for in Vitro Photodynamic Therapy of Cancer Cells. Front Bioeng Biotechnol 2023, 11, PMID: 37214289.

23. Jung, H.S.; Verwilst, P.; Sharma, A.; Shin, J.; Sessler, J.L.; Kim, J.S. Organic Molecule-Based Photothermal Agents: An Expanding Photothermal Therapy Universe. Chem Soc Rev 2018, 47, 2280–2297.

24. Yang, K.; Zhao, S.; Li, B.; Wang, B.; Lan, M.; Song, X. Low Temperature Photothermal Therapy: Advances and Perspectives. Coord Chem Rev 2022, 454, 214330.

25. Huang, X.; Jain, P.K.; El-Sayed, I.H.; El-Sayed, M.A. Plasmonic Photothermal Therapy (PPTT) Using Gold Nanoparticles. Lasers Med Sci 2008, 23, 217–228.

26. Zhao, L.; Zhang, X.; Wang, X.; Guan, X.; Zhang, W.; Ma, J. Recent Advances in Selective Photothermal Therapy of Tumor. J Nanobiotechnology 2021, 19, 335.

27. Dacarro, G.; Taglietti, A.; Pallavicini, P. Prussian Blue Nanoparticles as a Versatile Photothermal Tool. Molecules 2018, 23(6), 1414.

28. Zharov, V.P.; Galitovsky, V.; Viegas, M. Photothermal Detection of Local Thermal Effects during Selective Nanophotothermolysis. Appl Phys Lett 2003, 83, 4897–4899.

29. Raghavan, V.; O'Flatharta, C.; Dwyer, R.; Breathnach, A.; Zafar, H.; Dockery, P.; Wheatley, A.; Keogh, I.; Leahy, M.; Olivo, M. Dual Plasmonic Gold Nanostars for Photoacoustic Imaging and Photothermal Therapy. Nanomedicine 2017, 12, 457–471.

30. Vo-Dinh, T.; Liu, Y.; Crawford, B.M.; Wang, H.-N.; Yuan, H.; Register, J.K.; Khoury, C.G. Shining Gold Nanostars: From Cancer Diagnostics to Photothermal Treatment and Immunotherapy; J Immunol Sci 2018; 2, 1-8.

31. Heller, E.; Fuchs, E. Tissue Patterning and Cellular Mechanics. J. Cell Bio 2015, 211, 219–231.

32. Ahmed, T. Organ-on-a-Chip Microengineering for Bio-Mimicking Disease Models and Revolutionizing Drug Discovery. Biosens Bioelectron X 2022, 11, 100194.

33. Filipponi, L.; Nicolau, D. Cell Patterning, 2006.

34. Naseri, N.; Valizadeh, H.; Zakeri-Milani, P. Solid Lipid Nanoparticles and Nanostructured Lipid Carriers: Structure Preparation and Application. Adv Pharm Bull 2015, 5, 305–31.

35. Sharma, N.; Purwar, N.; Chandra Gupta, p. Microspheres as drug carriers for controlled drug delivery: a review. Int J Pharm Sci Res 2015, 6, 4579.

36. Canatella, P.J.; Karr, J.F.; Petros, J.A.; Prausnitz, M.R. Quantitative Study of Electroporation-Mediated Molecular Uptake and Cell Viability; Biophys J 2001, 80(2), 755-64.

37. Gehl, J. Electroporation: Theory and Methods, Perspectives for Drug Delivery, Gene Therapy and Research. Acta Physiol Scand 2003, 177, 437–447.

38. Ding, L.; Fang, Z.; Moser, M.A.J.; Zhang, W.; Zhang, B. A Single-Cell Electroporation Model for Quantitatively Estimating the Pore Area Ratio by High-Frequency Irreversible Electroporation. App Sci (Switzerland) 2023, 13(3), 1808.

39. Santra, T.S.; Chang, H.Y.; Wang, P.C.; Tseng, F.G. Impact of Pulse Duration on Localized Single-Cell Nano-Electroporation. Analyst 2014, 139, 6249–6258.

40. Porret, E.; Hoang, S.; Denis, C.; Doris, E.; Hrubý, M.; Novell, A.; Gravel, E.; Truillet, C. Sonoporation-Assisted Micelle Delivery in Subcutaneous Glioma-Bearing Mice Evaluated by PET/Fluorescent Bi-Modal Imaging. Nanoscale 2023, 15, 12574.

41. Liang, H.D.; Tang, J.; Halliwell, M. Sonoporation, Drug Delivery, and Gene Therapy. Proc Inst Mech Eng H 2010, 224, 343–361.

42. Chen, Q.; Huang, J.; Ye, Y.; Hu, A.; Xu, B.; Hu, D.; Wang, L.; Xing, L.; Chen, S.; Gui, X.; et al. Delivery of Hydroxycamptothecin via Sonoporation: An Effective Therapy for Liver Fibrosis. J Cont Rel 2023, 358, 319–332.

43. Zhang, Y.; Yu, L.C. Microinjection as a Tool of Mechanical Delivery. Curr Opin Biotechnol 2008, 19, 506–510.

44. Chakrabarty, P.; Gupta, P.; Illath, K.; Kar, S.; Nagai, M.; Tseng, F.G.; Santra, T.S. Microfluidic Mechanoporation for Cellular Delivery and Analysis. Mater Today Bio 2022, 13, 100193.

45. Nygren, P. What Is Cancer Chemotherapy? Acta Oncol (Madr) 2001, 40, 166–174.

46. Soussain, C.; Ricard, D.; Fike, J.R.; Mazeron, J.J.; Psimaras, D.; Delattre, J.Y. CNS Complications of Radiotherapy and Chemotherapy. The Lancet 2009, 374, 1639–1651.

47. Tohme, S.; Simmons, R.L.; Tsung, A. Surgery for Cancer: A Trigger for Metastases. Cancer Res 2017, 77, 1548–1552.

48. Kantoff, P.W.; Higano, C.S.; Shore, N.D.; Berger, E.R.; Small, E.J.; Penson, D.F.; Redfern, C.H.; Ferrari, A.C.; Dreicer, R.; Sims, R.B.; et al. Sipuleucel-T Immunotherapy for Castration-Resistant Prostate Cancer. N Engl J Med 2010, 363, 411–422.

49. Cross, D.; Burmester, J.K. Gene Therapy for Cancer Treatment: Past, Present and Future; Clin Med Res 2006, Vol. 4(3), 218-27.

50. Rozkiewicz, D.I.; Kraan, Y.; Werten, M.W.T.; De Wolf, F.A.; Subramaniam, V.; Ravoo, B.J.; Reinhoudt, D.N. Covalent Microcontact Printing of Proteins for Cell Patterning. Chemistry 2006, 12, 6290–6297.

51. Karp, J.M.; Yeo, Y.; Geng, W.; Cannizarro, C.; Yan, K.; Kohane, D.S.; Vunjak-Novakovic, G.; Langer, R.S.; Radisic, M. A Photolithographic Method to Create Cellular Micropatterns. Biomaterials 2006, 27, 4755–4764.

52. Mishra, A.; Okamoto, S.; Shibata, T.; Santra, T.S.; Nagai, M. Bioresist-Based Single-Cell Array Chip for Standardized Optoporation, MicroTAS 2023, abstract no. 0476.

53. Frimat, J.P.; Menne, H.; Michels, A.; Kittel, S.; Kettler, R.; Borgmann, S.; Franzke, J.; West, J. Plasma Stencilling Methods for Cell Patterning. Anal Bioanal Chem 2009, 395, 601–609.

54. Lin, R.Z.; Ho, C.T.; Liu, C.H.; Chang, H.Y. Dielectrophoresis-Based Cell Patterning for Tissue Engineering. Biotechnol J 2006, 1, 949–957.

55. Ino, K.; Okochi, M.; Konishi, N.; Nakatochi, M.; Imai, R.; Shikida, M.; Ito, A.; Honda, H. Cell Culture Arrays Using Magnetic Force-Based Cell Patterning for Dynamic Single Cell Analysis. Lab Chip 2007, 8, 134–142.

Chapter 2: Micropattern-Assisted Cell Perforation: Distance-Dependent Spatial Analysis of Micropattern-Generated Shockwave for Cell-Type Specific Intracellular Delivery

2.1 Introduction

Cellular function deteriorates with age, injury, and disease, necessitating the delivery of therapeutic agents like drugs and nucleic acids into cells for treatment. However, the cell membrane's semipermeable nature poses a major challenge to this delivery process. Two primary approaches have emerged to overcome this barrier: carrier-mediated delivery using biochemical compounds [1–4], and membrane-permeating delivery employing physical methods [5–13]. While carrier-mediated approaches utilize vehicles such as liposomes [4], dendrimers [14], microspheres [3], and solid lipid nanoparticles [1]. These carriers can potentially induce cellular toxicity.

To reduce carrier-based toxicity, physical methods such as electroporation [5,15], microinjection [7], sonoporation [8], mechanoporation [16], hydroporation [17–19], and optoporation [11–13, 20–23] have emerged as alternatives to carrier-based delivery systems while achieving membrane-penetrating intracellular delivery. Electroporation requires careful optimization of parameters, including field duration, field strength, and pulse number, to maintain cell viability. Excessive field strength or prolonged duration can prevent proper resealing of membrane pores, leading to cell death through electrolyte imbalance [24, 25]. During sonoporation, ultrasonic acoustic pressure waves generate cavitation bubbles, whose random nature and transient characteristics can lead to cell death [26]. Additionally, microinjection techniques suffer from low throughput due to difficulties in parallelization [7]. Mechanoporation utilizes viscoelastic shear flow to create non-contact pores in cells. Hydroporation, in the context of intracellular delivery, incorporates high-pressure hydrodynamic shear to achieve pores. Both techniques are dependent on flow within microfluidic devices. While effective for high-throughput applications, these flow-based techniques

encounter difficulties in targeting specific sub-populations of cells. This inherently limits precise temporal and spatial control, making site-specific intracellular delivery problematic.

Laser-based optoporation enables high-throughput, non-invasive delivery of cargo materials into cells through light-induced transient pore formation in cell membranes [22, 27]. This technique comprises two main approaches: direct laser optoporation and photosensitized optoporation. While direct laser optoporation can create membrane pores by controlling laser parameters such as wavelength, intensity, and irradiation duration [28]. Its application is limited by low throughput and operational complexity due to the requirement for precise laser focusing on individual cell membranes.

Traditional photosensitized optoporation relies on photoabsorber-laser interactions to generate pores in cell membranes. When laser light irradiates the photoabsorber material, vapor nanobubbles form at cell culture medium-photoabsorber interface [29]. The growth and collapse of these bubbles create transient membrane pores. Conventional approaches typically employ gold or carbon nanoparticles attached to cell membranes through electrostatic attraction or antibody conjugation [30–35]. While this nanoparticle-based approach effectively generates vapor nanobubbles, it presents two major challenges: difficulty in targeting specific cell populations and potential toxicity from the nanoparticles themselves [36]. Although researchers have attempted to address these limitations using modified photothermal substrates with different TiO_2 nanostructures, such as nanoflowers and nanotubes [37, 38]. These substrate-based methods still fail to provide adequate spatial access for site-specific intracellular delivery.

Photolithographically patterned photo-absorbing micropatterns generate vapor nanobubbles upon pulsed laser irradiation through localized heating. Compared to traditional gold nanoparticle-based and modified substrate-based optoporation methods, micropattern-assisted optoporation provides precise targeting of specific sites with improved spatial control [20, 39]. The versatility of micropatterns allows customization to specific shapes, offering advantages for heterogeneous cell

populations [40, 41]. While micropatterned devices have demonstrated high throughput optoporation of adherent cell lines [20, 39], previous approaches using titanium micropatterns as photoabsorbers faced significant limitations [42]. The titanium-based method required complex vacuum deposition and time-consuming fabrication processes. Moreover, these devices needed to be inverted over cell monolayers during optoporation and subsequently removed after the procedure. This process compromised spatial information and hindered the tracking of specific target cells. Although delivery efficiency could be measured through flow cytometry or averaged image intensities, these methods inadequately captured the spatial dynamics of laser-micropattern interactions, leaving the distance-dependent effects of laser-induced cell perforation poorly characterized.

In this study, we explored the transient pore creation on the cell membrane by irradiating a pulsed laser on a micropattern-based cell culture substrate. We developed an analytical method using pigmented SU-8 microdisks to investigate how laser-micropattern interactions affect cell membrane perforation at varying distances (Figure 2.1). This approach enables systematic characterization of spatial effects using different microdisk sizes and reveals cell type-specific responses to shockwave exposure. The simplified fabrication process combining spin-coating and photolithography allows direct cell culture adjacent to the patterns, facilitating precise spatial analysis of single-pulse shockwave effects on cell membranes.

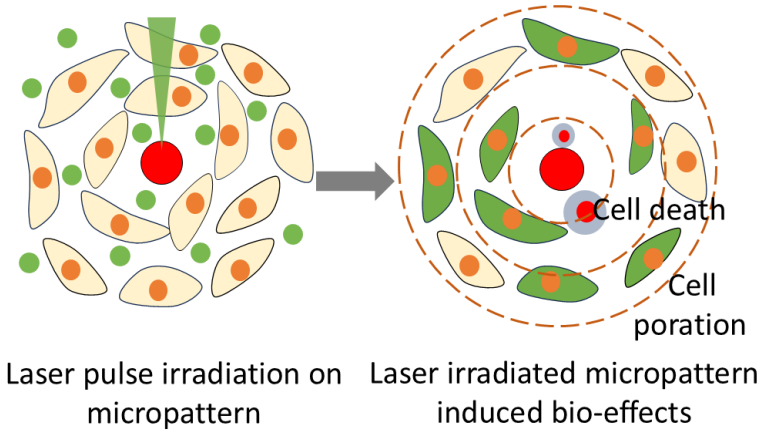

Figure 2.1 Representation of laser irradiated micropattern induced bio effects.

2.2 Experimental methods

2.2.1 Cell Perforation by Micropattern Irradiation

Upon laser irradiation of the microdisk pattern, the laser energy is rapidly absorbed by the microstructure. This absorption leads to swift heating of the microdisk, resulting in the generation of laser-induced shockwaves (Figure 2.2(a) and 2.2(b)). The strength of this laser shockwave significantly affects the structural integrity of the cell membrane (Figure 2.2(c)). The imaging data was quantitatively analyzed based on the above model, where the magnitude of the shockwave due to laser irradiation of the micropattern was expected to be higher closer to the micropattern, decreasing radially as the shockwave progressed in cell culture medium. The model implies that a higher shockwave will result in higher delivery efficiency. However, if the shockwave on the cells exceeds their tolerance, cell death occurs due to irreparable damage, and an even greater magnitude of shockwave peels off cells from the substrate. Hence, the process in the cell concerning shockwave magnitude occurs in the order of cell peeling from the substrate, cell necrosis on the substrate, cell delivery, and no effect, respectively. All these processes collectively contribute to the evaluation of delivery efficiency and cell viability.

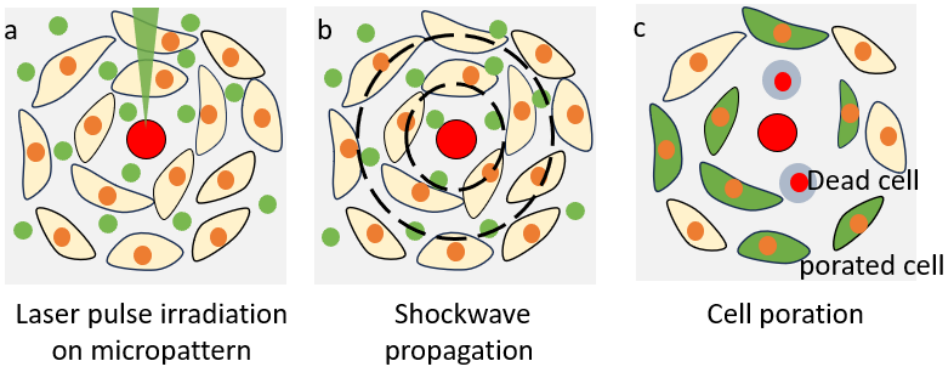

Figure 2.2 Schematic representation of the distance-dependent analysis method for micropattern-assisted optoporation. (a) Laser irradiation on the pigmented SU-8 microdisk. (b) Generation of shockwave upon bubble collapse in cell medium. (c) Intracellular delivery at varying radial distances from the irradiation point.

2.2.2 Calculation of Shockwave-Induced Pressure

The pressure exerted by the laser-induced shock wave is estimated by analyzing the displacement of microsphere particles (Figure 2.3). The motion of these microspheres can be divided into two phases: an acceleration phase and a deceleration phase.

In the acceleration phase, the particle is accelerated during the shock wave duration (Δt). Applying the principle of momentum conservation yields:

$$P \cdot S \cdot \Delta t = mv_0 \quad \ldots(2.1)$$

where P is shock wave pressure, S is the sphere's cross-sectional area, m is the mass of the sphere and v_0 is the initial velocity of the sphere.

In the deceleration phase, the sphere decelerates due to Stokes' drag in the water, described by:

$$m(dv/dt) = -6\pi\eta r v \quad \ldots(2.2)$$

where η is the dynamic viscosity of water. Solving this equation gives:

$$v(t) = v_0 e^{-\beta t}, \beta = 6\pi\eta r/m = 9\eta/(2r^2\rho) \quad \ldots(2.3)$$

Integrating the velocity equation yields the displacement:

$$x(t) = (v_0/\beta)(1 - e^{-\beta t}) \quad \ldots(2.4)$$

The final displacement can be calculated as:

$$x_{final} = v_0/\beta \quad \ldots(2.5)$$

The shock wave pressure can then be determined by:

$$P = (mv_0) / (S\Delta t) = (mv_0) / (\pi r^2 \Delta t) \quad \ldots(2.6)$$

The known values, $m = (4/3)\pi r^3\rho$, $v_0 = x_{final} \cdot \beta$ and $\beta = 9\eta/(2r^2\rho)$ are substituted into Eq. (2.6), we obtain

$$P = 6\rho \cdot x_{final} \cdot \eta / \Delta t \quad \ldots(2.7)$$

In the absence of a high-speed camera, the shockwave duration can be estimated to be approximately 50 nanoseconds for a 5-nanosecond pulsed laser, based on previous studies[43, 44]. The pressure at specific radial distances can be determined by measuring x_{final} from experimental data: P_{25} (pressure at 25 µm) for the 50 µm diameter microdisk and P_{10} (pressure at 10 µm) for the 20 µm diameter microdisk. Following the inverse-square law for pressure wave decay with distance [45, 46]. We can calculate pressures at radial distances of 40 µm (P_{40}), 80 µm (P_{80}), and 120 µm (P_{120}) using the known values of P_{10} and P_{25}. This approach enables mapping of the pressure distribution at various radial distances from the laser irradiation point, providing insights into the spatial characteristics of the laser-induced shockwave.

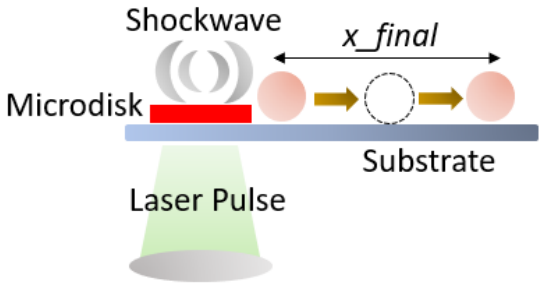

Figure 2.3 Schematic representation of particle propulsion on laser irradiation of micropattern.

2.2.3 Fabrication of Pigmented Microdisks

0.45 g of red pigment, PR-254 (P1676, Tokyo Kasei, Japan), was mixed with 15 mL of cyclopentanone in a centrifuge tube. This mixture was then mixed with 15 mL of SU-8 3005 (KAYAKU Advanced Materials, USA) to obtain 1.5 w/v% of PR-254. The SU-8-PR-254 mixture was stirred for 20 min on a vortexer (TRIO HM-2F, AZ-ONE, Japan) and then subjected to an ultrasonic cleaner (SonoCleaner 100D, KAIJO, Japan) for 5 min.

The prepared mixture was spin-coated on a 4-inch glass wafer, and circular patterns with 20 and 50 µm diameters were formed by photolithography to obtain photo-absorbing disks (Figure 2.4(a)-

(d)). A 4-inch glass wafer was washed with acetone and rinsed with isopropanol (IPA), then dried with nitrogen gas. The substrate was plasma-treated using a plasma ashing system (JPA-300, J-Science Labs, Japan) at 150 W for 60 s to improve hydrophilicity. Hexamethyldisiloxane (HMDS) was spin-coated on the plasma-treated glass substrate with the following spin-coating steps: a gradual increase in speed for 5 s, 1000 rpm for 10 s, a gradual decrease in speed for 5 s, 5000 rpm for 30 s, a gradual decrease in speed for 10 s, and then baked. The suspension of SU-8-PR-254 was spin-coated on the HMDS layer at a slope for 5 s, 500 rpm for 20 s; slope for 5 s; 3000 rpm for 60 s; slope for 10 s. The wafer was baked again and exposed with a light integral of 600 mJ/cm^2 using a mask aligner (PEM-800, Union Optical) through a mask. The mask contained one 10 × 10 array of 50-μm-diameter microdisks at 1 mm pitch and twelve 10 × 10 arrays of 20-μm-diameter microdisks at 300 μm pitch. The wafer was baked again after exposure and developed in 2-methoxy-1-methylethyl acetate. The wafer was diced into small chips before cell culture, and a silicone wall structure was attached with bioadhesive glue to avoid the slipping of cells from the device.

2.2.4 Analysis of Laser Pulse and Micropattern Interaction

Micropattern chips with pattern diameters of 50 μm and 20 μm were filled with 200 μL of deionized (DI) water. To characterize bubble formation, a series of laser fluences (36, 43, 49, 51, 58, 126, 164, 200, and 514 mJ/cm²) was tested on 50 μm diameter microdisks. For each fluence level, 20 different microdisks were irradiated, and bubble formation was recorded as a binary outcome (formed/not formed) using a CMOS camera (ZWO, ASL1600MC-Cool, Suzhou, China) with multi-dimensional acquisition in Micro-Manager 1.3 software. The probability of bubble formation was calculated as the percentage of successful formations out of 20 attempts.

For fluences that demonstrated 100% bubble formation probability (126–514 mJ/cm²), bubble size measurements were conducted. Images were acquired before and immediately after laser irradiation, and five independent measurements (n=5) were performed for each fluence level on both

20 μm and 50 μm microdisk patterns. The acquired images were analyzed using ImageJ software to calculate the diameters of the resulting bubbles, and the mean diameter and standard deviation were determined from the five measurements.

2.2.5 Measurement of Pressure on Microspheres

Polystyrene microparticles (Sigma Aldrich, 15 μm diameter, density = 1.05 g/cm³) were used to measure the shockwave pressure. The microparticles were placed immediately next to the edge of the microdisk pattern, and the laser was irradiated onto the micropattern. The particle displacement images were acquired after laser irradiation using the same method as described for bubble image acquisition. The displacement was measured, and pressure values were calculated at various radial distances from the center of the microdisk using the method described in section 2.2.4.

2.2.6 Cell Culture on Microdisks

A microdisk chip was sterilized with ethanol, acetone, and deionized (DI) water before cell culture. HeLa cells were cultured in minimum essential medium (MEM, Gibco, 11095072, Thermo Fisher Scientific, Waltham, MA, USA) supplemented with 10% fetal bovine serum (FBS, CCP-FBS-BR-500, Cosmo Bio, Tokyo, Japan) and 1% penicillin-streptomycin (streptomycin 10,000 U/mL, Thermo Fisher Scientific, Waltham, MA, USA). HEK293 and SAOS-2 cells were cultured in DMEM (FUJIFILM Wako Pure Chemical Co., Ltd., Tokyo, Japan) with 10% FBS and 1% penicillin–streptomycin (PS). The cells were grown in a polystyrene petri dish at 37 °C in a 5% CO_2 humidified atmosphere. The adherent cultured cells were detached from the petri dish using trypsin-EDTA. After replacement with fresh cell medium, the cells were seeded on the microchip at 37 °C with 5% CO_2 in the air. Cells were then cultured to 80-90% confluency on the disk substrate and washed with PBS before laser irradiation.

2.2.7 Optoporation and Observation Setup

We built a custom-made setup for laser-based optoporation (Figure 2.4(e)). A nanosecond pulse laser (532 nm, Cobolt, TorTM XS, Hubner Photonics, Solna, Sweden) was connected to a function generator. A dichroic mirror (Thorlabs, DMLP550R, Newton, NJ, USA) was placed to reflect a 532-nm light beam. A convex lens with a focal length of 50 mm focused the laser beam on the sample with a spot diameter of around 140 µm. The sample was observed using an objective lens and a CMOS camera (ZWO, ASL1600MC-Cool, Suzhou, China).

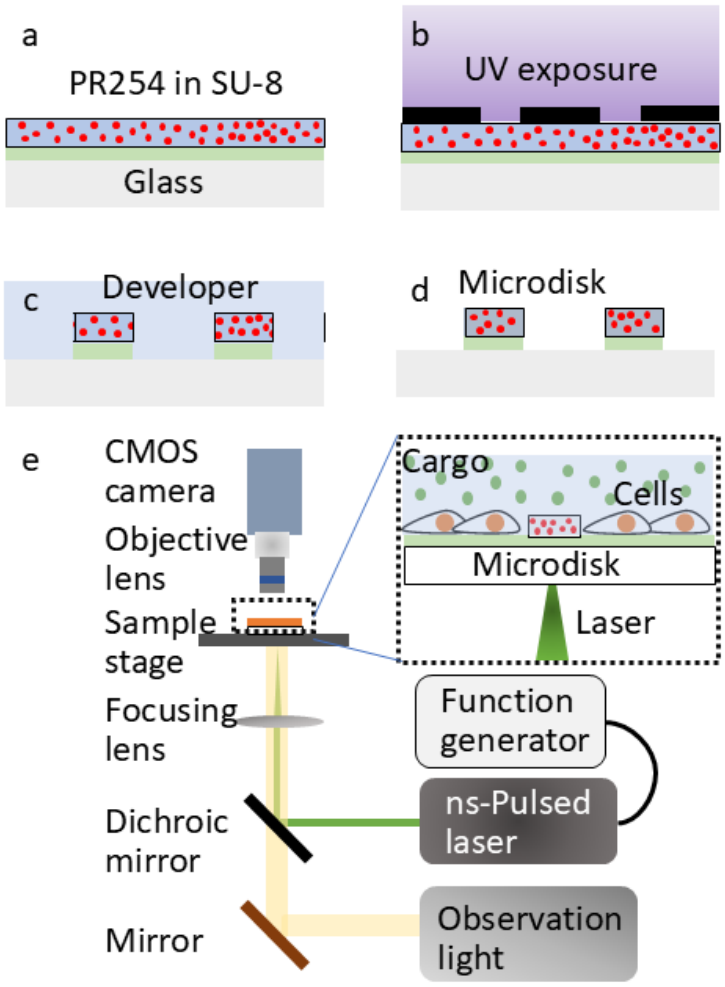

Figure 2.4 Schematic of microdisk fabrication and laser irradiation setup for the distance-dependent analysis method. (a)-(d) Steps in the fabrication of the pigmented SU-8 microdisk pattern. (e) Irradiation setup for optoporation, enabling precise control over shockwave magnitude and observation of cellular responses at different radial distances.

2.2.8 Optoporation Experiment, Image Acquisition, and Analysis

A pigmented SU-8 chip was placed on the sample stage, and cell-impermeable FITC dextran (1 mM, Mw 4000 Da, Sigma Aldrich, USA) was added over the chip before laser irradiation. A single pulse with a duration of 5 ns was utilized for irradiating the microdisks. After laser irradiation, the cells were immediately washed three times with PBS and incubated in 4 μM PI for the viability assay.

The micropattern substrate was placed on the stage of an inverted microscope (ECLIPSE Ti-2E, Nikon, Japan). The microscope was equipped with a camera (DS-Ri2, Nikon, Japan) and fluorescence cubes (B2-A and G-2A Nikon, Japan). Exposure time was optimized for each sample while maintaining consistent exposure conditions within the experimental group. Three images were obtained from each experiment, and 5 experiments were performed. All reported delivery efficiency and cell viability data were obtained from the 15 images obtained from experiments. Area divisions of three concentric circles with radii of 40 μm, 80 μm, and 120 μm were drawn using a Python script. Then obtained images were processed with background correction with a rolling ball radius of 2 in ImageJ and the cells were manually counted using the multipoint tool of ImageJ software in all three regions (25–40 μm, 40–80 μm, and 80–120 μm) for 50 μm microdisk and (10–40 μm, 40–80 μm, and 80–120 μm) for 20 μm were counted to evaluate delivery efficiency, cell viability and delivery yield after treatment with the laser irradiation on micropattern.

The delivery efficiency η_D, cell viability η_V, and delivery yield η_Y, were calculated from the total number of cells from brightfield images N_T, the number of dye-positive cells N_P, and the number of dead cells, N_D. They were determined by the following Eq. 2.8, 2.9, and 2.10:

$$\eta_D = \frac{N_P}{N_T} \qquad \ldots(2.8)$$

$$\eta_V = \frac{(N_T - N_D)}{N_T} \quad \ldots(2.9)$$

$$\eta_Y = \eta_P \eta_V \quad \ldots(2.10)$$

Fluorescence appeared in the micropattern structure upon laser irradiation. It was observed with/without cells. This fluorescence was excluded from cell counting and not further investigated.

2.2.9 Statistical Analysis

The delivery efficiency (η_D), cell viability (η_V), and delivery yield (η_Y) were analysed using JASP 0.19.0.0 software. First, the Shapiro-Wilk test was performed to assess data normality. Since some variables showed non-normal distributions, non-parametric tests were employed for all analyses. The Kruskal-Wallis test was conducted to evaluate differences between groups. When the Kruskal-Wallis test indicated significant differences ($p < 0.05$), Dunn's post-hoc test with Bonferroni correction for multiple comparisons was performed. Statistical significance was set at $p_{bonf} < 0.05$.

2.3 Experimental Results

2.3.1 Fabrication of Optical Absorber Disks

SU-8 microdisks containing PR-254 were formed on a glass wafer by photolithography. Micro-optical energy absorbers were patterned, and chips were obtained (Figure 2.5(a)). For the 20 μm design diameter (D.D.) diameter, and the approximate fabricated diameter (F.D.) of the disks was 24±1.5 μm (N=25) (Figure 2.5(b)) and 12 chips were obtained from one wafer with a pattern yield of 91.4±8.60% (mean ± standard deviation, number of measured wafers: N = 6)(Figure 2.5(c)). The microdisks with D.D. of 50 μm had an average F.D. of 57.5±1.0 μm (N=25) (Figure 2.5(b)) and were obtained with an average yield of 95.5±2.5% (number of measured wafers: N=6) (Figure 2.5(c)). Fabricated microdisks were found to be larger than the design value. With increasing D.D. size, the

error increased. This difference in diameter was probably because the resolution of the film mask used in this experiment was limited, and the corners of the pattern were not fully transferred.

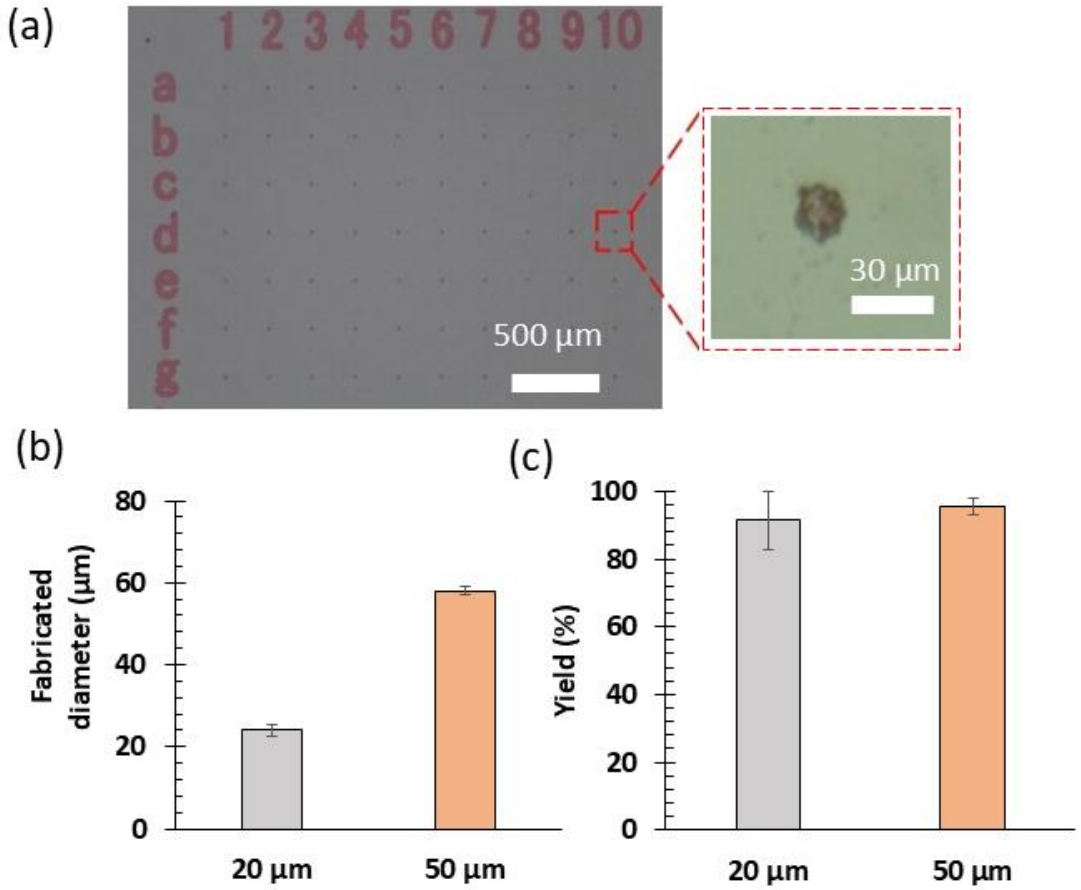

Figure 2.5 Fabricated pigmented microdisks. (a) Microscope image showing microdisks with 20 µm design diameters. (b) Fabricated diameters. (c) Fabrication yields for 20 µm and 50 µm microdisk patterns.

2.3.2 Characterization of Laser-Induced Bubble Formation

We evaluated the probability of bubble formation at laser fluences of 36 mJ/cm^2, 43 mJ/cm^2, 49 mJ/cm^2, 51 mJ/cm^2, 58 mJ/cm^2, 126 mJ/cm^2, 164 mJ/cm^2, 200 mJ/cm^2, and 514 mJ/cm^2 on the micropattern disks of 50 µm diameter. We measured the probability of bubble generation, which is

indicated in Figure 2.6(a) (n=20 microdisks). Only laser fluences with 100% bubble formation probability were considered for further experiments measuring bubble size.

Figure 2.6(b)–(i) shows the generation of larger bubble sizes with diameters of 50 μm and increasing laser fluences from 126 mJ/cm², 164 mJ/cm², 200 mJ/cm², to 514 mJ/cm². The 50 μm micropattern exhibited larger bubble sizes under the same energy conditions, with measurements of approximately 12.0±1.0 μm, 19.2±1.5 μm, 23.2±1.7 μm, and 42.2±1.0 μm (n=5) (Figure 2.6(j)). In contrast, for the 20 μm micropattern, the bubble sizes recorded were approximately 4.4±0.4 μm, 7.0±1.3 μm, 10.7±0.6 μm, and 20.9±1.4 μm (n=5) as the energy increased from 126 mJ/cm² to 514 mJ/cm² (Figure 2.6(k)).

Larger energy was absorbed in the 50-μm pattern, and allowed for greater accumulation of gas and subsequent bubble growth. The increase in energy input results in more vigorous gas generation and larger bubbles for both patterns, but the effect is more pronounced in the larger micropattern due to its enhanced capacity to sustain larger bubbles.

Notably, at 514 mJ/cm^2 laser fluence, we observed complete removal of the micropattern disc during some irradiation events. However, this removal was not consistent across all microdisks. The observed phenomenon is likely due to localized overheating or rapid gas expansion within the pattern, which occasionally disrupts the physical structure.

Overall, this analysis suggests that micropattern size plays a critical role in determining bubble dynamics during laser-induced processes and eventually contributes to the generation of perforation effects on the cell membrane.

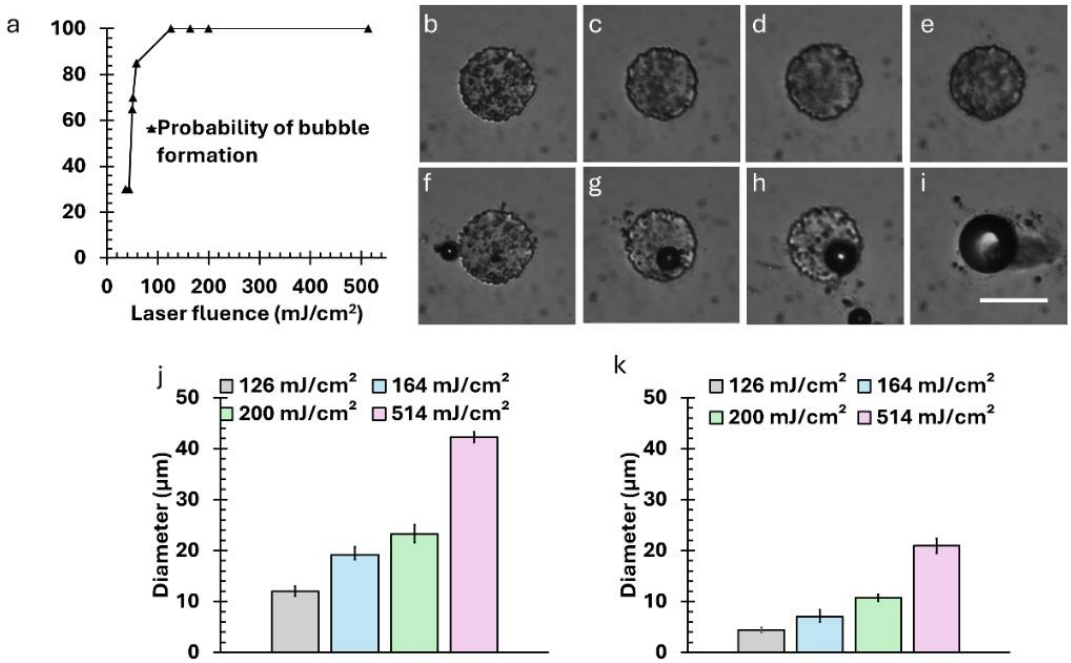

Figure 2.6 Bubble formation characteristics of microdisks. (a) Probability of bubble generation at various fluences for a 50 µm microdisk. Images of 50 µm microdisk. (b)–(e) Before pulse laser irradiation. (f)–(i) After laser pulse irradiation with 126 mJ/cm^2, 164 mJ/cm^2, 200 mJ/cm^2, 514 mJ/cm^2. Scale bar is 50 µm. (j) Bubble diameter measurement with 50-µm microdisk. (k) Bubble diameter measurement with 20 µm microdisk.

2.3.3 Shockwave-Induced Pressure Measurement

Figures 2.7(a) to 2.7(h) represent the propulsion of polystyrene microparticles upon irradiation of a 50-µm microdisk with various laser fluences. The study of laser-induced shock waves on micropatterns with diameters of 50 µm and 20 µm provides a detailed understanding of how shock wave pressure and particle displacement behave under varying conditions. At the chosen radial distances, the displacement of microsphere particles increased with higher laser energy levels, resulting in increased shock wave pressure for each micropattern size (Figure 2.7(i) and 2.7(k)).

Figures 2.7(j) and 2.7(l) describe the measurement of shockwave pressure from the 50-µm and 20-µm micropatterns, P_{25} ranged from approximately 6.8±0.9 MPa at an energy level of 126 mJ/cm²

to about 16.2±0.6 MPa at 514 mJ/cm². While the P_{10} for the smaller 20 μm microdisk ranged in the range of 5.2±0.4 MPa at 126 mJ/cm^2 to 13.2±1.4 MPa at the laser fluence of 514 mJ/cm^2. This uniformity likely results from similar initial forces exerted by the shockwave on both micropatterns due to uniform energy distribution at the impact point.

However, as the radial distance increases, the resultant pressure magnitude differs significantly between the two micropattern sizes due to the decay of the shock wave. At a radial distance of 40 μm, for instance, P_{40} for the 50-μm pattern ranged from 2.6±0.3 MPa to 6.3±0.6 MPa across energy levels from 126 mJ/cm² to 514 mJ/cm², while for the 20-μm pattern, it ranged from only 0.3±0.02 MPa to 0.7±0.08 MPa. This trend continued at greater distances; at 80 μm, pressures P_{80} for the larger pattern ranged from 0.6±0.08 MPa to 1.4±0.1 MPa compared to just 0.07±0.0 MPa to 0.19 ± 0.02 MPa for the smaller pattern. At 120 μm, P_{120} further decreased to between 0.2±0.03 MPa and 0.6±0.07 MPa for the larger pattern and between 0.03±0.0 MPa and 0.09±0.0 MPa for the smaller micropattern. These results highlight how shock wave pressure diminishes more rapidly with distance in smaller patterns due to their reduced capacity to sustain wave propagation over longer distances, emphasizing the importance of micropattern size in applications requiring precise control over shock wave effects.

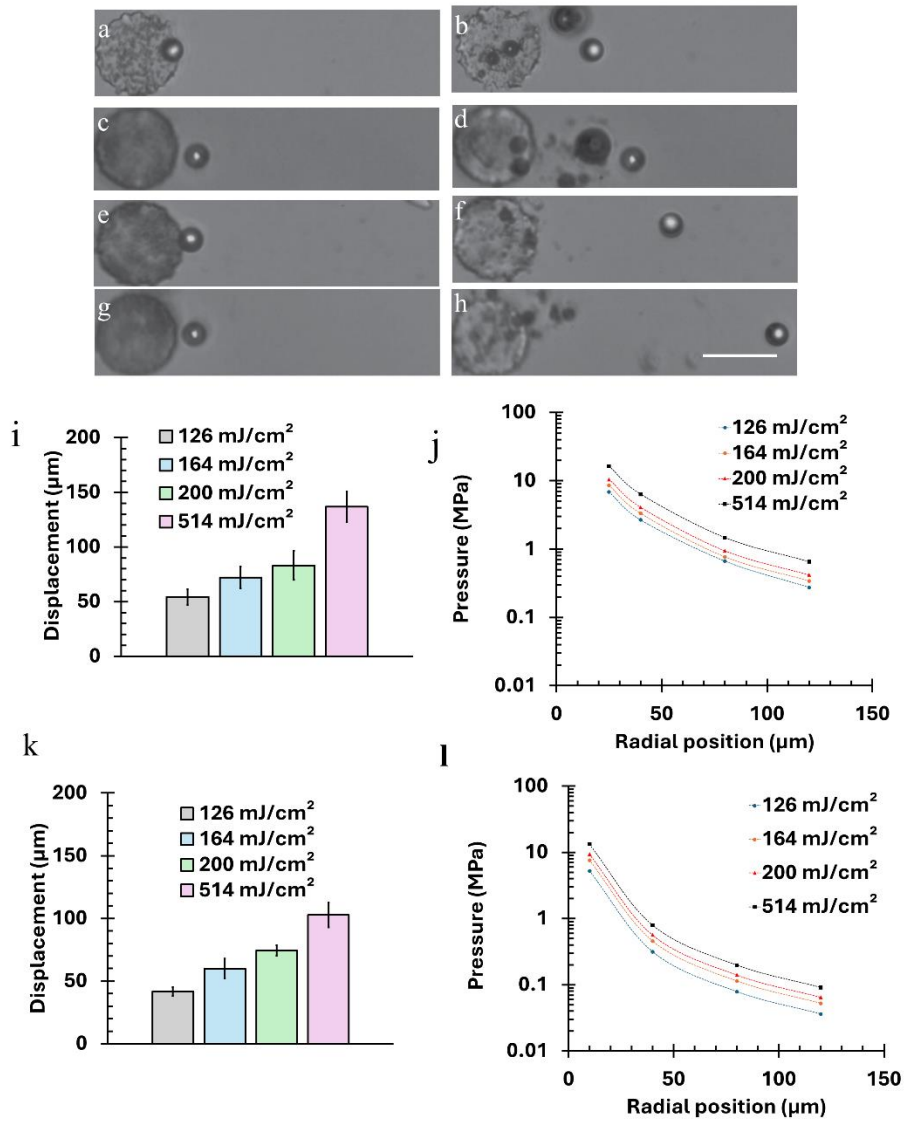

Figure 2.7 Propulsion of polystyrene microbead upon laser irradiation. Microscope images with a 50-µm microdisk at various laser fluence. (a-b) 126 mJ/cm². (c-d) 164 mJ/cm². (e-f) 200 mJ/cm². (g-h) 514 mJ/cm². Scale bar is 50 µm. (i) Measured displacement of particles using a 50-µm microdisk. (j) Pressure measurements as a function of radial distance from a 50-µm microdisk. (k) Measured displacement of particles using a 20-µm microdisk. (l) Pressure measurements as a function of radial distance from the 20-µm microdisk.

2.3.4 Optoporation of HeLa Cells with 50 μm Disk

Figures 2.8 and 2.9 show the effect of pattern size on micropattern-assisted optoporation with PR254 microdisks with diameters of 50 μm at laser fluences of 126 mJ/cm^2, 164 mJ/cm^2, 200 mJ/cm^2, and 514 mJ/cm^2. Figure 2.8 (a)–(l) display fluorescence images of optoporated cells using 50 μm diameter disks. The laser irradiation of the 50 μm pattern resulted in intracellular delivery of FITC dextran 4 kDa into cells (Figure 2.8(b), (e), (h), (k)). Upon laser irradiation on the micropattern, cell viability was compromised in Figure 2.8((c), (f), (i), (l)), indicating the influence of cell peeling or cell necrosis on the evaluated η_D, η_V, and η_Y. No dead or optoporated cells were observed in the absence of laser irradiation of cells cultured on a micropatterned substrate, and in the absence of micropatterns with laser irradiation on a cell monolayer on a glass substrate.

Figures 2.8(m)–(o) show η_D, η_V, and η_Y with a 50-μm microdisk at various radial distances and laser fluences. Intuitively, η_D should be higher closer to the area of laser irradiation, but the calculation of delivery is affected by cells either peeling off or undergoing necrosis, affecting η_Y at a given fluence and radial distance. The cell response of HeLa cells to micropattern laser irradiation at 126 mJ/cm² and to 514 mJ/cm² visually demonstrates the difference in cell response at varying laser parameters.

The analysis of delivery yield (η_Y) across different distances revealed complex relationships between delivery efficiency and laser fluence. In the 25–40 μm region, while the delivery efficiency at 514 mJ/cm² (51.3±12.0%, average N_T =5 cells) was significantly higher than at 126 mJ/cm² (36.0±13.2%, average N_T =7 cells, p_{bonf} =0.04), the final delivery yields remained statistically equivalent (32.0±15.1% at 514 mJ/cm² versus 27.1±11.3% at 126 mJ/cm², p_{bonf} =1). At greater distances with 514 mJ/cm², despite reduced cell viability, substantial delivery yields were maintained, reaching 34.7±6.5% in the 40–80 μm region (delivery efficiency 48.4±7.9%, average N_T =22 cells) and 39.07±14.4% in the 80–120 μm region (delivery efficiency 45.5±16.4%, average N_T =35 cells). These results demonstrate that while higher laser fluence initially produces greater delivery efficiency, the final yield remains consistent across distances due to the counterbalancing effects of cell viability.

Analysis of delivery at the same energy and different ranges shows an inverse relationship between distance from the laser irradiation point and cellular response: as distance increased, delivery efficiency (η_D) decreased while cell viability (η_V) increased. Using the 50 μm pattern at high laser fluence (514 mJ/cm²), uniform shockwave effects were observed throughout the 25–120 μm region, resulting in a non-significant difference in yields from 25–40 μm to 40–80 μm (p_{bonf} =1), and from 40–80 μm to 80–120 μm (p_{bonf} =0.62).

At 200 mJ/cm², a clear trade-off emerged between delivery efficiency and cell viability in different regions. The 40–80 μm region exhibited higher delivery efficiency (28.1±9.7%) despite lower cell viability (73.6±9.5%), while the 80–120 μm region showed reduced delivery efficiency (21.4±6.8%) but enhanced cell viability (86.7±5.7%). These counterbalancing effects resulted in non-significant delivery yields (p_{bonf} =1) between regions. Lower laser fluences (164 mJ/cm² and 126 mJ/cm²) displayed similar patterns, with the 40–80 μm region achieving higher delivery efficiency but reduced viability compared to the 80–120 μm region.

Analysis of delivery at the same energy and different ranges reveals a key trade-off: as distance from the laser irradiation point increases, intracellular delivery efficiency decreases, while cell viability correspondingly increases. Consequently, regions closer to the irradiation site achieve higher delivery efficiency at the expense of lower cell viability, while regions farther away exhibit improved viability but lower efficiency. Despite these opposing trends, the final delivery yield remains comparable due to counterbalancing effects. From these observations, the 25–80 μm range emerges as the optimal zone, providing the most favorable balance between delivery and cell health. This finding highlights the critical need for spatial targeting to optimize optoporation performance.

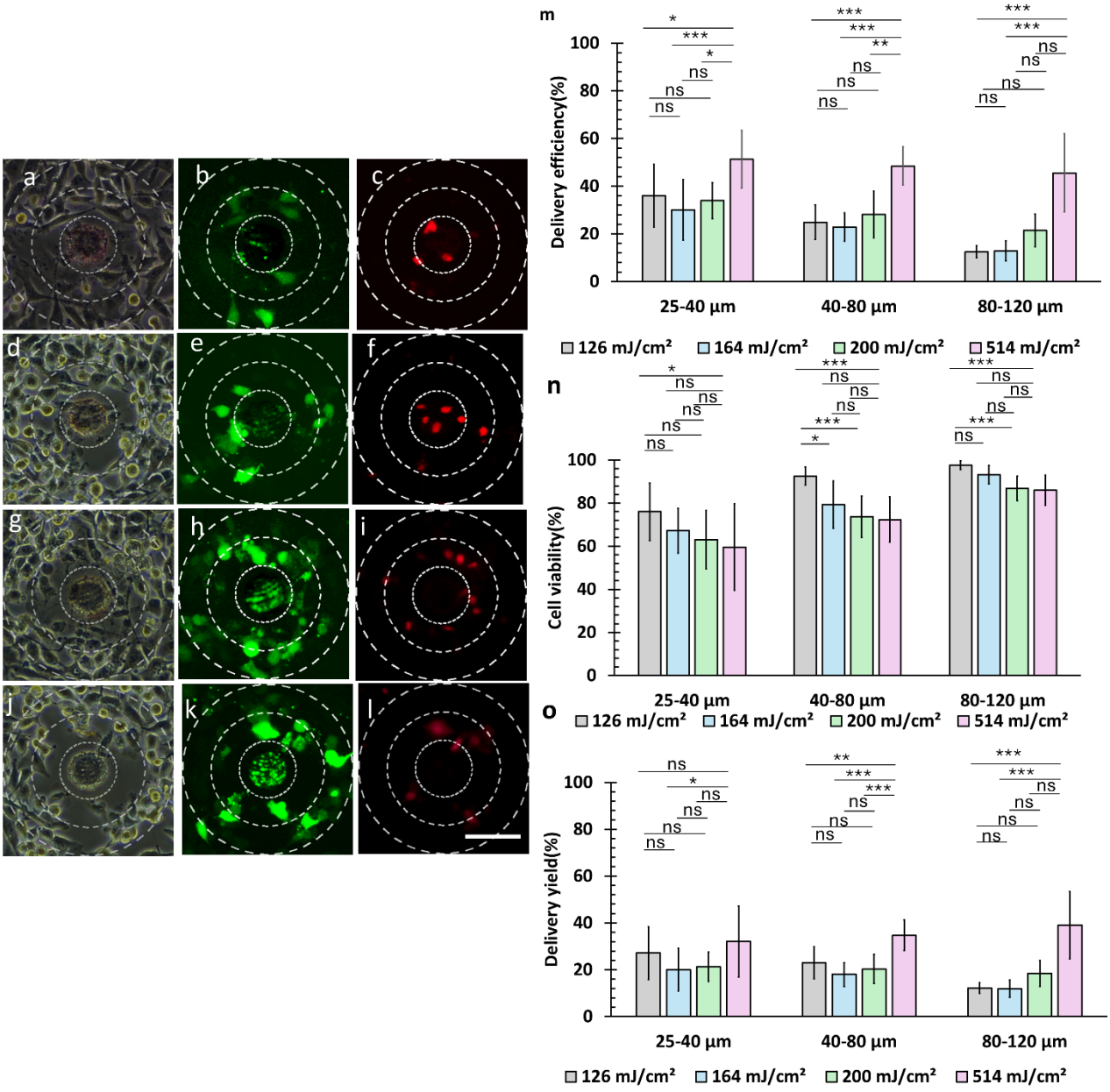

Figure 2.8 Laser fluence affects optoporation efficiency and cell viability in HeLa cells using a 50 µm diameter microdisk. (a–l) Representative images showing brightfield (left column), FITC-positive cells indicating successful delivery (green, middle column), and dead cells (red, right column) at different laser fluences. (a–c) 126 mJ/cm². (d–f) 164 mJ/cm². (g–i) 200 mJ/cm². and (j–l) 514 mJ/cm². Scale bar is 80 µm. (m) Delivery efficiency. (n) Cell viability. (o) Delivery yield as a function of laser fluence and distance from the irradiation point.

2.3.5 Optoporation of HeLa Cells with 20 μm Disk

The study revealed distinct differences in cellular responses between 20 μm and 50 μm microdisk patterns, with the smaller disk generating lower magnitude shockwaves across all measured distances (40 μm, 80 μm, and 120 μm). Fluorescence imaging demonstrated successful intracellular molecule delivery near the laser spot when using the 20 μm disk, achieving delivery patterns similar to those observed with the 50 μm pattern (Figure 2.9(b), 2.9(e), 2.9(h), 2.9(k)). Green fluorescence was observed near the laser spot on the disk.

Analysis of the 20-μm microdisk revealed distinct delivery characteristics compared to the 50-μm microdisk. Figures 2.9(m), 2.9(n), and 2.9(o) show η_D, η_V, and η_Y, respectively, for the 20-μm microdisk pattern. Unlike the case with the 50-μm microdisk, η_D showed less impact from cell necrosis and peeling while maintaining higher cell viability. As suggested by the microbubble size patterns observed in the previous section, η_D increased proportionally with laser fluence.

In the range of 10–40 μm, the highest η_Y was obtained at a laser fluence of 514 mJ/cm^2 (Figure 2.9(o)), significantly exceeding the yield at 126 mJ/cm^2 in the 10–40 μm region. This superior performance extended to the 40–80 μm region, where 514 mJ/cm^2 demonstrated significantly higher yields compared to both 126 mJ/cm^2 and 164 mJ/cm^2, with similar results in the 80–120 μm range. A delivery yield of 32.6±13.2% (average N_T = 6 cells) was obtained in the 10–40 μm range. The η_Y exhibited a distance-dependent decline, reaching 29.2±8.3% at 40–80 μm (average N_T = 20 cells) and 18.5±5.3% at 80–120 μm (average N_T = 34 cells) at 514 mJ/cm^2.

Statistical analysis of delivery at the same energy at different radial distances revealed that at the same energy, delivery efficiency for laser fluences of 514 mJ/cm^2 and 200 mJ/cm^2 showed significant differences only between the 40–80 μm and 80–120 μm ranges (p_{bonf} = 0.008 for both fluences). At 164 mJ/cm^2, significant differences were observed across all regions. At 126 mJ/cm^2,

only the regions between 40–80 μm and 80–120 μm showed highly significant differences (p_{bonf} = 0.002), likely due to minimal shockwave effects in the 80–120 μm regions.

Overall, the results from irradiation at the same energy indicate that the spatial extent and uniformity of laser-induced cellular effects are strongly influenced by laser fluence. At higher fluences, such as 514 mJ/cm² and 200 mJ/cm², shockwave effects extend farther from the irradiation point, resulting in significant differences in delivery efficiency primarily between mid-range (40–80 μm) and far-range (80–120 μm) regions. In contrast, at lower fluences, these effects become more spatially restricted, with significant differences observed across all regions at 164 mJ/cm², and highly localized effects at 126 mJ/cm², where only the 40–80 μm and 80–120 μm regions differ significantly. These results indicate that higher laser fluence enhances the effective range of optoporation, enabling delivery to cells located farther from the micropattern, whereas lower fluence limits delivery to cells in closer proximity. Therefore, adjusting laser energy is crucial for controlling the spatial reach and uniformity of cellular response in optoporation applications.

A comparison between the 50-μm and 20-μm microdisk patterns revealed distinct impacts on cell response during optoporation, with each pattern showing unique distance-dependent characteristics. While the 50-μm microdisk pattern exhibited more aggressive effects through significant cell detachment and necrosis that impacted the overall delivery process, the 20-μm microdisk pattern demonstrated more controlled effects with proportionally increasing delivery efficiency at higher laser fluence while maintaining better cell viability. For cells within 40 μm of the irradiation site, the 20-μm microdisk achieved comparable delivery efficiencies with enhanced viability, whereas the 50-μm pattern proved more effective for targeting HeLa cells at distances beyond 40 μm, suggesting that pattern size selection should be optimized based on the specific application requirements, considering both target distance and the desired balance between delivery efficiency and cell viability.

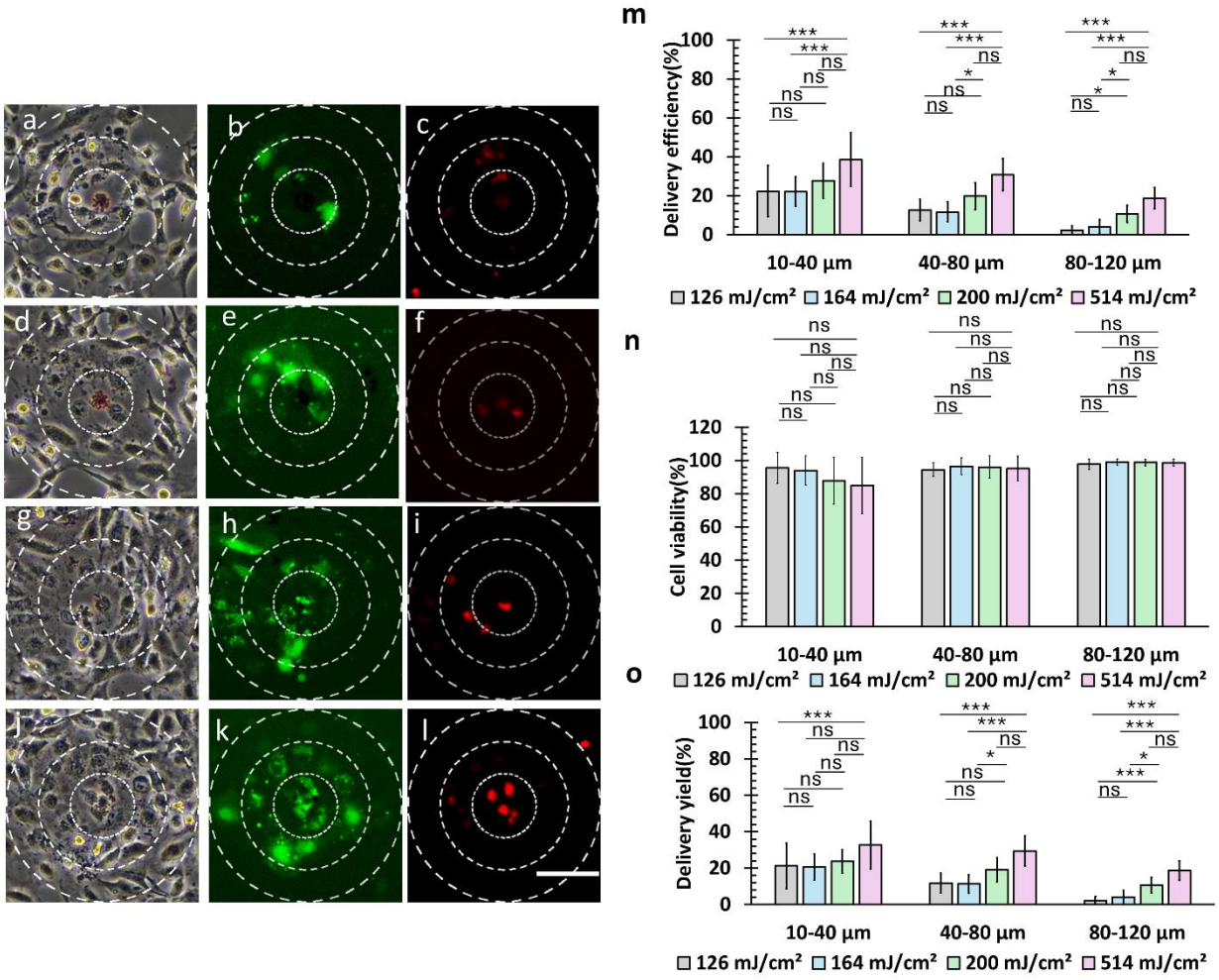

Figure 2.9 Optoporation of HeLa cells using a 20-µm-diameter microdisk at various laser fluences. (a-c) 126 mJ/cm². (d-f) 164 mJ/cm². (g-i) 200 mJ/cm². and (j-l) 514 mJ/cm². For each fluence, the left column shows brightfield images, the middle column shows FITC-positive cells (green, indicating successful delivery), and the right column shows dead cells (red). Scale bar is 80 µm. (m) Delivery efficiency. (n) Cell viability. (o) Delivery yield measured as a function of laser fluence and distance from the irradiation point.

2.3.6 Optoporation of HEK-293 and SAOS-2 Cells with 20 µm Disk

The versatility of micropattern optoporation was investigated using 20-µm diameter disks to deliver FITC-dextran into different cell lines, comparing weakly adhering HEK-293 cells (Figure 2.10)

and SAOS-2 cells (Figure 2.11) with HeLa cells as a reference. Due to their semi-adherent nature, HEK-293 cells demonstrated distinct responses in delivery efficiency (η_D), cell viability (η_V), and delivery yield (η_Y) when exposed to laser pulses at various fluences. Cellular responses to 20 μm microdisk pattern irradiation at 514 mJ/cm^2 laser fluence revealed variations among cell types, with HEK-293 cells showing extensive cell peeling and necrosis, while SAOS-2 cells exhibited reduced delivery effects compared to HeLa cells.

The delivery efficiency measurements, displayed in Figure 2.10(m), demonstrated that laser and micropattern parameters affected cells differently based on their adhesion strength. HEK-293 cells exhibited increased susceptibility to necrosis and peeling at greater distances due to their physical properties, showing more pronounced effects compared to HeLa cells. As evidenced in Figures 2.10(a), 2.10(d), 2.10(g), and 2.10(j), HEK-293 cells primarily experienced cell peeling and cell necrosis, attributable to their lower adhesion strength. The delivery efficiency consistently decreased with increasing radial distance, confirming the spatial extent of laser-induced effects.

The delivery yield analysis revealed distinct patterns at different radial distances from the irradiation point. At the highest laser fluence of 514 mJ/cm², extensive cell necrosis and peeling made evaluation impossible in the proximal 10-40 μm region, as evidenced in Figures 2.10(j) and 2.10(k). Among lower fluences in this region, statistical analysis showed no significant differences in delivery yield (p_{bonf} = 1 for 200 mJ/cm² vs 164 mJ/cm², p_{bonf} = 0.2 for 200 mJ/cm² vs 126 mJ/cm², and p_{bonf} = 0.3 for 126 mJ/cm² vs 164 mJ/cm²). Notably, at greater distances from the irradiation point, 514 mJ/cm² achieved the highest delivery yields despite compromised cell viability, reaching 60.3±8.8% (N_T = 31 cells) in the 40-80 μm region and 31.7±12.1% (N_T = 60 cells) in the 80–120 μm region.

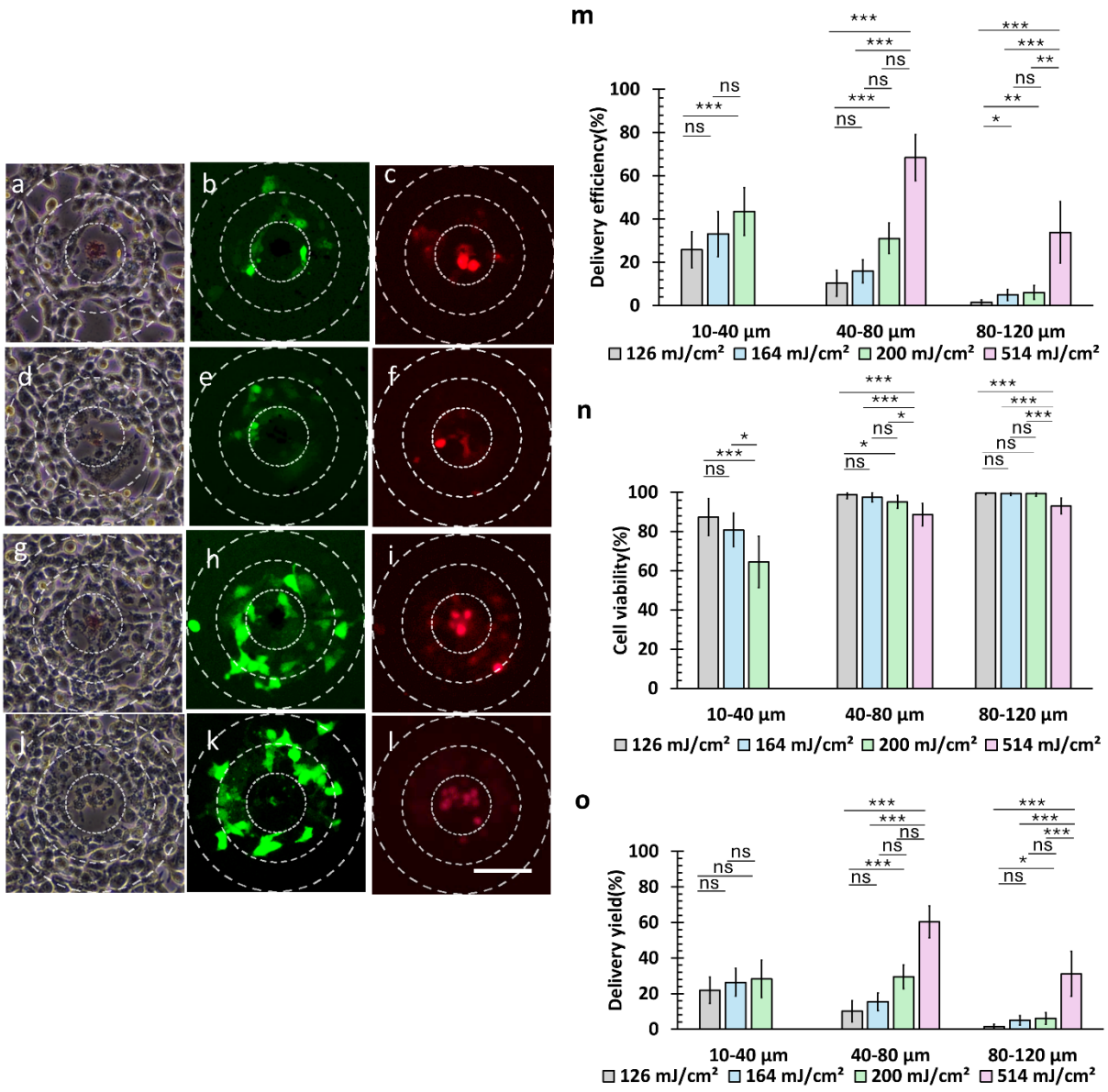

Figure 2.10 Optoporation of HEK-293 cells using a 20-µm diameter microdisk. (a–c) 126 mJ/cm². (d–f) 164 mJ/cm². (g–i) 200 mJ/cm². and (j–l) 514 mJ/cm². For each fluence: the left column shows brightfield images, the middle column shows FITC-positive cells (green, indicating successful delivery), and the right column shows dead cells (red). Scale bar is 80 µm. (m) Delivery efficiency. (n) Cell viability. (o) Delivery yield measured as a function of laser fluence and distance from the irradiation point.

Statistical analysis at same energy at different radial distance revealed significant differences for lower fluences (126 and 164 mJ/cm²) between the regions of 10–40 μm and 40–80 μm (p_{bonf} = 0.04 for both fluences) and between the 40–80 μm and 80–120 μm regions (p_{bonf} = 0.002 for both fluences). For higher energies of 200 mJ/cm^2 and 514 mJ/cm^2, significant differences were only observed between 40–80 μm and 80–120 μm regions (p_{bonf} < 0.001 for both fluences). These findings demonstrate that while lower laser fluences produced similar effects at shorter distances, higher fluences showed comparable effects at greater distances from the irradiation point, suggesting a distance-dependent relationship between laser fluence and delivery effectiveness.

Compared to HeLa cells, HEK-293 cells showed greater sensitivity to laser-induced effects at shorter distances. Significant delivery differences were observed even between proximal regions under low fluence, indicating that delivery in HEK-293 cells is more spatially localized and dependent on distance from the irradiation point. In contrast, HeLa cells exhibited broader effective delivery zones and higher tolerance to shockwave-induced stress, resulting in more uniform delivery across wider regions. These differences likely stem from variations in membrane composition, adhesion strength, and mechanical properties.

Fluorescence imaging of SAOS-2 cells during micropattern optoporation (Figure 2.11) revealed their unique resistance to perforation, reflected in both delivery efficiency and cell viability measurements. These cells demonstrated remarkable resilience, with neither cell necrosis nor detachment observed across all tested laser fluences, while maintaining 100% cell viability (η_V) throughout all laser irradiation conditions. While no delivery was detected at 126 mJ/cm^2, the delivery efficiency showed a consistent pattern: decreasing with increasing radial distance while increasing within the same radial distance as laser fluence increased.

The optimal delivery yield (η_Y) was achieved at maximum laser fluences across all distances, with both delivery efficiency (η_D) and delivery yield reaching their peak values. The measurements

showed 41.0±10.8% (average N_T = 4 cells) in the 10–40 μm range, declining to 28.7±9.8% (average N_T = 14 cells) at 40–80 μm, and further decreasing to 18.6±9.5% (average N_T = 22 cells) at 80–120 μm (Figure 2.11l). These values were significantly higher than those observed at other laser fluences, demonstrating the effectiveness of higher laser fluences for delivery.

Statistical analysis at the same energy at different radial distances revealed significant differences in delivery yield between the 40–80 μm and 80–120 μm regions (p_{bonf} = 0.009 at 164 mJ/cm² and p_{bonf} = 0.001 at 200 mJ/cm²). The delivery yield showed a consistent decrease with increasing radial distance at any given energy level. At the highest laser fluence, significant differences emerged between the 10–40 μm and 40–80 μm regions (p_{bonf} = 0.04). These findings demonstrate that while lower laser fluences produced similar effects at shorter distances, higher fluences showed comparable effects at greater distances from the irradiation point, suggesting a distance-dependent relationship between laser fluence and delivery effectiveness.

Like the other cell types tested, delivery efficiency in SAOS-2 cells decreased with increasing radial distance from the laser. However, unlike those cells, SAOS-2 cells maintained high viability across all conditions. Statistical analysis confirmed that significant spatial differences in delivery yield still occurred, especially at higher fluences. Despite these differences, the consistently high viability makes SAOS-2 uniquely suited for high-intensity optoporation. This resilience distinguishes SAOS-2 from HeLa cells, which exhibit moderate tolerance and broader delivery zones, and HEK cells, which show greater sensitivity to short-range effects, highlighting cell-type-specific variations in shockwave response and membrane robustness.

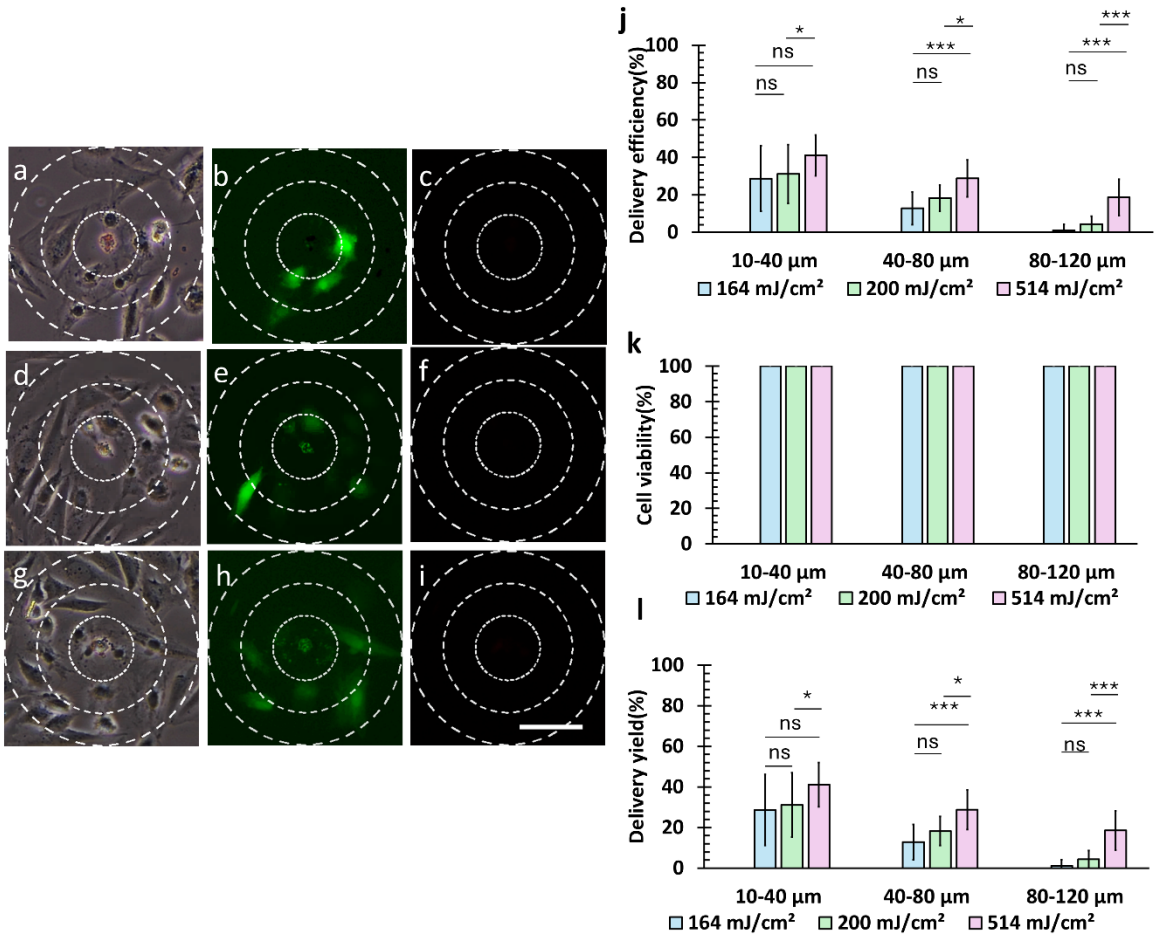

Figure 2.11 Optoporation of SAOS-2 cells using a 20-µm diameter microdisk. (a–c) 164 mJ/cm². (d–f) 200 mJ/cm². (g–i) 514 mJ/cm². For each fluence, the left column shows brightfield images, the middle column shows FITC-positive cells (green, indicating successful delivery), and the right column shows dead cells (red). Scale bar is 80 µm. (j) Delivery efficiency. (k) Cell viability. (l) Delivery yield measured as a function of laser fluence and distance from the irradiation point.

2.4 Discussion

2.4.1 Novelty of Methodology and Setup

This study introduces a novel approach for investigating laser-irradiated micropattern-induced bioeffects on cell monolayers using modified substrates. The methodology enables the identification of multiple sites and facilitates long-term cell monitoring, overcoming significant challenges related

to site-specific response faced in previous studies [46, 47] where the laser was randomly irradiated on the substrate, making the task of identifying the irradiation sites highly time-consuming and tedious.

While laser irradiation has been extensively studied to optimize parameters for minimizing cell damage [48, 49], previous experiments without photoabsorbers faced difficulties in characterizing radial effects on cell monolayers. The identification of multiple sites and long-term cell monitoring posed challenges. [44, 47]. Our approach using modified substrates with micropatterns addresses these challenges by enabling precise identification of multiple irradiation sites and facilitating sustained observation of cellular responses.

2.4.2 Cell-Type Specific Responses

The cellular response to micropattern-generated bio-effects demonstrated significant variation across different cell types, with pattern size playing a crucial role in delivery outcomes. When using the 50-μm microdisk pattern, HeLa cells exhibited compromised delivery efficiency due to extensive cell detachment and necrosis throughout the 0–120 μm range. However, the 20-μm microdisk pattern generated smaller shockwaves that maintained delivery efficiency while minimizing cellular damage.

The investigation of multiple cell lines revealed that cellular adhesion strength significantly influenced the response to shockwave exposure. SAOS-2 cells demonstrated remarkable resilience when exposed to 20-μm microdisk-generated shockwaves, maintaining cellular integrity without experiencing necrosis or detachment. In stark contrast, HEK-293 cells, characterized by weaker adhesion properties, exhibited heightened sensitivity to the shockwaves, resulting in reduced delivery efficiency and diminished cell viability across an extended range. These findings highlight the importance of considering cell-specific characteristics when optimizing micropattern-assisted optoporation parameters.

2.4.3 Mechanism Analysis

Upon irradiation of a laser pulse on the micropattern, although visible plasma light emission (sparks) was not directly observed, laser-induced breakdown or localized plasma production below our detection threshold could still occur. Indeed, the main sources of laser-irradiated micropattern-induced bioeffects in this system are probably laser-induced breakdown and plasma generation on the microdisk. The PR-254/SU-8 surface is rapidly heated by the 532-nm, 5-ns laser pulse, which causes a small layer of water at the interface to evaporate and then explode into bubbles. Although we cannot define a precise breakdown threshold, the onset of bubble formation could be considered a practical threshold for significant material modification. The mechanism likely involves rapid heating of the micropattern surface, vaporization of a thin water layer, and subsequent bubble nucleation and growth, which would contribute to the observed bioeffects.

Our nanosecond pulsed laser study revealed that micropattern size and laser fluence significantly influence cellular responses through three primary mechanisms affecting membrane integrity. Larger micropatterns contributed to increased cell necrosis and detachment over greater distances, impacting delivery efficiency in a cell type-specific manner. The analysis of these mechanisms is crucial for understanding the observed changes in cell membrane integrity: a) Expansion and collapse of a cavitation bubble, b) Laser-induced shockwave upon micropattern irradiation, and c) Heat transfer between the micropattern and cells.

The first mechanism involves rapid photothermal absorption upon laser irradiation of micropatterned surfaces, leading to cavitation bubble formation through optical breakdown and vaporization. These bubbles undergo explosive expansion and subsequent collapse, generating high velocity microjets that exert significant mechanical stress on nearby cell membranes [50–52]. This process results in transient perforation and enhanced membrane permeability through the mechanical forces generated during bubble dynamics.

At shorter timescales, the second mechanism occurs when PR-254/SU-8 surfaces experience rapid heating from the 532-nm, 5-ns laser pulse, inducing a phase change in the adjacent water layer. This generates supersonic shock waves, whose propagation creates transient stress fields in the surrounding medium, causing membrane deformation and temporary disruption of the phospholipid bilayer structure [46, 53].

The third mechanism involves localized thermal effects, where heat transfer from micropatterns leads to the formation of short-lived hydrophilic pores through lipid bilayer denaturation, enhancing membrane permeability to various molecules [54]. These mechanisms collectively depend on the interaction between the target surface and laser irradiation, with larger micropatterns producing more pronounced bioeffects on the cell monolayer while smaller micropatterns cause less bioeffects.

Given the complexity of these rapid physical phenomena occurring at very short time scales, further investigation using advanced techniques such as time-resolved spectroscopy, high-speed imaging, and molecular dynamics simulations would enhance our understanding of the induced bioeffects, ultimately enabling optimized designs for specific applications in biophotonic cell manipulation.

2.4.4 Comparison to Previously Reported Similar Studies

In this section, we compare our micropattern-assisted, site-specific optoporation method to previously reported studies that also utilized single-pulse laser irradiation or targeted laser exposure at specific cell sites. Traditional single-point optoporation approaches have primarily relied on direct laser irradiation of individual cells on standard culture substrates. While these methods demonstrate localized perforation and successful intracellular delivery, they are inherently low throughput, as each cell must be individually targeted and irradiated. This manual or semi-automated targeting introduces significant challenges in relocating and aligning cells for repeated or large-scale processing, making it impractical for applications requiring the treatment of thousands of cells in parallel.

In contrast, our approach introduces a patterned substrate embedded with photoabsorbing microdisks, enabling simultaneous irradiation of multiple cells located on predefined micropatterns with a single laser pulse. This design transforms the optoporation process from a single-cell, labor-intensive method into a massively parallel, spatially predictable platform. Each microdisk acts as a localized energy converter that generates a confined shockwave upon laser irradiation, transiently permeabilizing the membranes of cells cultured above it. Because the micropattern layout is predefined during fabrication, the location of treated cells is inherently site-specific and easily relocatable for post-treatment analysis, imaging, or subsequent therapeutic steps.

Compared to previous site-specific optoporation studies—where laser beams had to be manually focused and scanned over individual cells—our method achieves parallel processing without requiring precise real-time beam steering or single-cell manipulation. This not only reduces operational complexity but also minimizes the risk of off-target exposure and cell loss. Furthermore, the micropattern-based approach allows tuning of disk size and spacing to control delivery efficiency and cell recovery rates, providing a level of adaptability that is challenging to achieve in conventional point-by-point laser irradiation methods.

Overall, our micropattern-assisted platform uniquely combines site specificity, high parallelism, and contactless laser processing, marking a significant advancement over earlier single-pulse, localized optoporation techniques. This innovation bridges the gap between single-cell precision and clinically relevant scalability, paving the way for next-generation high-throughput intracellular delivery systems. Table 2.1 represents the concise comparison of related studies to our method for optoporation.

Table 2.1 Comparison with previous reports.

Technique	Photoabsorber / Approach	Application focus	Efficiency / Viability	Unique Contribution	Reference
Femtosecond laser pore creation	None (direct laser interaction)	DNA plasmid entry via transient pores	Low plasmid entry (few copies), high viability	Quantitative pore resealing dynamics and delayed translocation mechanism	[55]
Nanosecond laser microbeams	Optical breakdown cavitation bubbles	Cell lysis and perforation	Viability depends on pulse energy and distance	Characterization of plasma-induced lysis zones	[44]
Femtosecond laser with microparticles	Plasmid-coated microparticles	Single-cell transfection	Low transfection efficiency	Single-cell precision with optical tweezers and microinjection	[56]
Nanosecond pulsed Nd: YAG laser.	Glass substrate (no absorber)	Bulk optoporation of adherent cells	High viability zone (>60 μm from the beam)	Distance-dependent molecular delivery efficiency	[57]
Micropattern-assisted Optoporation	Photoabsorber embedded micropatterns	Intracellular delivery on micropatterned cell culture substrate	61 % delivery yield	Spatially controlled micropattern-assisted delivery and dual transient/permanent perforation	Our work

2.5 Conclusions

In this chapter, we studied transient membrane pore creation with a micropattern-based cell culture substrate. A quantitative distance-dependent method was developed to evaluate laser-irradiated micropattern-induced bioeffects on intracellular delivery using pigmented SU-8 microdisks. This approach enabled precise control of both microdisk size and laser fluence while allowing direct observation of cellular responses at varying radial distances from the irradiation point. The effectiveness of the bioeffects was significantly influenced by two key factors: micropattern size and cell-type-specific characteristics.

The study revealed distinct responses between different cell types and pattern sizes. Larger micropatterns led to increased cell necrosis and detachment over broader ranges, while smaller micropatterns maintained comparable delivery efficiency with minimal cellular damage. Cell-specific properties played a crucial role in treatment outcomes, as demonstrated by the contrasting responses between SAOS-2 and HEK-293 cells. While SAOS-2 cells maintained their integrity throughout the

treatment, HEK-293 cells showed increased susceptibility to detachment and necrosis over larger distances.

This systematic analysis establishes a framework for optimizing laser and micropattern parameters in micropattern-assisted optoporation. The method offers advantages over conventional approaches through precise spatial control and real-time monitoring capabilities. These findings enhance our understanding of shockwave-mediated intracellular delivery mechanisms and provide practical guidelines for developing more effective therapeutic delivery strategies while preserving cell viability.

References

1. Naseri, N.; Valizadeh, H.; Zakeri-Milani, P. Solid Lipid Nanoparticles and Nanostructured Lipid Carriers: Structure Preparation and Application. Adv Pharm Bull 2015, 5, 305–313.
2. Kesharwani, P.; Jain, K.; Jain, N.K. Dendrimer as a Nanocarrier for Drug Delivery. Prog Polym Sci 2014, 39, 268–307.
3. Sharma, N.; Purwar, N.; Chandra Gupta, P. Microspheres As Drug Carriers For Controlled Drug Delivery: A REVIEW. Int J Pharm Sci Res 2015, 6, 4579.
4. Yadav, D.; Sandeep, K.; Pandey, D.; Dutta, R.K. Liposomes for Drug Delivery. J Biotechnol Biomater 2017, 07, 192-224.
5. Santra, T.S.; Chang, H.Y.; Wang, P.C.; Tseng, F.G. Impact of Pulse Duration on Localized Single-Cell Nano-Electroporation. Analyst 2014, 139, 6249–6258.
6. Santra, T.S.; Kar, S.; Chang, H.Y.; Tseng, F.G. Nano-Localized Single-Cell Nano-Electroporation. Lab Chip 2020, 20, 4194–4204.
7. Zhang, Y.; Yu, L.C. Microinjection as a Tool of Mechanical Delivery. Curr Opin Biotechnol 2008, 19, 506–510.
8. Liang, H.D.; Tang, J.; Halliwell, M. Sonoporation, Drug Delivery, and Gene Therapy. Proc Inst Mech Eng H 2010, 224, 343–361.
9. Shinde, P.; Kar, S.; Loganathan, M.; Chang, H.Y.; Tseng, F.G.; Nagai, M.; Santra, T.S. Infrared Pulse Laser-Activated Highly Efficient Intracellular Delivery Using Titanium Microdish Device. ACS Biomater Sci Eng 2020, 6, 5645–5652.
10. Yao, C.P.; Zhang, Z.X.; Rahmanzadeh, R.; Huettmann, G. Laser-Based Gene Transfection and Gene Therapy. IEEE Trans Nanobioscience 2008, 7, 111–119.
11. Yao, C.; Rudnitzki, F.; He, Y.; Zhang, Z.; Hüttmann, G.; Rahmanzadeh, R. Cancer Cell-Specific Protein Delivery by Optoporation with Laser-Irradiated Gold Nanorods. J Biophotonics 2020, 13, 1–10.

12. Wilson, A.M.; Mazzaferri, J.; Bergeron, É.; Patskovsky, S.; Marcoux-Valiquette, P.; Costantino, S.; Sapieha, P.; Meunier, M. In Vivo Laser-Mediated Retinal Ganglion Cell Optoporation Using KV1.1 Conjugated Gold Nanoparticles. Nano Lett 2018, 18, 6981–6988.

13. Soman, P.; Zhang, W.; Umeda, A.; Zhang, Z.J.; Chen, S. Femtosecond Laser-Assisted Optoporation for Drug and Gene Delivery into Single Mammalian Cells. J Biomed Nanotechnol 2011, 7, 334–341.

14. Kesharwani, P.; Jain, K.; Jain, N.K. Dendrimer as Nanocarrier for Drug Delivery. Prog Polym Sci 2014, 39, 268–307.

15. Gehl, J. Electroporation: Theory and Methods, Perspectives for Drug Delivery, Gene Therapy and Research. Acta Physiol Scand 2003, 177, 437–447.

16. Chakrabarty, P.; Gupta, P.; Illath, K.; Kar, S.; Nagai, M.; Tseng, F.G.; Santra, T.S. Microfluidic Mechanoporation for Cellular Delivery and Analysis. Mater Today Bio 2022, 13, 100193.

17. Kim, H.; Lee, M.; Han, B.; Kim, J.; Cho, D.; Doh, J.; Chung, A.J. Advancing Allogeneic NK Cell Immunotherapy through Microfluidic Gene Delivery. Adv Sci (Weinh) 2025,12, 2412544.

18. Zhang, G.; Gao, X.; Song, Y.K.; Vollmer, R.; Stolz, D.B.; Gasiorowski, J.Z.; Dean, D.A.; Liu, D. Hydroporation as the Mechanism of Hydrodynamic Delivery. Gene Ther 2004, 11, 675–682.

19. Sytsma, B.J.; Allain, V.; Bourke, S.; Faizee, F.; Fathi, M.; Ferreira, L.M.R.; Brewer, W.J.; Li, L.; Pan, F.L.; Rothrock, A.G.; et al. Scalable Intracellular Delivery via Microfluidic Vortex Shedding Enhances the Function of Chimeric Antigen Receptor T-Cells. Sci Rep 2025, 15, 5749.

20. Shinde, P.; Kar, S.; Loganathan, M.; Chang, H.Y.; Tseng, F.G.; Nagai, M.; Santra, T.S. Infrared Pulse Laser-Activated Highly Efficient Intracellular Delivery Using Titanium Microdish Device. ACS Biomater Sci Eng 2020, 6, 5645–5652.

21. Yao, C.P.; Zhang, Z.X.; Rahmanzadeh, R.; Huettmann, G. Laser-Based Gene Transfection and Gene Therapy. IEEE Trans Nanobioscience 2008, 7, 111–119.

22. Xiong, R.; Samal, S.K.; Demeester, J.; Skirtach, A.G.; De Smedt, S.C.; Braeckmans, K. Laser-Assisted Photoporation: Fundamentals, Technological Advances and Applications. Adv Phys X 2016, 1, 596–620.

23. Soman, P.; Zhang, W.; Umeda, A.; Zhang, Z.J.; Chen, S. Femtosecond Laser-Assisted Optoporation for Drug and Gene Delivery into Single Mammalian Cells. J Biomed Nanotechnol 2011, 7, 334–341.

24. Weiss, J.; Garnon, J.; Dalili, D.; Cazzato, R.L.; Koch, G.; Auloge, P.; Gangi, A. The Feasibility of Combined Microwave Ablation and Irreversible Electroporation for Central Liver Metastases. Cardiovasc Intervent Radiol 2021, 44, 999–1001.

25. Canatella, P.J.; Karr, J.F.; Petros, J.A.; Prausnitz, M.R. Quantitative Study of Electroporation-Mediated Molecular Uptake and Cell Viability. Biophys J 2001, 80, 755–764.

26. Liu, Y.; Yan, J.; Prausnitz, M.R. Can Ultrasound Enable Efficient Intracellular Uptake of Molecules? A Retrospective Literature Review and Analysis. Ultrasound Med Biol 2012, 38, 876–888.

27. Wang, J.; Harizaj, A.; Wu, Y.; Jiang, X.; Brans, T.; Fraire, J.C.; Mejía Morales, J.; De Smedt, S.C.; Tang, Z.; Xiong, R.; et al. Black Phosphorus Mediated Photoporation: A Broad Absorption Nanoplatform for Intracellular Delivery of Macromolecules. Nanoscale 2021, 13, 17049–17056.

28. Du, X.; Wang, J.; Zhou, Q.; Zhang, L.; Wang, S.; Zhang, Z.; Yao, C. Advanced Physical Techniques for Gene Delivery Based on Membrane Perforation. Drug Deliv 2018, 25, 1516–1525.

29. Ramon, J.; Xiong, R.; De Smedt, S.C.; Raemdonck, K.; Braeckmans, K. Vapor Nanobubble-Mediated Photoporation Constitutes a Versatile Intracellular Delivery Technology. Curr Opin Colloid Interface Sci 2021, 54, 1014453.

30. Becker, A.; Lehrich, T.; Kalies, S.; Heisterkamp, A.; Ngezahayo, A. Parameters for Optoperforation-Induced Killing of Cancer Cells Using Gold Nanoparticles Functionalized with the c-Terminal Fragment of Clostridium Perfringens Enterotoxin. Int J Mol Sci 2019, 20, 4248.

31. Heinemann, D.; Kalies, S.; Schomaker, M.; Ertmer, W.; Murua Escobar, H.; Meyer, H.; Ripken, T. Delivery of Proteins to Mammalian Cells via Gold Nanoparticle Mediated Laser Transfection. Nanotechnology 2014, 25(24), 254101.

32. Begandt, D.; Bader, A.; Antonopoulos, G.C.; Schomaker, M.; Kalies, S.; Meyer, H.; Ripken, T.; Ngezahayo, A. Gold Nanoparticle-Mediated (GNOME) Laser Perforation: A New Method for a High-Throughput Analysis of Gap Junction Intercellular Coupling. J Bioenerg Biomembr 2015, 47, 441–449.

33. Kalies, S.; Keil, S.; Sender, S.; Hammer, S.C.; Antonopoulos, G.C.; Schomaker, M.; Ripken, T.; Escobar, H.M.; Meyer, H.; Heinemann, D. Characterization of the Cellular Response Triggered by Gold Nanoparticle–Mediated Laser Manipulation. J Biomed Opt 2015, 20, 115005.

34. Schomaker, M.; Killian, D.; Willenbrock, S.; Heinemann, D.; Kalies, S.; Ngezahayo, A.; Nolte, I.; Ripken, T.; Junghanß, C.; Meyer, H.; et al. Biophysical Effects in Off-Resonant Gold Nanoparticle Mediated (GNOME) Laser Transfection of Cell Lines, Primary- and Stem Cells Using Fs Laser Pulses. J Biophotonics 2015, 8, 646–658.

35. Lapotko, D. Optical Excitation and Detection of Vapor Bubbles around Plasmonic Nanoparticles. Opt Express 2009, 17, 2538.

36. Eversole, D.; Subramanian, K.; Harrison, R.K.; Bourgeois, F.; Yuksel, A.; Ben-Yakar, A. Femtosecond Plasmonic Laser Nanosurgery (Fs-PLN) Mediated by Molecularly Targeted Gold Nanospheres at Ultra-Low Pulse Fluences. Sci Rep 2020, 10, 12387.

37. Mohan, L.; Kar, S.; Nagai, M.; Santra, T.S. Electrochemical Fabrication of TiO2 Micro-Flowers for an Efficient Intracellular Delivery Using Nanosecond Light Pulse. Mater Chem Phys 2021, 267, 124604.

38. Mohan, L.; Kar, S.; Ren Hattori; Ishii-Teshima, M.; Bera, P.; Roy, S.; Santra, T.S.; Shibata, T.; Nagai, M. Can Titanium Oxide Nanotubes Facilitate Intracellular Delivery by Laser-Assisted Photoporation? Appl Surf Sci 2021, 543, 148815.

39. Shinde, A.; Shinde, P.; Kar, S.; Illath, K.; Dey, S.; Mahapatra, N.R.; Nagai, M.; Santra, T.S. Metallic Micro-Ring Device for Highly Efficient Large Cargo Delivery in Mammalian Cells Using Infrared Light Pulses. Lab Chip 2023,23, 2175-2192.

40. Nakashima, Y.; Yamamoto, Y.; Hikichi, Y.; Nakanishi, Y. Creation of Cell Micropatterns Using a Newly Developed Gel Micromachining Technique. Biofabrication 2016, 8(3), 035006.

41. Deglincerti, A.; Etoc, F.; Guerra, M.C.; Martyn, I.; Metzger, J.; Ruzo, A.; Simunovic, M.; Yoney, A.; Brivanlou, A.H.; Siggia, E.; et al. Self-Organization of Human Embryonic Stem Cells on Micropatterns. Nat Protoc 2016, 11, 2223–2232.

42. Wu, Y.C.; Wu, T.H.; Clemens, D.L.; Lee, B.Y.; Wen, X.; Horwitz, M.A.; Teitell, M.A.; Chiou, P.Y. Massively Parallel Delivery of Large Cargo into Mammalian Cells with Light Pulses. Nat Methods 2015, 12, 439–444.

43. Venugopalan, V.; Guerra, A.; Nahen, K.; Vogel, A. Role of Laser-Induced Plasma Formation in Pulsed Cellular Microsurgery and Micromanipulation. Phys Rev Lett 2002, 88, 781031–781034.

44. Hellman, A.N.; Rau, K.R.; Yoon, H.H.; Venugopalan, V. Biophysical Response to Pulsed Laser Microbeam-Induced Cell Lysis and Molecular Delivery. J Biophotonics 2008, 1, 24–35.

45. Schroeder, M.C.; Andral, U.; Wolf, J.P. Opto-Mechanical Expulsion of Individual Micro-Particles by Laser-Induced Shockwave in Air. AIP Adv 2022, 12(9), 095119.

46. Noack, J.; Vogel, A. Single-Shot Spatially Resolved Characterization of Laser-Induced Shock Waves in Water; Appl Opt 1998, 37, 4092-4099.

47. Rau, K.R.; Quinto-Su, P.A.; Hellman, A.N.; Venugopalan, V. Pulsed Laser Microbeam-Induced Cell Lysis: Time-Resolved Imaging and Analysis of Hydrodynamic Effects. Biophys J 2006, 91, 317–329.

48. Bergeron, E.; Boutopoulos, C.; Martel, R.; Torres, A.; Rodriguez, C.; Niskanen, J.; Lebrun, J.-J.; Winnik, F.M.; Sapieha, P.; Meunier, M. Cell-Specific Optoporation with near-Infrared Ultrafast Laser and Functionalized Gold Nanoparticles. Nanoscale 2015, 7, 17836–17847.

49. Patskovsky, S.; Qi, M.; Meunier, M. Single Point Single-Cell Nanoparticle Mediated Pulsed Laser Optoporation. Analyst 2020, 145, 523–529.

50. Zhou, Y.; Yang, K.; Cui, J.; Ye, J.Y.; Deng, C.X. Controlled Permeation of Cell Membrane by Single Bubble Acoustic Cavitation. J Control Release. 2012, 157, 103–111.

51. Yasukuni, R.; Koyanagi, A.; Tanaka, Y.; Okano, K.; Hosokawa, Y. Cell Viability Assessment Associated with a Contact of Gas Bubbles Produced by Femtosecond Laser Breakdown in Cell Culture Media. Sci Rep 2022, 12, 19001.

52. Long, J.; Eliceiri, M.; Vangelatos, Z.; Rho, Y.; Wang, L.; Su, Z.; Xie, X.; Zhang, Y.; Grigoropoulos, C.P. Early Dynamics of Cavitation Bubbles Generated during NS Laser Ablation of Submerged Targets. Opt Express 2020, 28, 14300.

53. Gomez Godinez, V.; Morar, V.; Carmona, C.; Gu, Y.; Sung, K.; Shi, L.Z.; Wu, C.; Preece, D.; Berns, M.W. Laser-Induced Shockwave (LIS) to Study Neuronal Ca2+ Responses. Front Bioeng Biotechnol 2021, 9, 598896.

54. Qian, Y.; Neale, S.L.; Marsh, J.H. Microparticle Manipulation Using Laser-Induced Thermophoresis and Thermal Convection Flow. Sci Rep 2020, 10, 19169.

55. Davis, A.A.; Farrar, M.J.; Nishimura, N.; Jin, M.M.; Schaffer, C.B. Optoporation and Genetic Manipulation of Cells Using Femtosecond Laser Pulses. Biophys J 2013, 105, 862–871.

56. Waleed, M.; Hwang, S.-U.; Kim, J.-D.; Shabbir, I.; Shin, S.-M.; Lee, Y.-G. Single-Cell Optoporation and Transfection Using Femtosecond Laser and Optical Tweezers. Biomed Opt Express 2013, 4, 1533.

57. Soughayer, J.S.; Krasieva, T.; Jacobson, S.C.; Ramsey, J.M.; Tromberg, B.J.; Allbritton, N.L. Characterization of Cellular Optoporation with Distance. Anal Chem 2000, 72, 1342–1347.

Chapter 3: Parallelization of Micropatterned Cell Perforation: Investigating Cell Response to Pulsed Laser Irradiation on Micropatterned Surface

3.1 Introduction

The study of cellular responses to various physical stimuli is essential for advancing modern theranostic therapies, as it provides crucial insights into cell behavior and development under external influences. For instance, in cancer therapy and treatment, significant focus has been placed on methods that depend on cell responses to specific photothermal stimuli, such as photothermal therapy (PTT) [1–3] and optoporation-assisted cell reprogramming [4–7]. Based on the cell response, these techniques aim to develop targeted treatment for tumors while minimizing damage to the healthy cell population. Hence, the advancements in understanding cellular responses to physical stimuli can lead to the development of advanced technologies and therapeutic strategies that can significantly improve patient care and outcomes.

Cells exhibit diverse responses to applied physical stimuli such as mechanical forces, electric fields, ultrasound, and optical energy. In mechanotransduction, cells convert mechanical forces into biochemical signals, influencing critical processes such as differentiation, proliferation, and migration that play pivotal roles in cell development [8, 9]. Furthermore, some physical stimuli have immediate effects that lead to changes in the organization of the cell's cytoskeleton and may result in phenomena like increased membrane permeability. In the context of ultrasound-induced effects, cell membranes undergo deformation and transient pore creation, facilitating the entry of foreign molecules into the cells [10–12]. Similarly, electrical field stimuli such as electroporation can increase cell permeability or induce cell death [13, 14].

Biomedical processes that utilize laser-induced cell-membrane effects, such as cell perforation, cell necrosis, or cell fragmentation, have garnered significant attention for their versatile applications in various biomedical therapeutic fields, particularly in photothermal therapy [1–3, 15, 16] and

optoporation [17–23]. These effects, generated by the rapid absorption of laser energy by targeted materials, offer a unique combination of precision and minimal invasiveness, making them ideally suited for delicate biomedical procedures. One of the primary advantages of laser-induced cell effects is their ability to provide highly precise spatial control [16,24]. The laser's energy can be tightly focused on specific areas, allowing for targeted treatment of diseased or damaged tissues while minimizing the impact on surrounding healthy tissue. In photothermal therapy, lasers are used to selectively heat and destroy cancerous cells. By confining the shockwave to the target area, this approach effectively eliminates tumors while preserving the integrity of adjacent structures, reducing the risk of collateral damage and improving patient outcomes [25–33]. Similarly, in optoporation, lasers are employed to create transient pores in the cell membrane, enabling the delivery of therapeutic molecules directly into the cytosol [34–43]. Unlike other physical delivery methods, such as electroporation or microinjection, laser-induced optoporation achieves membrane permeabilization without causing significant damage to cells or tissues. Both photothermal therapy and optoporation rely on specific cellular responses to lasers—cell perforation in the case of optoporation and cell fragmentation in photothermal therapy.

The cell responses to lasers can be realized by using several techniques, each with its own set of advantages and limitations. Three primary methods include direct laser irradiation [4,44–46], nanoparticle sensitization [47–51], and a more recent approach—micropattern-assisted shockwave generation [43,52]. Direct laser irradiation is the most straightforward method, where a tightly focused laser beam is directed onto a specific point on the sample, resulting in rapid plasma formation. This plasma expands explosively, generating a shockwave that propagates through the medium. However, this method typically requires high laser fluences (energy per unit area) and extremely precise focusing of the laser beam, which can limit its practicality, especially in clinical settings where precision and safety are paramount. The high energy involved also increases the risk of damage to surrounding healthy tissues. To address these challenges, nanoparticle sensitization has been developed as an

alternative method. In this approach, nanoparticles are introduced into the target area. These particles are designed to absorb laser energy efficiently, converting it into localized heat, which in turn results in membrane permeabilization [53–56]. This method allows for the use of less focused laser beams and lower fluences, making the process more efficient and enabling parallel processing of multiple cells or areas simultaneously. This scalability makes nanoparticle sensitization a promising technique for large-scale applications. However, the introduction of nanoparticles comes with significant risks, particularly the potential for nanoparticle-associated cytotoxicity for non-target cell populations. Prolonged interactions between nanoparticles and non-target cells can lead to unintended cellular damage, which is a major concern in clinical contexts.

To overcome the limitations associated with both direct laser irradiation and nanoparticle sensitization, a novel approach known as micropattern-assisted laser methods has been developed. This technique leverages micro-patterned surfaces, which are engineered to interact with the laser in a highly controlled manner. When the laser beam strikes these micropatterns, the energy is distributed in a way that generates highly localized effects. This method is highly site-specific, meaning that the effects are confined to precise areas of interest, thereby minimizing the risk of damage to surrounding tissues [57, 58]. Because it does not rely on nanoparticles, this technique mitigates the risks of cytotoxicity, making it a safer option for clinical use. Micropattern-assisted method has been successfully employed in optoporation to temporarily permeabilize cell membranes to allow the delivery of molecules such as drugs or genetic material into cells. Despite the successful use of this technique in optoporation, the interaction of the laser with the micropatterns and the broader biological responses of cells to micropattern-generated laser effects, particularly from the point of view of cell heterogeneity, have not been thoroughly studied. This cell heterogeneity in the cell population can lead to diverse responses, complicating the task of optimizing laser parameters for consistent outcomes.

In this study, we worked towards the parallelization of the method developed in Chapter 2 with a relatively different approach of using a micropattern on top configuration. We first characterized the

laser irradiation on micropatternd surface and then we focused on the biological responses of HeLa cells—a widely used human cell line in research—to micropattern-generated bio-effects. Specifically, we examine two critical responses: cell perforation (resealable pores for intracellular delivery) and cell fragmentation (cell peeling and cell necrosis). Cell perforation refers to the creation of temporary pores in the cell membrane, which can facilitate the entry of therapeutic agents. Understanding the factors that influence the efficiency and safety of perforation is essential for optimizing therapies like optoporation. On the other hand, cell fragmentation, where the shockwave causes the cell to break apart, can be either a desired outcome (as in certain cancer treatments) or an adverse effect that needs to be minimized, which can be critical in the evaluation of modern photothermal therapies. By systematically studying these cellular behaviors, we aim to refine the parameters of micropattern-assisted cell effects to achieve optimal therapeutic outcomes.

3.2 Experimental Methods

3.2.1 Fabrication of Optical Absorber Disks

A mixture of 0.45 g of red pigment PR-254 (P1676, Tokyo Kasei, Japan) was prepared in 15 mL of cyclopentanone in a centrifuge tube. This solution was then combined with 15 mL of SU-8 3005 (KAYAKU Advanced Materials, USA) to achieve a 1.5 w/v% concentration of PR-254. The SU-8-PR-254 mixture was stirred for 20 minutes using a vortex mixer (TRIO HM-2F, AZ-ONE, Japan).

The prepared solution was spin-coated onto a 4-inch glass wafer, and circular patterns with diameters of 20 μm and varying pitches of 30 μm, 35 μm, and 45 μm were formed through photolithography. Before coating, the glass wafer was cleaned with acetone, rinsed with isopropanol (IPA), dried with nitrogen gas, and plasma-treated at 150 W for 60 seconds to enhance hydrophilicity (JPA-300, J-Science Labs, Japan).

Hexamethyldisiloxane (HMDS) was spin-coated onto the plasma-treated substrate with the following spin cycle: initial slope for 5 seconds, 1000 rpm for 10 seconds, slope for 5 seconds, 5000

rpm for 30 seconds, and slope for 10 seconds, followed by baking. The SU-8/PR-254 suspension was then spin-coated onto the HMDS layer with a spin sequence of slope for 5 seconds, 500 rpm for 20 seconds, slope for 5 seconds, and 3000 rpm for 60 seconds, ending with a final slope for 10 seconds.

After baking, the coated wafer was exposed to a 600 mJ/cm² light integral using a mask aligner (PEM-800, Union Optical). Post-exposure baking was performed, and the wafer was developed using 2-methoxy-1-methylethyl acetate (Figure 3.1). Following development, the wafer was diced into smaller chips, and the edges were pasted with 10 µm-thick tape to avoid the direct contact of the micropattern chip and cells.

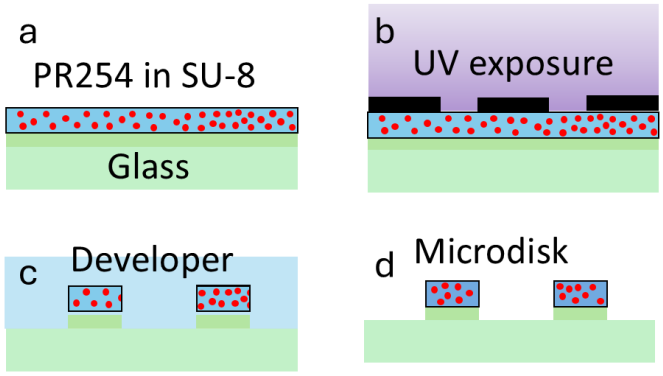

Figure 3.1 (a)-(d) Steps in the fabrication of microdisk pattern.

3.2.2 Irradiation Setup

A custom setup was built to irradiate cells at the specific location of the petri dish. A nanosecond pulsed laser (Cobolt, Tor^{TM} XS, Hubner Photonics, Solna, Sweden) with a pulse width of 5 ns and repetition rate of 1kHz was connected to a function generator. A dichroic mirror (Thorlabs, DMLP550R, Newton, NJ, USA) was used to reflect a 532 nm light beam, and the beam was focused on the sample with a convex lens of focal length 50 mm to a beam waist of around 30 µm. While laser irradiation, the samples were observed with a CMOS camera (ZWO, ASL1600MC-Cool, Suzhou, China).

3.2.3 Analysis of Laser Irradiation on Micropattern Surface

The cavitation bubbles were generated by irradiating the micropatterns with a nanosecond pulsed laser at different laser fluences and imaged using a CMOS camera (ZWO, ASL1600MC-Cool, Suzhou, China) equipped with the irradiation setup. These images were analysed in ImageJ (Fiji) to obtain the bubble diameter and number of bubbles for specific experimental conditions.

3.2.4 Cell Culture

HeLa cells were cultured in minimum essential medium (MEM, Gibco, 11095072, Thermo Fisher Scientific, Waltham, MA, USA) supplemented with 10% fetal bovine serum (FBS, CCP-FBS-BR-500, Cosmo Bio, Tokyo, Japan) and 1% penicillin-streptomycin (streptomycin 10,000 U/mL, Thermo Fisher Scientific, Waltham, MA, USA) in 37^{o}C in a 5% CO2 humidified atmosphere.

3.2.5 Laser Irradiation Experiment, Image Acquisition, and Analysis

The micropattern device was cleaned with 70% ethanol and dried in UV for 2 hours before the experiment. The cultured cells at appropriate confluency were washed thrice with PBS, and fresh medium containing FITC Dextran (4 mg/mL) of interest was added to the petri dish. Then the inverted device was placed on the petri dish with cells and FITC Dextran, and it was placed over the stage. The stage was moved at a constant velocity of 1mm/s with micropatterns of various pitches and laser fluence of 25mJ/cm^2, 66 mJ/cm^2, and 100 mJ/cm^2. Upon completion of laser scanning. The device was taken out, and cells were immediately washed with PBS three times to observe the immediate effect of laser shockwave application. Then, fresh medium was added, and PI (4 μM) was added to the fresh medium to observe cell necrosis.

Brightfield and FITC-positive and PI-stained images were obtained using a Nikon Ti-2 microscope to evaluate cell responses in the irradiated regions. First, the average cell density in the non-irradiated control region *($N_{Control}$)* was calculated by averaging five images for each experimental condition. For the irradiated regions, an image set of brightfield microscopy ($N_{Brightfield}$), the number of

FITC-positive cells (N_{FITC}), and the number of necrotic cells (N_{PI}) were analyzed to evaluate cell perforation and cell fragmentation.

The efficiency of cell perforation (η_P) for each image set was calculated by taking the ratio of FITC-positive cells from the FITC image to the average number of cells in the control region, and the data was represented as an average of five image sets as represented in Eq. 3.1:

$$\eta_P = \frac{N_{FITC}}{N_{Control}} \quad \ldots (3.1)$$

Cell fragmentation (η_F) for each set of images was determined by calculating the difference between the average control cell number ($N_{Control}$) and the total number of cells in the irradiated region to account for cells that peeled off ($N_{peeled\ off}$) due to irradiation. This number was then combined with the number of necrotic cells (N_{PI}) from PI-stained cells, and the sum was expressed as a ratio relative to the control cell number as represented in Eq. 3.2 and Eq. 3.3:

$$\eta_F = \frac{N_{Peeled\ off} + N_{PI}}{N_{Control}} \quad \ldots (3.2)$$

$$\eta_F = \frac{(N_{Control} - N_{Brightfield}) + N_{PI}}{N_{Control}} \quad \ldots (3.3)$$

The rest of the cells were classified as cells without any bioeffect.

3.3 Results

3.3.1 Characterization of Micropatterns

The photoabsorber micropatterns with pitches of 30 µm, 35 µm, and 45 µm were created by patterning PR-254 suspended in SU-8 using photolithography on a glass wafer, as shown in Figure 3.2(a)-(c). The intended diameter of the micropatterns was 20 µm, but after fabrication, the measured diameters were 25.5±0.1 µm, 25.9±0.6 µm, and 27.06±0.5 µm for the respective patterns (n=500 micropatterns) (Figure 2(d)). This resulted in distances between the micropatterns of 4.4±0.1 µm, 9.08±0.6 µm, and 17.9±0.4 µm for the pitches of 30 µm, 35 µm, and 45 µm (n=500 micropatterns) (Figure 3.2(e)). The deviation from the design dimensions is attributed to the limited resolution of the film mask, which hindered the accurate transfer of the corners.

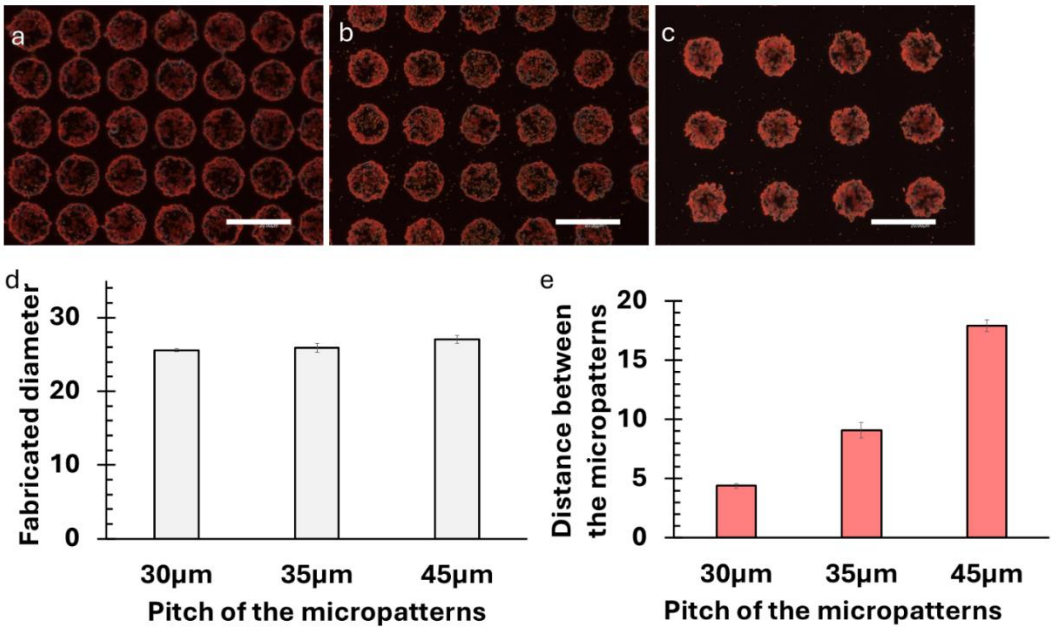

Figure 3.2 Fabricated micropatterns. (a)-(c) Pitch 30 µm, 35 µm, and 45 µm microdisks. (d) Fabricated radii of micropatterns. (e) Actual distance between adjacent micropatterns. Scale bar is 40 µm.

3.3.2 Characterization of Micropatterns and Laser Irradiation Interaction

We first investigated the irradiation of a single micropattern with a single pulse of 5ns laser irradiation at laser fluence of 25 mJ/cm^2, 66 mJ/cm^2, 100 mJ/cm^2 (Figure 3.3(a)). The images in the Figure. 3.3(b) clearly shows an increase in size of cavitation bubble formed upon laser irradiation of the micropattern with a single pulse of laser, indicating that the interaction between the micropattern and the laser pulse increases as the pulse energy is increased.

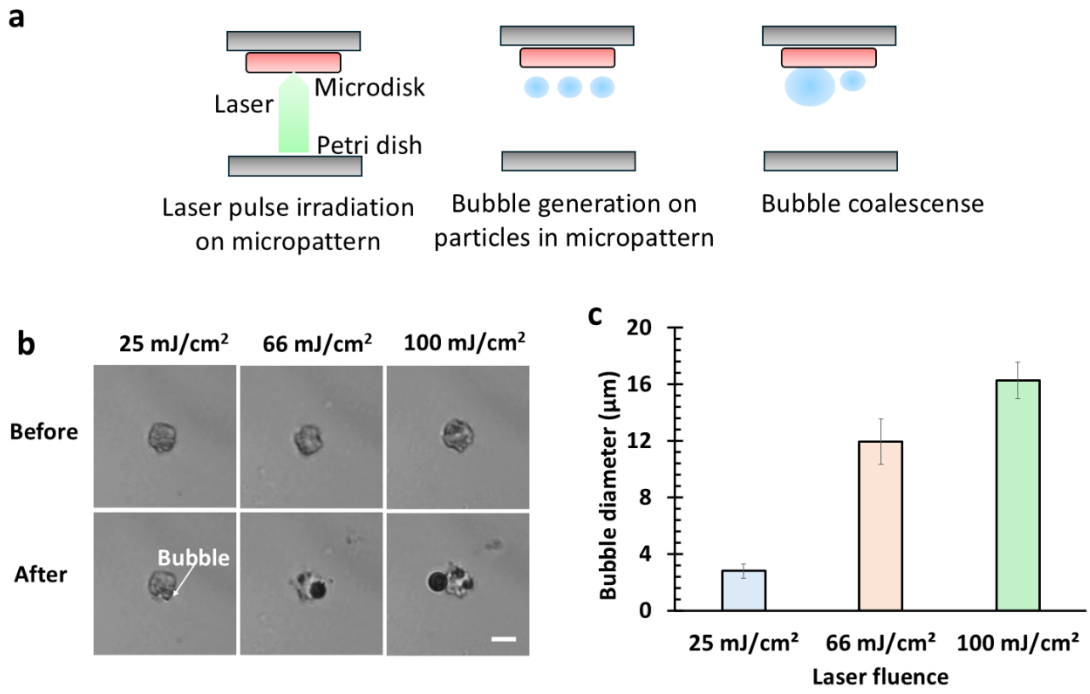

Figure 3.3 Single pulse laser irradiation on micropattern. (a) Pulse laser irradiation of micropattern. (b) Images of micropattern before and after pulse laser irradiation. Scale bar is 20 μm. (c) Size of cavitation bubble formed after pulse laser irradiation on the micropattern.

Next, we investigated the formation of microbubbles upon laser irradiation with a scanning laser with the same laser fluences and a micropatterned surface with various pitches to investigate the effect of micropattern pitch on the interaction of laser and micropattern (Figure 3.4(a)). Figure 3.4(b) represents site-specific irradiation of a 30 μm micropattern surface. Figures 3.4(c) show the generation of cavitation bubbles with increasing micropattern

pitch at the laser fluence of 66mJ/cm^2. The frequency of laser irradiation and micropattern interaction can be qualitatively described by studying the bubble density in the given area upon laser irradiation. Micropatterns with smaller pitches exhibit a higher bubble density, implying that more frequent cavitation events occur within a given area compared to micropatterns with larger pitches, suggesting more frequent generation of laser-assisted bio effects. This suggests that the smaller pitch micropatterns experience more frequent laser-induced effects, leading to increased laser-micropattern interaction activity. The graph in Figure 3.4(d) provides a clear representation of this relationship, showing that bubble generation is significantly more frequent in micropatterns with smaller pitches, while it is less frequent in patterns with larger pitches.

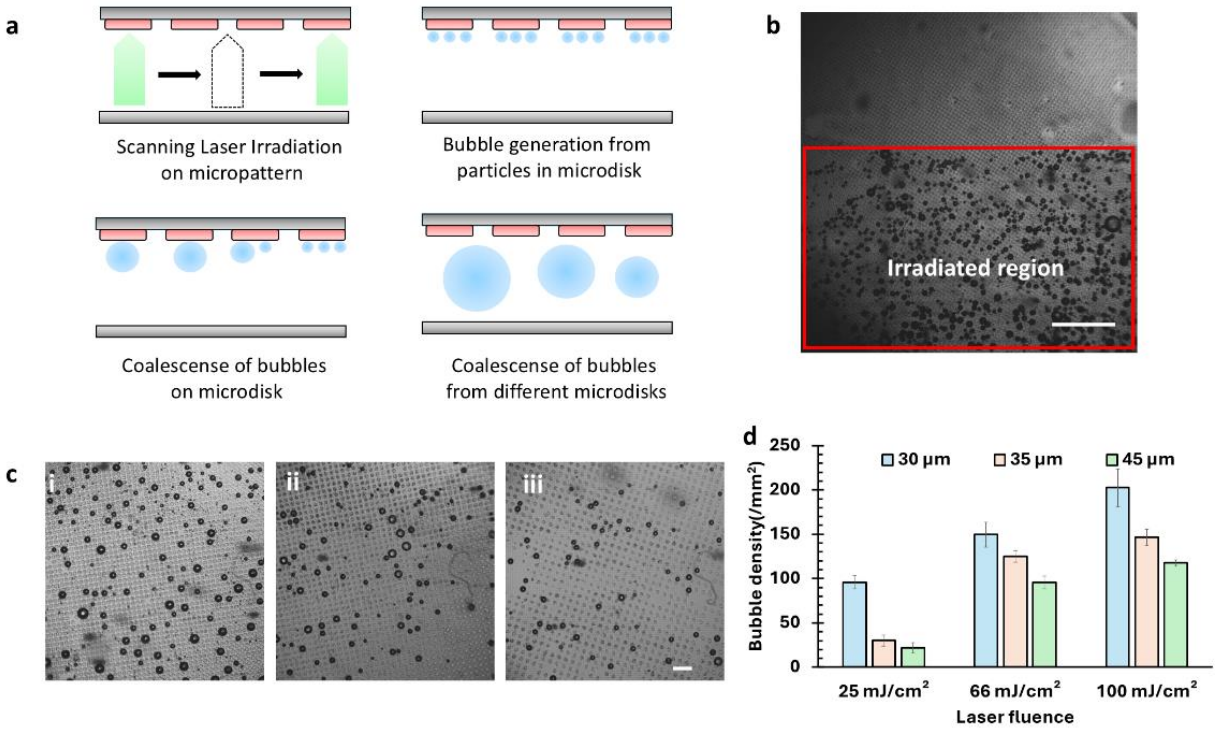

Figure 3.4 (a) Schematic representation of laser irradiation with scanning stage on the micropattern substrate. (b) Site-specific irradiation of 30 µm pitch micropattern. Scale bar is 300 µm. (c) Bubble generation at laser fluence of (i) 25 mJ/cm², (ii) 66 mJ/cm², (iii) 100 mJ/cm². Scale bar is 100 µm. (d) Bubble density at various pitches and fluences.

3.3.3 The Effect of Micropattern Pitch on Cell Response

We investigated the response of HeLa cells by adjusting the micropattern pitch and laser fluence as represented in Figure 3.5. Figure 3.5 (a)-(i) represents brightfield and fluorescent images of HeLa cells upon laser irradiation of a 35 μm micropattern. Figure 3.5(j) represents site-specific cell perforation in HeLa cells with a laser fluence of 66 mJ/cm^2. Increasing laser fluence for each pattern led to a reduction in the number of cells without inducing bioeffects such as cell perforation, necrosis, or fragmentation, as long as the micropattern pitch remained constant. Initially, increasing laser fluence increased cell perforation, after which cell fragmentation became the dominant effect. Additionally, for the same laser fluence, micropatterns with smaller pitches exhibited more pronounced bioeffects compared to those with larger pitches (Figure 3.5(k-m)) due to the presence of more localized effects. Control experiments with only laser irradiation on cells and laser irradiation on glass substrate without micropattern indicated that most of the cells were without bioeffects, indicating the necessity of both laser irradiation and micropattern for observed bioeffects in cells.

For the micropattern with a 30 μm pitch, a laser fluence of 25 mJ/cm² resulted in 10.5±0.7% cell perforation and 18.7±12.7% cell fragmentation. At 66 mJ/cm², cell perforation increased to 34.5±2.1% and cell fragmentation increased to 55.5±3.2%. Further increment in laser fluence to 100 mJ/cm^2 resulted in a decrease in cell perforation and an increase in cell fragmentation. Indicating that cell perforation can be maximized between 25 mJ/cm² to 66 mJ/cm², while between 66 and 100 mJ/cm², cell fragmentation dominated, indicating this fluence range may be ideal for applications requiring cell fragmentation.

Figures 5(a) to 5(i) illustrate cells after laser shockwave treatment with the 35 μm micropattern. A similar trend was observed as with the 30 μm pattern. For the 35 μm pitch, cell perforation increased from 16.9±9.4% to a higher perforation of 62.5±2.5%, while cell fragmentation was not statistically significant for increasing laser fluence from 25 mJ/cm^2 to

66 mJ/cm^2. These results suggest that the highest perforation occurs between 25-66 mJ/cm², but further increases in fluence to 100 mJ/cm² lead to high fragmentation (52.8±4.7%) and a decrease in cell perforation to 30.6±6.15%, making this fluence range suitable for cell fragmentation applications.

In case of micropatterns with 45 μm pitch, minimal effect on cells was observed at 25 mJ/cm², as more than 90% of cells remained unaffected. At 66 mJ/cm², cell fragmentation increases sharply to 19.0±3.1%, and delivery efficiency peaks at 30.8±7.8%, although only 50.11±6.8% of cells remain unaffected. Finally, at 100 mJ/cm², fragmentation reaches 47.1± 5.0%, while delivery drops to 18.23±2.8%, and just 34.5±5.1% of cells show no effect. These results indicate that at lower fluences (25-66 mJ/cm²), cell perforation (delivery) is maximized with minimal cell damage, while at higher fluences (66–100 mJ/cm²), cell fragmentation becomes dominant, reducing the delivery efficiency and increasing fragmentation becomes the most dominant at 47.19%, while delivery efficiency drops to 18.23%. Only 34.56% of cells show no effect at this higher energy level. In the case of micropatterns with a higher pitch, the cells with no effect are very high in comparison to micropatterns with a lower pitch due to a less localized effect caused by the micropattern with a higher pitch.

There is a clear trade-off between cell perforation and fragmentation, where higher laser fluences favor cell destruction (fragmentation) while lower fluences favor delivery (cell perforation). This balance allows for tuning the laser parameters based on the desired biological outcome—either for cellular disruption or efficient molecular delivery. In summary, for effective molecular delivery with minimal cell damage, lower laser fluences (25-66 mJ/cm²) and smaller micropattern pitches (30–35 μm) are preferred. On the other hand, for inducing cell fragmentation, higher laser fluences (above 100 mJ/cm²) are more effective, particularly with smaller micropatterns. The ability to modulate bioeffects through these parameters offers flexibility in tailoring the treatment for specific applications.

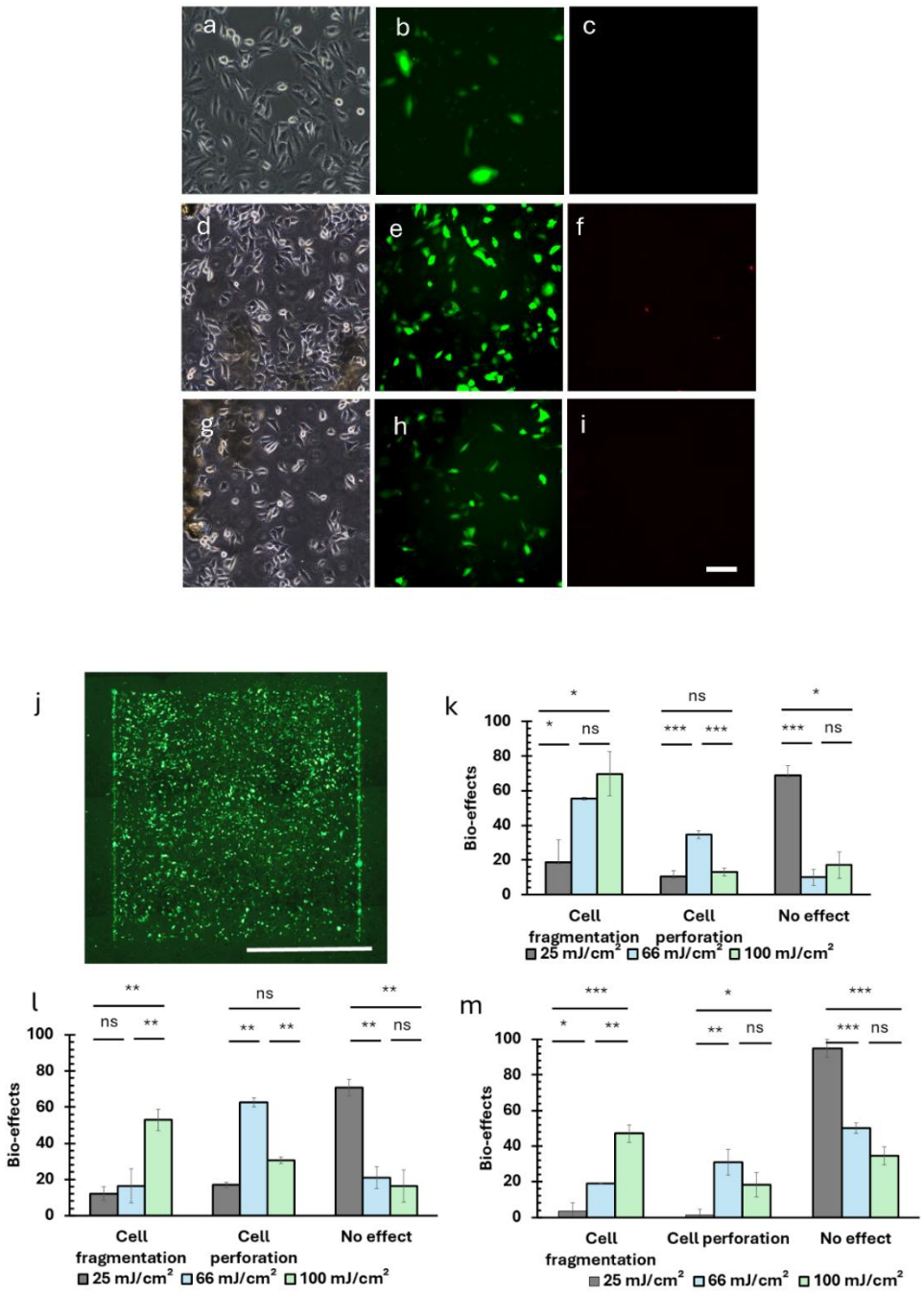

Figure 3.5 Analysis of bioeffects on HeLa cells upon laser irradiation on micropatterned surface. (a)-(i) Brighfield, FITC introduced and PI stained images for 35 µm micropattern. (a)-(c) 25mJ/cm². (d)-(f) 66mJ/cm². (g)-(i) 100mJ/cm². Scale bar is 100 µm. (j) Tile-scan image of irradiation of HeLa cells with 35 µm micropattern at 66 mJ/cm². Scale bar is 2.5 mm. Laser-assisted bio effects on HeLa cells for micropatterns with pitch. (k) 30µm, (l) 35µm, and (m) 45 µm (One-way ANOVA: *p<0.05, **p<0.01, ***p<0.001).

3.3.4 The Effect of the Size of Cargo Molecules on the Cell Response

We investigated whether changing the size of a foreign molecule would have an effect on the biological response of the cells by changing the size of the dextran molecule to 10 kDa and 40 kDa. The micropattern with pitch 35 μm at laser fluence of 66 mJ/cm² was used to study the effect of the size of the foreign molecule on the bio effects. The figure represents the biological response of HeLa cells upon treatment with laser shockwaves. In case of FITC 10 kDa and 40 kDa, at the same treatment, the unaffected cells were 24.4±4.5% and 46.6±1.4% with cell perforation of 53.1±6.6% and 33.7±2.9% cells, respectively. The perforation in cells was seen to be less than that of 4 kDa, where 62.5±2.5% cells showed cell perforation. The decrement in perforation and increment in unaffected cells with consistent cell fragmentation prove the crucial role of cargo molecules in the experiment (Figure 3.6).

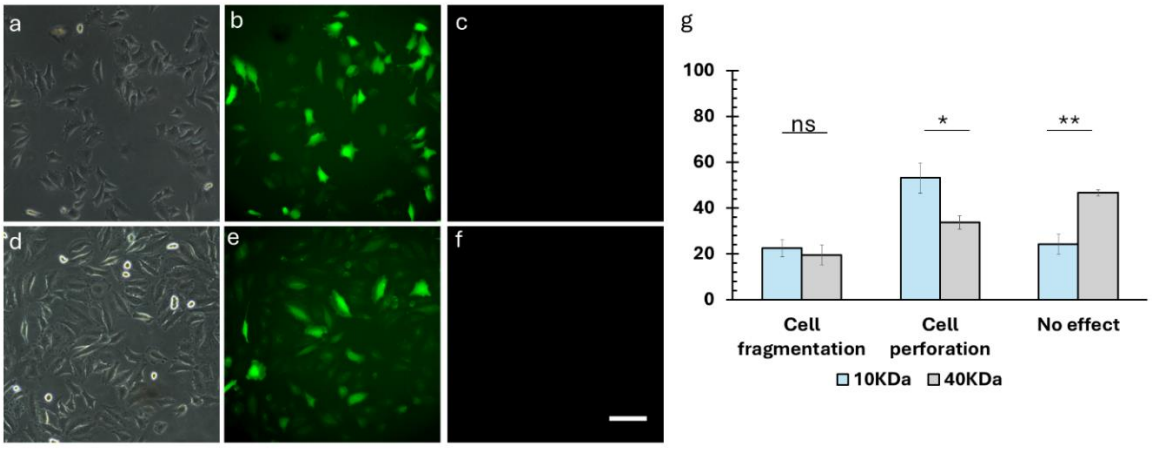

Figure 3.6 Delivery of higher molecular weight FITC Dextran into HeLa cells. (a)-(c) Brightfield, FITC 10 kDa introduced and PI-stained image of HeLa cells at 66 mJ/cm². (d)-(f) Brightfield, FITC 40 kDa introduced and PI-stained image of HeLa cells at 66 mJ/cm². Scale bar is 100 μm. (g) Bio-effects in HeLa cells with FITC 10kDa and 40kDa (Students *t*-test: $*p<0.05$, $**p<0.01$, $***p<0.001$).

These results might be due to differences in diffusion rates of the molecules, as larger molecules tend to diffuse slowly into the cell cytosol. We assume that at given parameters of laser and micropattern, the perforation mechanism remains the same, and cells' pores are supposed to be of the same size.

3.4 Discussion

3.4.1 Mechanism of Bio-effect Induction in Cells

The interaction between laser irradiation and micropatterns in cell culture medium results in material modification and induces laser effects. Although direct observation of plasma light emission was not feasible with our current setup, likely, laser-induced breakdown or localized plasma generation at the interface of the microdisk and cell medium plays a critical role in these laser-induced bio effects. When the laser energy surpasses a specific nucleation threshold, it increases the temperature at the micropattern interface, leading to nucleation and the formation of cavitation bubbles within the irradiated region. Each particle in the micropattern contributes to the formation of the nanobubbles, which coalesce and form a bigger microbubble. In the absence of observable plasma light emission, the appearance of bubbles can serve as a practical threshold for significant material modification.

The following mechanisms can be hypothesized for a potential working principle for observed bio effects on the cells upon nanosecond pulsed laser irradiation on the micropatterned substrate (Figure 3.7): (a) Bubble expansion and collapse, (b) Laser-induced shockwave, (c) Heat transfer from micropattern to cells, (d) Hydrodynamic effects. Upon laser irradiation on the micropattern surface. (a) The photoabsorber micropattern surface absorbs the laser energy rapidly and heats up, causing nucleation of cavitation bubbles. The expansion of these bubbles causes a shockwave in cell culture medium, causing shear stress on the cell membrane and causing transient pores or cell peeling from the substrate. (b) Alternatively, on

a faster timescale upon laser irradiation on the micropattern surface, a laser-induced shockwave is generated, which can cause the observed bio-effects. (c) The increment in temperature of the micropatterns might result in heat transfer to the cell membrane, causing permeabilization in the cell membrane by denaturation of the lipid bilayer of the cell membrane. (d) Laser-induced fluid flow from the micropatterns to the cells could create hydrodynamic forces that mechanically stress the cell membrane. These fluid flows may induce deformation or even pore formation in the cell membrane. Additionally, if the flow intensity exceeds the cell's ability to withstand mechanical stress, it may lead to cell detachment or peeling from the substrate. The flow could also facilitate the entry of substances into the cells, further contributing to the observed effects.

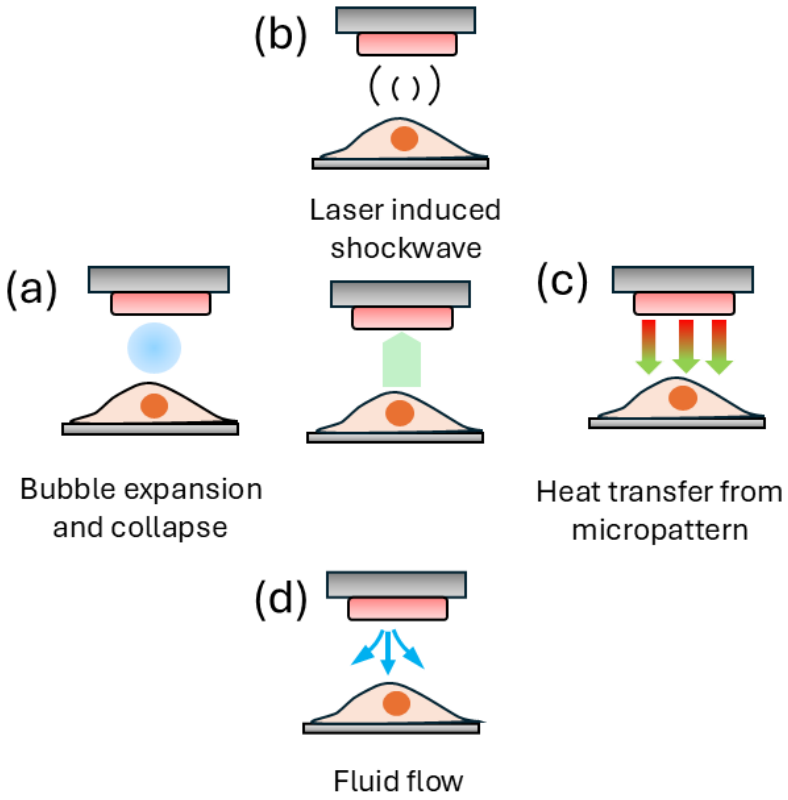

Figure 3.7 Schematic representation of a possible mechanism for observed bio-effects on cells (a) Bubble-induced bio-effect. (b) Laser-induced shockwave. (c) Heat transfer from micropattern to cells. (d) Hydrodynamic effects for bio-effects.

3.4.2 Implications for Biomedical Applications

This study investigates the response of mammalian cells to bioeffects generated in cells, which is paramount in a plethora of biomedical applications, such as intracellular delivery and photothermal therapy for determining optimal process parameters. These findings underscore the importance of both laser fluence and micropattern pitch in controlling the cell response and help us isolate the specific cell response at specific process parameters. The findings of this study conclude that the optimal fluence range is crucial for maximizing delivery efficiency while maintaining cell viability, particularly for therapeutic applications requiring minimal cell disruption.

The cell response changes to cell fragmentation from cell perforation at higher laser fluence. When the fluence exceeds the cell's capacity to repair or withstand the induced damage, the membrane integrity is permanently compromised, leading to cell rupture and fragmentation. However, in applications that require the destruction of cells, such as photothermal therapy, the same parameters can prove to be optimal because this method describes highly site-specific fragmentation of cells, which is crucial for non-invasive photothermal laser therapy, where differences in cell density are evident in irradiated and non-irradiated regions, indicating the spatial selectivity of the process.

3.4.3 Effect of Biomolecule Size

We studied the effect of biomolecule size on cell perforation and found that cell perforation tends to decrease for molecules as the size increases. The decrease in perforation with larger dextran molecules can be explained by the slower diffusion rates and increased resistance these molecules face when attempting to pass through the transient pores formed during laser treatment, which can be explained by the following formulae by assuming the FITC molecules to be spheres of Stokes radius r_s:

$$r_s = \frac{k_B T}{6\pi\eta D} \quad \ldots(3.4)$$

From the above formulae and value of Stokes radii for FITC 4 kDa (1.2nm), 10 kDa (2.3nm), and 40 kDa (4.5nm), the diffusion constant can be calculated at 25 °C to be 1.5×10^{-10} m^2/s, 9.55×10^{-11} m^2/s, and 4.88×10^{-11m} m^2/s [59]. Larger molecules have a lower diffusion constant; hence, they tend to enter cells slowly in cells and some of the small pores may close early enough to not let the larger molecules enter, while permitting entry of smaller molecules. Larger molecules like FITC Dextran 40 kDa may not have sufficient time to cross the cell membrane before the pores close, resulting in a lower number of porated cells. In addition, larger molecules may induce faster pore closure due to greater disruption of the cell membrane, which could further reduce the opportunity for these molecules to enter the cells.

While the current study highlights the size-dependent effects on cell response via laser shockwaves, several areas remain for further exploration. The particular response of the cells at a given laser fluence can potentially be maximized by fine-tuning the size and pitch of the micropatterns, which opens up the possibility of further research in the area.

3.4.4 Comparison to Previous Studies

The main advantage of our method lies in its fully contactless laser irradiation, where membrane pores are created not by direct heat transfer from nanoparticles to cells but through shockwaves generated by laser irradiation on a photoabsorber substrate. Unlike previous approaches that rely on nanoparticle-mediated heating or micropattern-mediated heating, our micropattern platform integrates multiple nanosecond laser pulses with a scanning stage, allowing large-area, parallel processing of cells. This design produces localized cavitation and shockwaves that permeabilize cell membranes efficiently, without physical contact or the use of nanoparticles. Moreover, our work is the first to simultaneously quantify both cell

perforation and cell fragmentation, offering a comprehensive characterization of bioeffects. This dual quantification enables precise tuning of laser parameters to maximize delivery efficiency while minimizing unwanted cell loss, advancing the development of tunable and scalable cell membrane perforation technologies. A concise comparison of this work can be found in Table 3.1 below.

Table 3.1 Comparison with previous studies.

Technique	**Photoabsorber / Approach**	**Application focus**	**Delivery evaluation method/ Efficiency**	**Unique Contribution**	**Reference**
Incubated nanoparticles based on optoporation	Light pulses directly on particles in incubated cells	Parallel delivery of large cargo	Qualitative and quantitative using a random field of view and flow cytometry	Highly localized delivery of cargo molecules into cells without accounting for cell loss	[37,38,50]
Massively parallel light-pulse delivery	Light pulses directly on mammalian cells (no substrate)	Parallel delivery of large cargo	Random selection of the field of view/ High efficiency Moderate delivery; limited site-specific control	Massively parallel delivery using light pulses	[41]
Infrared laser irradiation on the substrate	Titanium-based photoabsorber (nanotubes and micropatterns)	Entrance of a variety of molecules in cell lines without quantification of cell loss.	Random selection of the field of view/ High efficiency (more than 90%)	Quantitative pore resealing dynamics and delayed translocation mechanism	[42,43, 48]
Micropattern-assisted optoporation	PR-254 pigment micropatterns on SU-8 microdisks	Massively parallel optoporation quantifies both perforation and fragmentation	Random selection of the field of view/ moderate delivery efficiency (around 60%)	Contactless, avoiding nanoparticles, and enabling spatial control	Our work

3.5 Conclusions

Laser-irradiated micropatterned substrates for parallel pore creation in cell membrane offer a highly site-specific alternative to traditional direct laser and photosensitized methods. This study found that by systematically optimizing laser fluence and micropattern pitch for a desired application, the specific cell response can be isolated. Specifically, we found out that

HeLa cell responses to laser irradiation of micropatterns depend on micropattern pitches and the size of foreign molecules. For a micro-pattern surface with a specific pitch the increasing the laser fluence results in increasing cell perforation up to a certain limit, followed by fragmentation of the cells. For the chosen specific process parameters cell perforation of FITC-Dextran (4 kDa) was higher than the cell perforation of FITC 10 kDa and 40 kDa.

References

1. Huang, X.; Jain, P.K.; El-Sayed, I.H.; El-Sayed, M.A. Plasmonic Photothermal Therapy (PPTT) Using Gold Nanoparticles. Lasers Med Sci 2008, 23, 217–228.
2. Yang, K.; Zhao, S.; Li, B.; Wang, B.; Lan, M.; Song, X. Low Temperature Photothermal Therapy: Advances and Perspectives. Coord Chem Rev 2022, 454, 214330.
3. Zhao, L.; Zhang, X.; Wang, X.; Guan, X.; Zhang, W.; Ma, J. Recent Advances in Selective Photothermal Therapy of Tumor. J Nanobiotechnology 2021, 19, 335.
4. Campargue, G.; Zielinski, B.; Courvoisier, S.; Sarpe, C.; Winkler, T.; Bonacina, L.; Baumert, T.; Wolf, J.P. Live Cells Assessment of Opto-Poration by a Single Femtosecond Temporal Airy Laser Pulse. AIP Adv 2018, 8, 125105.
5. Becker, A.; Lehrich, T.; Kalies, S.; Heisterkamp, A.; Ngezahayo, A. Parameters for Optoperforation-Induced Killing of Cancer Cells Using Gold Nanoparticles Functionalized with the c-Terminal Fragment of Clostridium Perfringens Enterotoxin. Int J Mol Sci 2019, 20(17), 4248.
6. Du, X.; Fu, L.; Wang, Z.; Zhang, Z.; Jiang, S.; Wang, J.; Yao, C. Monitoring Optoporated Process on Mammalian Cells by Real-Time Measurement of Membrane Resealing Time. J Biomed Opt 2023, 28(6), 065006.
7. Pylaev, T.; Vanzha, E.; Avdeeva, E.; Khlebtsov, B.; Khlebtsov, N. A Novel Cell Transfection Platform Based on Laser Optoporation Mediated by Au Nanostar Layers. J Biophotonics 2019, 12(1), e201800166.
8. Martino, F.; Perestrelo, A.R.; Vinarský, V.; Pagliari, S.; Forte, G. Cellular Mechanotransduction: From Tension to Function. Front Physiol 2018, 9, 824.
9. Mousavi, S.J.; Hamdy Doweidar, M. Role of Mechanical Cues in Cell Differentiation and Proliferation: A 3D Numerical Model. PLoS One 2015, 10(5), 0124529.
10. Porret, E.; Hoang, S.; Denis, C.; Doris, E.; Hrubý, M.; Novell, A.; Gravel, E.; Truillet, C. Sonoporation-Assisted Micelle Delivery in Subcutaneous Glioma-Bearing Mice Evaluated by PET/Fluorescent Bi-Modal Imaging. Nanoscale 2023, 15, 12574-12585.
11. Liang, H.D.; Tang, J.; Halliwell, M. Sonoporation, Drug Delivery, and Gene Therapy. Proc Inst Mech Eng H 2010, 224, 343–361.
12. Chen, Q.; Huang, J.; Ye, Y.; Hu, A.; Xu, B.; Hu, D.; Wang, L.; Xing, L.; Chen, S.; Gui, X.; et al. Delivery of Hydroxycamptothecin via Sonoporation: An Effective Therapy for Liver Fibrosis. J Control Release 2023, 358, 319–332.

13. Canatella, P.J.; Karr, J.F.; Petros, J.A.; Prausnitz, M.R. Quantitative Study of Electroporation-Mediated Molecular Uptake and Cell Viability; 2001, 80(2), 755-64.

14. Gehl, J. Electroporation: Theory and Methods, Perspectives for Drug Delivery, Gene Therapy and Research. Acta Physiol Scand 2003, 177, 437–447.

15. Li, J.; Liu, X.; Tan, L.; Cui, Z.; Yang, X.; Liang, Y.; Li, Z.; Zhu, S.; Zheng, Y.; Yeung, K.W.K.; et al. Zinc-Doped Prussian Blue Enhances Photothermal Clearance of Staphylococcus Aureus and Promotes Tissue Repair in Infected Wounds. Nat Commun 2019, 10(1), 4490.

16. Mishra, A.; Inaam, R.; Okamoto, S.; Shibata, T.; Santra, T.S.; Nagai, M. Visible Pulsed Laser-Assisted Selective Killing of Cancer Cells with PVP-Capped Plasmonic Gold Nanostars. Micromachines (Basel) 2023, 14(6), 1173.

17. Berdecka, D.; Harizaj, A.; Goemaere, I.; Punj, D.; Goetgeluk, G.; De Munter, S.; De Keersmaecker, H.; Boterberg, V.; Dubruel, P.; Vandekerckhove, B.; et al. Delivery of Macromolecules in Unstimulated T Cells by Photoporation with Polydopamine Nanoparticles. J Control Release 2023, 354, 680–693.

18. Breunig, H.G.; Uchugonova, A.; Batista, A.; König, K. Software-Aided Automatic Laser Optoporation and Transfection of Cells. Sci Rep 2015, 5, 11185.

19. Davis, A.A.; Farrar, M.J.; Nishimura, N.; Jin, M.M.; Schaffer, C.B. Optoporation and Genetic Manipulation of Cells Using Femtosecond Laser Pulses. Biophys J 2013, 105, 862–871.

20. Wang, J.; Harizaj, A.; Wu, Y.; Jiang, X.; Brans, T.; Fraire, J.C.; Mejía Morales, J.; De Smedt, S.C.; Tang, Z.; Xiong, R.; et al. Black Phosphorus Mediated Photoporation: A Broad Absorption Nanoplatform for Intracellular Delivery of Macromolecules. Nanoscale 2021, 13, 17049–17056.

21. Bergeron, E.; Boutopoulos, C.; Martel, R.; Torres, A.; Rodriguez, C.; Niskanen, J.; Lebrun, J.-J.; Winnik, F.M.; Sapieha, P.; Meunier, M. Cell-Specific Optoporation with near-Infrared Ultrafast Laser and Functionalized Gold Nanoparticles. Nanoscale 2015, 7, 17836–17847.

22. Patskovsky, S.; Qi, M.; Meunier, M. Single Point Single-Cell Nanoparticle Mediated Pulsed Laser Optoporation. Analyst 2020, 145, 523–529.

23. Aniket Mishra, Hirofumi Yamamoto, Shunya Okamoto, Takayuki Shibata, Moeto Nagai, Dual Use of Laser Shockwave with Beta-Carotene Embedded Gelatin Film: Intracellular Delivery and Manipulation. In Proceedings of the Proceedings of JSPE Semestrial Meeting 2023 JSPE Autumn Conference; The Japan Society for Precision Engineering: Fukuoka, August 1, 2023; 747–748.

24. Hosokawa, Y.; Takabayashi, H.; Miura, S.; Shukunami, C.; Hiraki, Y.; Masuhara, H. Nondestructive Isolation of Single Cultured Animal Cells by Femtosecond Laser-Induced Shockwave. In Proceedings of the Applied Physics A: Materials Science and Processing; Springer Verlag, 2004, 79, 795–798.

25. Jung, H.S.; Verwilst, P.; Sharma, A.; Shin, J.; Sessler, J.L.; Kim, J.S. Organic Molecule-Based Photothermal Agents: An Expanding Photothermal Therapy Universe. Chem Soc Rev 2018, 47, 2280–2297.

26. Zhao, L.; Zhang, X.; Wang, X.; Guan, X.; Zhang, W.; Ma, J. Recent Advances in Selective Photothermal Therapy of Tumor. J Nanobiotechnology 2021, 19, 335.

27. Dacarro, G.; Taglietti, A.; Pallavicini, P. Prussian Blue Nanoparticles as a Versatile Photothermal Tool. Molecules 2018, 23(6), 1414.

28. Zharov, V.P.; Galitovsky, V.; Viegas, M. Photothermal Detection of Local Thermal Effects during Selective Nanophotothermolysis. Appl Phys Lett 2003, 83, 4897–4899.

29. Li, Y.; Wang, X.; Gao, L.; Hu, P.; Jiang, L.; Ren, T.; Fu, R.; Yang, D.; Jiang, X. Aptamer-Conjugated Gold Nanostars for Targeted Cancer Photothermal Therapy. J Mater Sci 2018, 53, 14138–14148.

30. Raghavan, V.; O'Flatharta, C.; Dwyer, R.; Breathnach, A.; Zafar, H.; Dockery, P.; Wheatley, A.; Keogh, I.; Leahy, M.; Olivo, M. Dual Plasmonic Gold Nanostars for Photoacoustic Imaging and Photothermal Therapy. Nanomedicine 2017, 12, 457–471.

31. Hoffman, H.A.; Chakrabarti, L.; Dumont, M.F.; Sandler, A.D.; Fernandes, R. Prussian Blue Nanoparticles for Laser-Induced Photothermal Therapy of Tumors. RSC Adv 2014, 4, 29729–29734.

32. Li, X.; Lovell, J.F.; Yoon, J.; Chen, X. Clinical Development and Potential of Photothermal and Photodynamic Therapies for Cancer. Nat Rev Clin Oncol 2020, 17, 657–674.

33. Vo-Dinh, T.; Liu, Y.; Crawford, B.M.; Wang, H.-N.; Yuan, H.; Register, J.K.; Khoury, C.G. Shining Gold Nanostars: From Cancer Diagnostics to Photothermal Treatment and Immunotherapy, 2018; Vol. 2(1), 1-8.

34. Schneckenburger, H.; Hendinger, A.; Sailer, R.; Strauss, W.S.L.; Schmitt, M. Laser-Assisted Optoporation of Single Cells. J Biomed Opt 2002, 7, 410.

35. Soman, P.; Zhang, W.; Umeda, A.; Zhang, Z.J.; Chen, S. Femtosecond Laser-Assisted Optoporation for Drug and Gene Delivery into Single Mammalian Cells. J Biomed Nanotechnol 2011, 7, 334–341.

36. Wilson, A.M.; Mazzaferri, J.; Bergeron, É.; Patskovsky, S.; Marcoux-Valiquette, P.; Costantino, S.; Sapieha, P.; Meunier, M. In Vivo Laser-Mediated Retinal Ganglion Cell Optoporation Using KV1.1 Conjugated Gold Nanoparticles. Nano Lett 2018, 18, 6981–6988.

37. Yao, C.; Rudnitzki, F.; He, Y.; Zhang, Z.; Hüttmann, G.; Rahmanzadeh, R. Cancer Cell-Specific Protein Delivery by Optoporation with Laser-Irradiated Gold Nanorods. J Biophotonics 2020, 13, 1–10.

38. Kumar, S.; Li, A.; Thadhani, N.N.; Prausnitz, M.R. Optimization of Intracellular Macromolecule Delivery by Nanoparticle-Mediated Photoporation. Nanomedicine 2021, 37, 102431.

39. Illath, K.; Narasimhan, A.K.; Shinde, P.; Wankhar, S.; Nagai, M.; Santra, T.S. Intracellular Delivery Using Anisotropic Gold Nanocrystals Synthesized by Microfluidic Device. 15th IEEE International Conference on Nano/Micro Engineered and Molecular System, NEMS 2020 2020, 448–452.

40. Ramon, J.; Xiong, R.; De Smedt, S.C.; Raemdonck, K.; Braeckmans, K. Vapor Nanobubble-Mediated Photoporation Constitutes a Versatile Intracellular Delivery Technology. Curr Opin Colloid Interface Sci 2021, 54, 101453.

41. Wu, Y.C.; Wu, T.H.; Clemens, D.L.; Lee, B.Y.; Wen, X.; Horwitz, M.A.; Teitell, M.A.; Chiou, P.Y. Massively Parallel Delivery of Large Cargo into Mammalian Cells with Light Pulses. Nat Methods 2015, 12, 439–444.

42. Mohan, L.; Kar, S.; Ren Hattori; Ishii-Teshima, M.; Bera, P.; Roy, S.; Santra, T.S.; Shibata, T.; Nagai, M. Can Titanium Oxide Nanotubes Facilitate Intracellular Delivery by Laser-Assisted Photoporation? Appl Surf Sci 2021, 543, 148815.

43. Shinde, P.; Kar, S.; Loganathan, M.; Chang, H.Y.; Tseng, F.G.; Nagai, M.; Santra, T.S. Infrared Pulse Laser-Activated Highly Efficient Intracellular Delivery Using Titanium Microdish Device. ACS Biomater Sci Eng 2020, 6, 5645–5652.

44. Steger, A.C.; Lees, W.R.; Walmsley, K.; Bown, S.G. Interstitial Laser Hyperthermia: A New Approach to Local Destruction of Tumours. Br Med J 1989, 299, 362–365.

45. Sokolovski, S.G.; Zolotovskaya, S.A.; Goltsov, A.; Pourreyron, C.; South, A.P.; Rafailov, E.U. Infrared Laser Pulse Triggers Increased Singlet Oxygen Production in Tumour Cells. Sci Rep 2013, 3, 3484.

46. Breunig, H.G.; Batista, A.; Uchugonova, A.; König, K. Cell Optoporation with a Sub-15 Fs and a 250-Fs Laser. J Biomed Opt 2016, 21, 060501.

47. Hoffman, H.A.; Chakrabarti, L.; Dumont, M.F.; Sandler, A.D.; Fernandes, R. Prussian Blue Nanoparticles for Laser-Induced Photothermal Therapy of Tumors. RSC Adv 2014, 4, 29729–29734.

48. Mohan, L.; Kar, S.; Nagai, M.; Santra, T.S. Electrochemical Fabrication of TiO2 Micro-Flowers for an Efficient Intracellular Delivery Using Nanosecond Light Pulse. Mater Chem Phys 2021, 267, 124604.

49. Lukianova-Hleb, E.Y.; Wagner, D.S.; Brenner, M.K.; Lapotko, D.O. Cell-Specific Transmembrane Injection of Molecular Cargo with Gold Nanoparticle-Generated Transient Plasmonic Nanobubbles. Biomaterials 2012, 33, 5441–5450.

50. Schomaker, M.; Killian, D.; Willenbrock, S.; Heinemann, D.; Kalies, S.; Ngezahayo, A.; Nolte, I.; Ripken, T.; Junghanß, C.; Meyer, H.; et al. Biophysical Effects in Off-Resonant Gold Nanoparticle Mediated (GNOME) Laser Transfection of Cell Lines, Primary- and Stem Cells Using Fs Laser Pulses. J Biophotonics 2015, 8, 646–658.

51. Liu, X.; Zhou, W.; Wang, T.; Miao, S.; Lan, S.; Wei, Z.; Meng, Z.; Dai, Q.; Fan, H. Highly Localized, Efficient, and Rapid Photothermal Therapy Using Gold Nanobipyramids for Liver Cancer Cells Triggered by Femtosecond Laser. Sci Rep 2023, 13, 3372.

52. Shinde, A.; Shinde, P.; Kar, S.; Illath, K.; Dey, S.; Mahapatra, N.R.; Nagai, M.; Santra, T.S. Metallic Micro-Ring Device for Highly Efficient Large Cargo Delivery in Mammalian Cells Using Infrared Light Pulses. Lab Chip 2023, 23, 2175-2192.

53. Kalies, S.; Keil, S.; Sender, S.; Hammer, S.C.; Antonopoulos, G.C.; Schomaker, M.; Ripken, T.; Escobar, H.M.; Meyer, H.; Heinemann, D. Characterization of the Cellular Response Triggered by Gold Nanoparticle–Mediated Laser Manipulation. J Biomed Opt 2015, 20, 115005.

54. Maksimova, I.L.; Akchurin, G.G.; Khlebtsov, B.N.; Terentyuk, G.S.; Akchurin, G.G.; Ermolaev, I.A.; Skaptsov, A.A.; Soboleva, E.P.; Khlebtsov, N.G.; Tuchin, V. V. Near-Infrared Laser Photothermal Therapy of Cancer by Using Gold Nanoparticles: Computer Simulations and Experiment. Med. Laser Appl 2007, 22, 199–206.

55. Heinemann, D.; Kalies, S.; Schomaker, M.; Ertmer, W.; Murua Escobar, H.; Meyer, H.; Ripken, T. Delivery of Proteins to Mammalian Cells via Gold Nanoparticle Mediated Laser Transfection. Nanotechnology 2014, 25(24), 245101.

56. Huang, X.; Jain, P.K.; El-Sayed, I.H.; El-Sayed, M.A. Plasmonic Photothermal Therapy (PPTT) Using Gold Nanoparticles. Lasers Med Sci 2008, 23, 217–228.

57. Nakashima, Y.; Yamamoto, Y.; Hikichi, Y.; Nakanishi, Y. Creation of Cell Micropatterns Using a Newly Developed Gel Micromachining Technique. Biofabrication 2016, 8(3), 035006.

58. Deglincerti, A.; Etoc, F.; Guerra, M.C.; Martyn, I.; Metzger, J.; Ruzo, A.; Simunovic, M.; Yoney, A.; Brivanlou, A.H.; Siggia, E.; et al. Self-Organization of Human Embryonic Stem Cells on Micropatterns. Nat Protoc 2016, 11, 2223–2232.

59. Fluorescein Isothiocyanate-Dextran Sigma Stock, https://www.sigmaaldrich.com/JP/en/technical-documents/technical-article/cell-culture-and-cell-culture-analysis/imaging-analysis-and-live-cell-imaging/fluorescently-labeled-dextrane?srsltid=AfmBOoq65XZ749x9o4wvVZW0aqmDhHECvd53UflPEZrN3HDA48sTJxeZ

Chapter 4: Cell Perforation for Photothermal Therapy: Visible Pulsed Laser-assisted Selective Killing of Cancer Cells with PVP-capped Plasmonic Gold Nanostars

4.1 Introduction

Cancer is one of the biggest causes of a high number of deaths worldwide. Advances in nanotechnology have opened the doors for new cancer therapy strategies in the previous two decades [1, 2]. Gold nanoparticles have been utilized in a plethora of biomedical applications, such as bioimaging, biosensing [3], photothermal therapy, photodynamic therapy [4], antibacterial treatment [5, 6], and drug delivery [7, 8]. Gold nanoparticles offer excellent potential for biomedical applications due to their highly biocompatible nature and plasmonic properties. The plasmonic characteristics of nanoparticles are highly dependent upon the structure of a synthesized nanomaterial, and drastic changes in the plasmonic properties can be observed upon changing the surface morphology and synthesis method [9, 10]. Numerous pointed branches of gold nanostars (GNS) create a “lightning rod” effect and considerably enhance the local electromagnetic field [11]. The considerable electromagnetic field increment causes strong light absorption properties and effective energy conversion for heating tumor cells in experiments using nanoparticle-mediated photothermal therapy.

A combination of resonance enhancement and “the lightning rod effect” causes the large field amplification at the star’s tips due to the extreme curvature of nanostars, where a stronger electric (E) field and a higher charge density are produced. Therefore, nanostars can create E-field hotspots and are far more effective than relatively smoother particles, such as nanospheres, nanorods, and nanodiscs for applications such as surface-enhanced Raman scattering (SERS), bioimaging, and photothermal therapy (PTT) [12-14].

The plasmonics of GNS have been studied using a variety of analytical and empirical strategies, including label-free biosensing [15], two-photon photoluminescence, and SERS activity [16]. Different syntheses of gold nanostars involve the use of various non-biocompatible chemicals, such as cetyltrimethylammonium bromide (CTAB), which is cytotoxic and affects cell viability [17]. Hence a facile, reproducible, and biocompatible reactant-assisted synthesis of gold nanoparticles is needed for more optimum applications of gold nanoparticles in various biomedical applications, such as drug delivery, photodynamic therapy, and photothermal therapy.

PTT has special benefits in therapeutic strategies for cancer treatment, including high selectivity resulting in minimal invasiveness and precise spatial–temporal selection [18-19]. It can be compared to other methods, such as immunotherapy, which have quite a low response rate and immune-related adverse effects, and chemotherapy, which can cause induce significant toxicity in healthy cells [20]. Initially, PTT was tested without photosensitizing agents; however, a high laser power was needed, and the requirement of integrated fiber cooling systems hampered the simple treatment system. A contrast agent was added to PPT, which allowed for the use of lower power lasers and system simplification of PPT. The laser wavelength is either in the visual spectrum using spherical gold nanoparticles or in the near-infrared (NIR) region using NIR-absorbing gold-based nanoparticles depending on the surface plasmon resonance (SPR) wavelength. CW NIR lasers are generally used for application in photothermal therapy because only a little supply of continuous laser light provides considerable heating. Huang et al. used various shapes of gold nanoparticles, including nanocages, nanospheres, and nanorods, for the photothermal therapy of cells by using NIR continuous wave (CW) lasers at different wavelengths [21]. Gold nanostars (GNS) were used for PTT with a NIR CW laser [22]. CW lasers have significant heat-affected zones and affect the viability of cells. The disadvantage of a heat-affected zone with a CW laser in photothermal

experiments can be reduced by a short-pulse laser, such as femtosecond lasers [18-19, 23], and nanosecond pulse lasers [24-25].

The combination of GNS and visible pulsed laser irradiation for PTT is promising, but it has not been reported yet. GNS were mostly irradiated in the IR range [12, 14, 26-30]. A visible nanosecond pulsed laser was used for GNP-assisted PTT [31-32]. Mahmoodazeh et al. used GNP@polymer-DOX theranostic medicine and demonstrated chemo-photothermal therapy of solid tumors [31]. Zharov et al. investigated laser-induced microbubbles around gold nanoparticles upon laser irradiation [32]. The heat conversion rate of gold nanoparticles in the visible region is better [13] than that of the NIR laser. The combination of GNS and visible pulsed laser irradiation is expected to establish an efficient and less invasive photothermal treatment.

This study aims to develop a low-cost, efficient, and less invasive cancer treatment that limits tumor development or eradicates tumors. We have prepared gold nanoparticles with star-shaped morphology via highly biocompatible one-pot synthesis. To increase the throughput of the process, we have used a visible nanosecond pulse laser for the photothermal treatment of cancer cells. The nanoparticles were incubated over cancer cells, and upon irradiation with a laser, site-specific cell death was confirmed using fluorescence imaging.

4.2 Materials and Methods

4.2.1 Preparation of PVP-Capped Au Nanostars

GNS were synthesized using a simple solution process (Figure 4.1) with some modifications [33]. A total of 3 ml of deionized water was mixed with 2 ml HEPES (4-(2-hydroxyethyl)-1-piperazineethanesulfonic acid, 100 mM). HEPES is a Good's Buffer and has minimal salt and temperature effects on the buffering capacity. HEPES produces nitrogen-centered free radicals and reduces gold ions, and it serves as an effective, weak reducing and

capping agent [33]. HEPES concentration plays a crucial role in controlling the branched length of the particles and affects the shape and size of GNS [34]. A total of 20 µl of 50 mM HAuCl4 (chloroauric acid) was added, and the solution was mixed gently via inversion. The prepared solution was left to stand until a change in color from transparent to blue was observed, which took almost 30 minutes. The color change signifies a reduction of $HAuCl_4$, and the change was monitored carefully, as it might affect the final concentration of GNS. Then, 600 µl of polyvinylpyrrolidone (PVP, 25 mM) was added and gently mixed. After 1 day, the solution was centrifuged at 220 g for 50 min to remove unadhered PVP from the GNS. The supernatant was removed, and the nanoparticles were suspended in DI water.

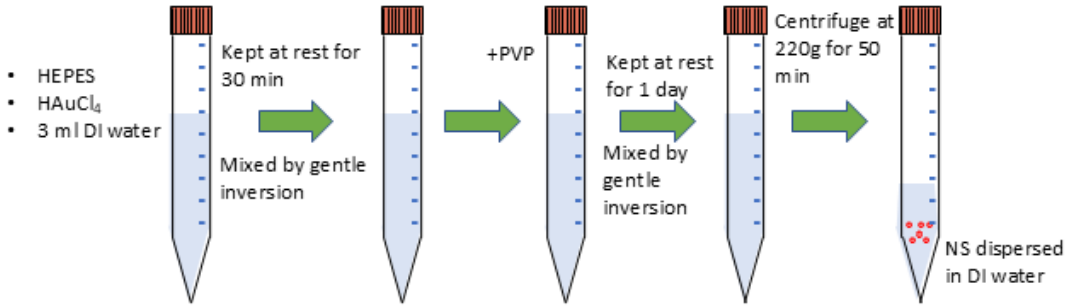

Figure 4.1 Synthesis of gold nanostars.

4.2.2 Cell Culture

HeLa cells were cultured in minimum essential medium (MEM, Gibco, 11095072, USA) with 10% fetal bovine serum (FBS, CCP-FBS-BR-500, Cosmo Bio) and 1% penicillin-streptomycin (PS) for three days. The adherence of HEK-293 cells to the petri dish was relatively weak; hence, the glass petri dish was coated with fibronectin before seeding cells. For HEK-293 cells, glass petri dishes were first coated with fibronectin and placed in a humidified atmosphere incubator with 5%CO_2 at 37 °C. After coating the dish with fibronectin,

HEK-293 cells were cultured. Both HEK-293 and SAOS-2 cells were cultured using high-glucose DMEM with 10% FBS and 1% penicillin-streptomycin (PS).

4.2.3 Procedure for Site-Specific Killing of Cancer Cells

The medium containing cultured cells was removed, and the cells were washed twice with phosphate-buffered saline (PBS). Then, a new colorless modified Dulbecco's modified eagle medium (DMEM) was used for cancer cell-killing experiments. After the fresh medium was added, the cells were incubated with four different concentrations of PVP-Capped GNS, ρ = 20 µg/mL, 15 µg/mL, 10 µg/mL, and 5 µg/mL, named respectively ρ_A to $\rho_{D,}$ and incubated in 5% CO_2 supply incubator for 4 hours. Then the medium was removed, and cells were washed with PBS twice to remove unadhered PVP-capped GNS. After washing, fresh DMEM was added. Then, 4µM of propidium iodide (PI) was added for indication of laser-induced cancer cell killing. To observe cell viability, the medium was removed, and cells were washed with PBS twice. A new medium was added, followed by the addition of Calcein-AM. The cells were observed with the inverted microscope (Nikon, ECLIPSE Ti-E) and microscope camera (Nikon, DS-Fi3).

4.2.4 Experimental Setup

The experimental setup consisted of irradiation, scanning, and observation systems (Figure 4.2(a), (b). Irradiation system: We used a nanosecond pulsed laser (Cobolt, TorTM XS, Hubner Photonics, Solna, Sweden) with a gaussian profile, a wavelength of 532 nm, a pulse of 5 ns, and a frequency of 1 kHz. The laser was controlled with a digital function generator. The laser light was reflected through a mirror for alignment. A dichroic mirror (Thorlabs, DMLP550R, Newton, NJ, USA) reflected the laser and combined observation light. The original diameter of the laser beam was 1.1 ± 0.3 mm, and a convex lens of focal length 50 mm focused the laser on a sample.

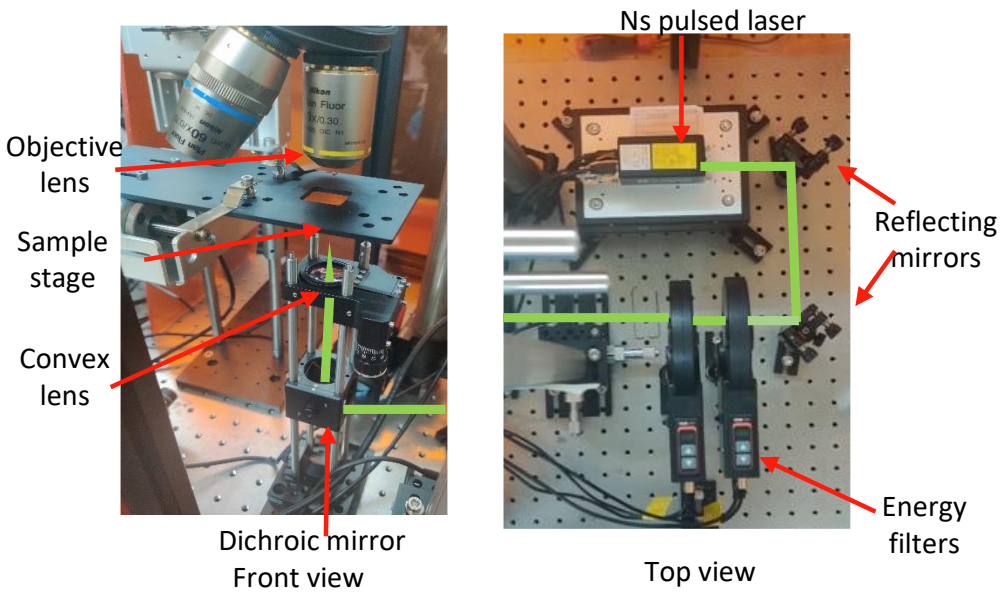

Figure 4.2 Experimental setup for site-specific selective killing of cancer cells.

Scanning system: A Cartesian robot (IAI Corporation) was used for scanning a sample. The scanning speed was kept constant at 100 mm/s for all the experiments.

Observation system: The samples were observed using a CMOS (ZWO, ASL1600MC Cool, Suzhou, China) camera and an observation light (Thorlabs, MWWHLP1). The samples were visualized using the ImageJ webcam plugin.

4.2.5 Data Analysis

The cell-killing efficiency of spot irradiation was calculated from an average of five irradiation spots for each experimental condition. All the experiments were performed in triplets, and efficiency was reported as mean±standard deviation for three independent experiments. In the case of the scanning laser, the efficiency was calculated by counting the number of cells along the laser path for 1000 µm for three different scan paths for each parameter for a single experiment, and the reported efficiency is the mean±standard deviation of three independent experiments. No effect of laser on cells leads to 0% cell killing, and

peeling off cells upon laser irradiation is defined as 100% cell killing efficiency. To evaluate cell killing efficiency in the case of single pulse spot irradiation, the number of dead cells and live cells within the laser circumference of the irradiated spot was calculated, and the efficiency was evaluated. For continuous pulse laser-induced cancer cell killing, the cell killing efficiency was evaluated by counting the number of dead cells and live cells along the path of laser irradiation, and the efficiency, η, was evaluated as follows by Eq. 4.1 (except peeling off cells at higher laser energies):

$$\eta = \frac{N_R}{N_R + N_G} \times 100 \qquad \ldots(4.1)$$

where N_R and N_G are respectively the numbers of PI-stained and calcein-AM-stained cells.

4.3 Simulation of Temperature Rise in Gold Nanostars upon Laser Irradiation

4.3.1 Simulation Method

We performed heat transfer simulations in COMSOL Multiphysics to confirm that the heat upon laser irradiation on gold nanostars is generated more than on gold nanospheres. Such higher heat generation allows for the site-specific killing at lower laser energy, resulting in less effect on cells in the vicinity. A 2-D Gaussian laser pulse, irradiated on gold nanoparticles, is modeled by [35].

$$S(t) = \frac{0.94 \times F_{abs}}{\delta t_p} \exp\left[-4\ln(2) \times \left(\frac{t - 2t_p}{t_p}\right)^2\right. \qquad \ldots(4.2)$$

Q_{in} represents total heat load, Q_o represents total input power, R_c Is the reflection coefficient, A_c is the absorption coefficient, within x and y coordinates, σ_x is the standard deviation in the x-direction, and σ_y is standard deviation in the y-direction. To obtain the temperature rise of gold in both shapes, two temperature models were considered [2], [28]. An irradiated laser pulse resulted in a rise in the temperature of the electron layer T_e in the

respective specimen. The heat from the electron layer was transferred to a gold lattice covered with polyvinyl pyrrolidone, which raised lattice temperature T_l. Finally, the heat was dissipated into the water body into which nanoparticles were immersed separately. The temperature rise T_m of water bodies was observed.

$$C_e(T_e)\frac{\partial T_e}{\partial t} = \nabla(k_e \nabla T_e) - g(T_e - T_l) + Q(t) \quad \ldots(4.3)$$

$$C_l\frac{\partial T_l}{\partial t} = \nabla(k_l \nabla T_l) - g(T_l - T_e) + Q(t) \quad \ldots.(4.4)\eta = \frac{N_R}{N_R + N_G} \times 100 \quad \ldots(4.4)$$

$$\rho_m(r)c_m(r)\frac{\partial T_m(r,t)}{\partial t} = \nabla.\left(k_m.\nabla T_m(r,t)\right) + F(t)\eta = \frac{N_R}{N_R + N_G} \times 100 \quad \ldots(4.5)$$

, where $C_e(T_e) = {}^{\gamma}T_e$ with ${}^{\gamma}$= 70 Jm $^{-3}$K^{-2} is the electron heat capacity of gold, C_l is the lattice heat capacity of gold, k_e = 300 Wm $^{-1}$K^{-1} [8] is electron thermal conductivity, k_l = 2.7 Wm^{-1}K^{-1} [1] is the lattice thermal conductivity, g = 2*10^{16} Wm^{-3}K^{-1} [8] is the gold electron phonon coupling element, C_m = 4182 Jm^{-3}K^{-1} [8] is the water heat capacity, and k_m = 0.6 Wm^{-1}K^{-1} is the water thermal conductivity. The laser was irradiated at a fluence of 100 mJ/cm2. The function *F(t)* represents the heat transfer at the interface between the GNS and the surrounding area. All parameters were obtained from [8].

4.3.2 Simulation Result and Discussion

Simulation results in Figure 4.3(a, b) show the temperature rise in star-shaped nanoparticles. The figures show that the temperature rise in a star shape is almost double the temperature rise in a spherical shape. In Figure 4.3(b), an interesting phenomenon of higher temperature in star spikes as compared to the star core can be seen. This is because during heating, spikes primarily come in contact with laser heat, whereas certain areas of the cone in contact with the base of spikes do not directly receive heat. Also, it can be seen that the surface area of a gold nano star is larger than compared of a gold nano sphere. Due to the higher surface

area, heat gain is also increased. Due to these reasons, there is localized heating in spikes on a nano star, which overall increases the temperature of a particle. This explains the reasons for almost double the temperatures observed in a nano star as compared to a nano sphere.

Figures 4.3(c, d) indicate the temperature rise in sphere-and-star-shaped nanoparticles against time. Simulation time for gold nanosphere and nano star was 15 ns. Maximum temperature for a gold nano star was 2200 K and for a nanosphere was 1000 K. By comparing all the results, we can see that the temperature rises and falls for star shape are much larger than for sphere shape, this may be because there is heat accumulation in the star spikes leading to localized heating resulting in higher temperature rises.

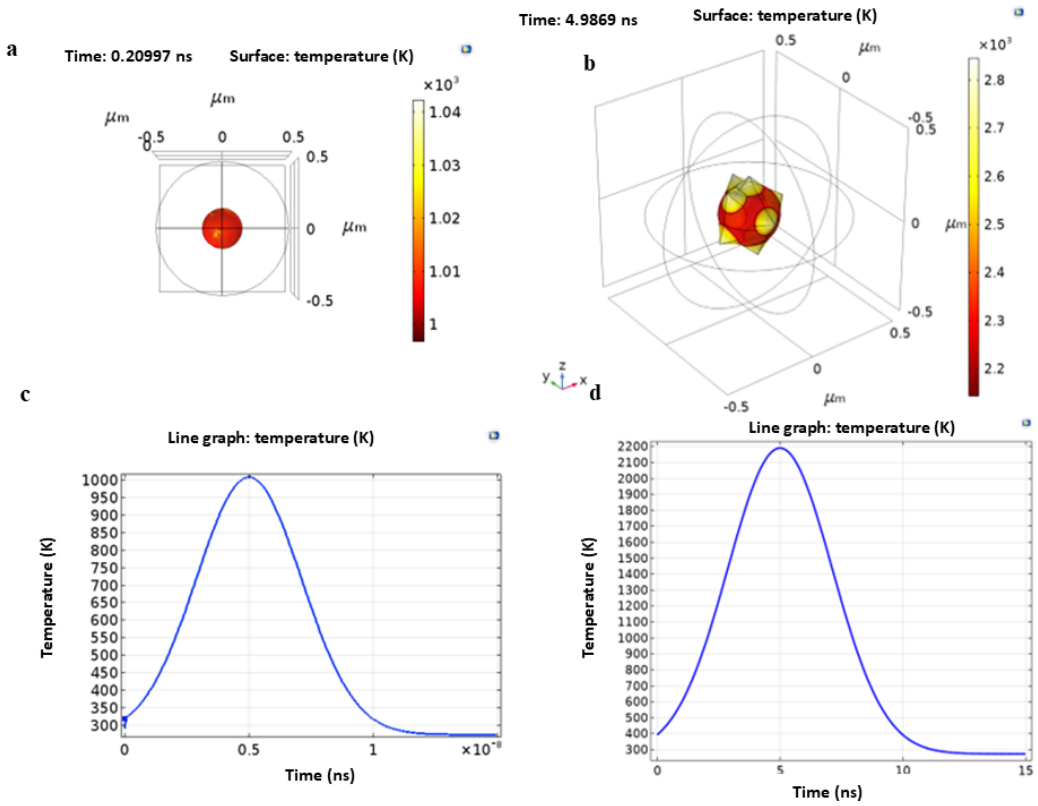

Figure 4.3 Comsol multiphysics simulation results for pulse laser irradiation on gold nanoparticles. (a) Temperature rise in gold nanosphere. (b) Temperature rise in star-shaped gold nanoparticle. (c) Maximum temperature rise of the nanosphere core. (d) Maximum temperature rise of the core of a star-shaped nanoparticle.

4.4 Experimental Results

4.4.1 FESEM Analysis and UV-Visible Spectroscopy Analysis

The prepared nanomaterials were characterized using field emission scanning electron microscopy (FESEM) for morphological analysis. Figure 4.4(a) represents PVP-capped gold nanoparticles in star morphology; the pointed tips appearing in the image provide hotspots for field enhancement on the plasmonic gold nanoparticle. Hotspots are the specific locations on the NPs where electric field enhancement occurs upon laser illumination. GNS offers more hotspots in comparison to other shapes like nanotubes or nanospheres. PVP cap can be visually observed in FESEM. The arrows indicate PVP caps. Our nanosecond pulsed laser has a wavelength of 532 nm, and we checked that the prepared nanoparticles absorb the laser light around this wavelength under UV-vis spectroscopy. UV-VIS (Figure 4.4(b)) shows that the prepared nanoparticles absorb the given laser light with a maximum absorption peak of around 532 nm.

Smaller nanoparticles have been reported to get transported into the cell cytosol via endocytosis [36]; hence, we have preferred to use particles with relatively bigger sizes that allow for cell killing to occur due to ion imbalance because of irreversible pore creation on the cell membrane. Commonly, nanoparticles with a size of 200 nm have been used for photothermal biomedical experiments [37,38]. The size of gold nanostars as measured using a laser diffraction particle size analyzer (SALD 2300, Shimadzu) revealed that 90% of particles were under 262 nm, whereas the mean particle size was 204 nm, as depicted in Figure 4(c).

The X-ray diffractometer (XRD, Rigaku ULTIMA IV R185) analysis (Figure. 4.4d) of the nanoparticles on a silicon wafer revealed the presence of peaks at 38.46(1 1 1), 44.78°(2 0 0), and 62.1°(2 2 0) which is identical with standard gold metal(Au^0) concerning JCPSD no. 04-0784. XRD indicates the presence of a face-centered cubic (FCC) structure of Gold(Au).

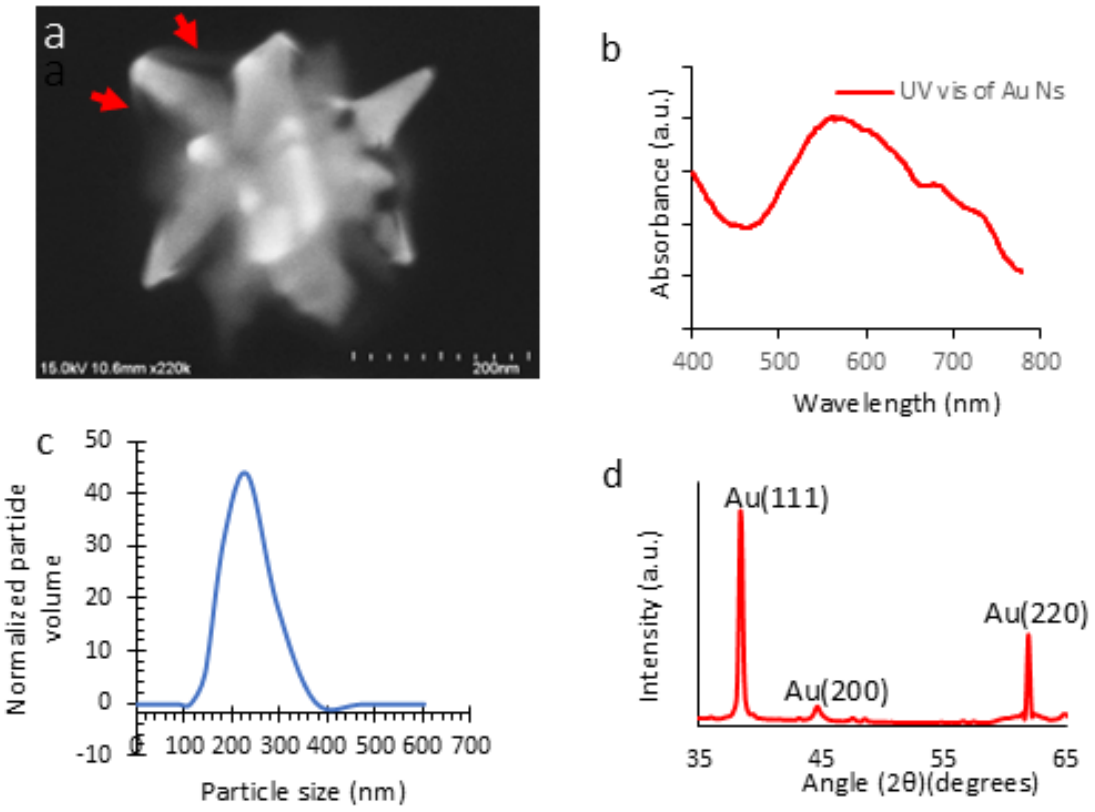

Figure 4.4 Characterization of PVP-capped gold nanostars. (a) FESEM. (b) UV-Visible spectroscopy. (c) Particle size analysis. (d) XRD analysis of prepared particles.

4.4.2 Site-specific Cancer Cell Killing with Single Pulse

Fluorescence microscopy was used to examine cancer cells that had been killed at specific sites. HeLa cells at the highest concentration (ρ_A: 20 µg/mL) in case of spot irradiation were peeled off from the surface of the glass-bottom Petri dish due to the high magnitude of shock wave generation upon laser irradiation (Figure 4.5(d)), whereas the cells at the other concentrations (ρ_B: 15µg/mL, ρ_C: 10 µg/mL) unadhered only at the highest laser fluence of 192 mJ/cm^2. The efficiency of cell death was assessed at lower fluences (Figure 4.5(a–c)), and as laser fluence and particle concentration increase, so does the efficiency of cell death (Figure 4.5(f)). The cells were unaffected by the laser irradiation at the lowest concentration (ρ_D: 5 µg/mL) and the lowest laser fluence of 19 mJ/cm^2 due to an insufficient amount of laser effect.

Next, we tested the efficacy of our system for site-induced cell killing in the HEK-293 cell line. Single pulse laser irradiation at higher energies at ρ_A detached the HEK-293 cells from the substrate, similar to that of HeLa cells. At lower concentrations (ρ_B, ρ_C), the cell death efficiency increased upon increasing the laser fluence. Upon decreasing the particle concentration from ρ_B to ρ_C (Figure 5(g)), the cell killing efficiencies were comparable at 78mJ/cm^2 and 92 mJ/cm^2 (Figure 4.5(c)) and different at maximum and minimum laser fluence. For the lowest concentration of photosensitizer nanoparticles (ρ_D), the cells were unaffected by laser irradiation. It implies that a laser with various fluences at a concentration is unable to generate enough vapor nanobubbles essential for the generation of the shock wave to induce pores on the cell wall, where the pores possibly create electrolyte imbalance and induce cell death due to heterogeneity found in different cell lines (HeLa and HEK-293).

We tested our system on a human osteosarcoma cell line (SAOS-2) and verified that our method can be applied to various cancer cell lines (Figure 4.5(h)). As both laser fluence and particle concentration increased, the cell killing efficiency increased. As a general trend, a notable change in efficiency was observed upon changing the laser fluence from 19 mJ/cm^2 to 78 mJ/cm^{2,} whereas the efficiency was almost similar upon further increasing the laser fluence from 78 mJ/cm^2 to 192 mJ/cm^2. As expected, the highest cell killing efficiency was observed at 192 mJ/cm^2 (Figure 5(e)). The cell killing efficiencies at ρ_B and ρ_C were almost comparable with respect to various fluences. The cells at ρ_A were observed to detach at a fluence of 192mJ/cm^2. In general, it can be concluded that the cancer cell-killing efficiency increases significantly upon increasing the laser fluence and the photosensitizer nanoparticle concentration.

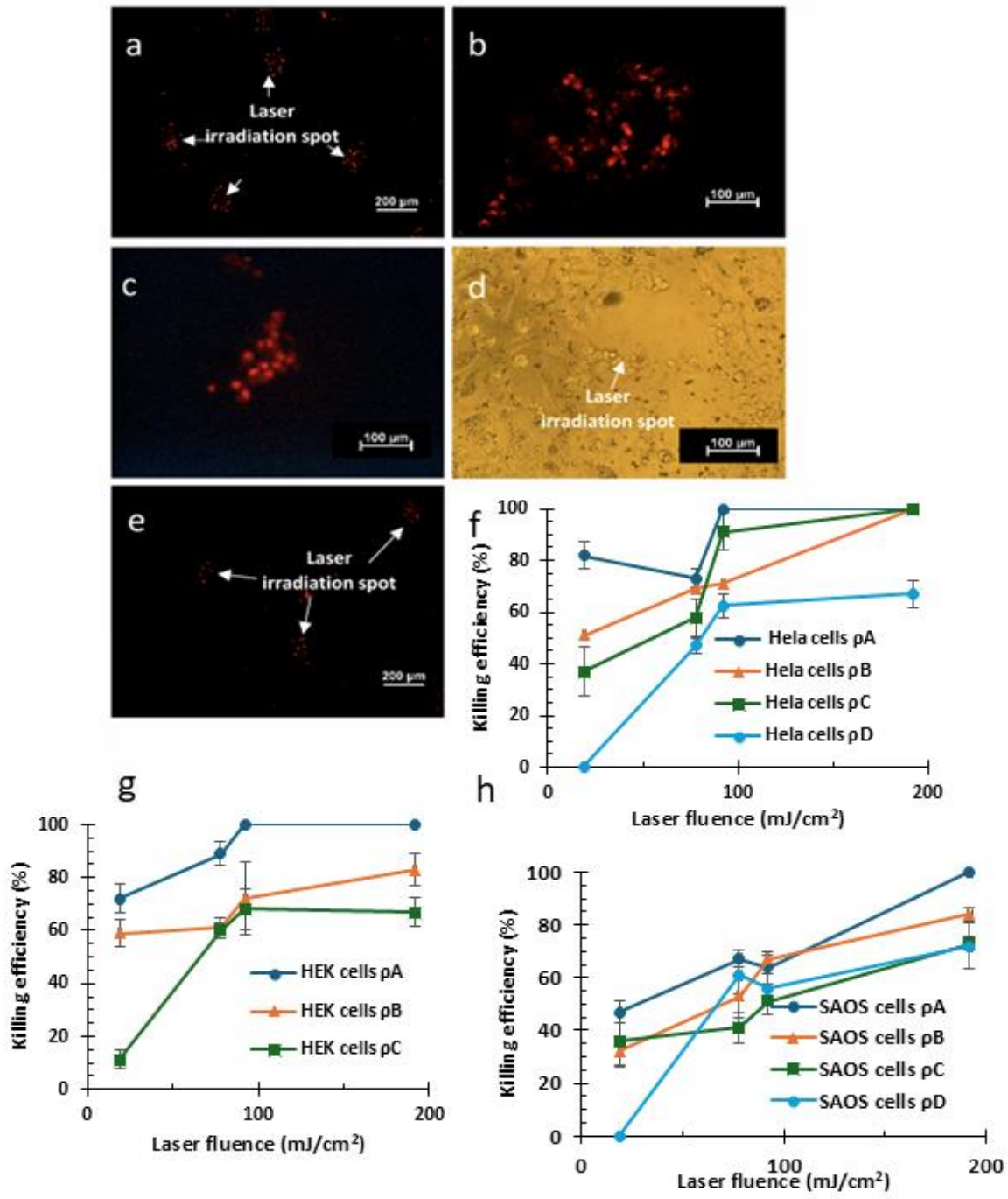

Figure 4.5 Single pulse spot irradiation killing. HeLa cells. (a) At 192 mJ/cm^2 at ρ_D. (b) 192 mJ/cm^2 at ρ_D. (c) HEK-293 cells at 92 mJ/cm^2 at ρ_C. (d) Peeling off HEK-293 cells at 92 mJ/cm^2 at ρ_A. (e) Spot irradiation of SAOS-2 cells at 192 mJ/cm^2 at ρ_B. Cell killing efficiency vs. laser fluence curve at various concentrations. (f) HeLa cells. (g) HEK-293 cells. (h) SAOS-2 cells.

4.4.3 Site-specific and High Throughput Scanning Laser-Induced Cell Killing

Continuous pulsed laser irradiation led to the irradiation of multiple laser pulses at a single spot, and the magnitude of the generated shock wave was stronger. At the highest concentration (ρ_A), cells were peeled off at all the laser fluences (Figure 4.6(d)). While at lower nanoparticle concentrations (ρ_C, ρ_D), high throughput site-specific HeLa cell killing was observed (Figure 6(a, b)), and the results were similar to spot irradiation, indicating an increment in cell killing efficiency when either the laser fluence or the nanoparticle concentration was increased. At ρ_C, 100% cell killing efficiency was observed at higher laser fluences. There was a significant difference in cell killing efficiency at ρ_C and ρ_D (Figure 4.6(f)). In the case of HEK cells, the continuous pulse laser irradiation of cells on the glass substrate resulted in the peeling of cells at the highest photosensitizer nanoparticle concentration (ρ_A), thus resulting in 100% cell killing efficiency at all the laser fluences. For the other concentrations (ρ_B, ρ_C) (Figure 4.6(c)), the cells were killed upon laser irradiation, and the efficiency was calculated. The cell killing efficiency was observed to be gradually increasing upon increasing Laser fluence, while the effect of decreasing the nanoparticle concentration (ρ_B, ρ_C) on the killing efficiency was negligible, as depicted in Figure 4.6(g).

SAOS-2 cells were peeled off at the highest concentration of photosensitizer nanoparticles. Figure 4.6(e) represents the high-throughput killing of SAOS-2 cells at 192 mJ/cm^2 at ρ_B. At ρ_B *and* ρ_C, cell killing efficiency was found to increase similarly to spot irradiation for the same cell line. That is, a gradual increase in the cell killing efficiency was observed upon increasing the laser for both concentrations (Figure 4.6(h)), while for ρ_D, the cell killing efficiency was almost comparable at various laser fluences. We can conclude that upon increasing particle concentration and laser energy increase in cell-killing efficiency has been observed, the reason for which will be further elaborated in the discussion section.

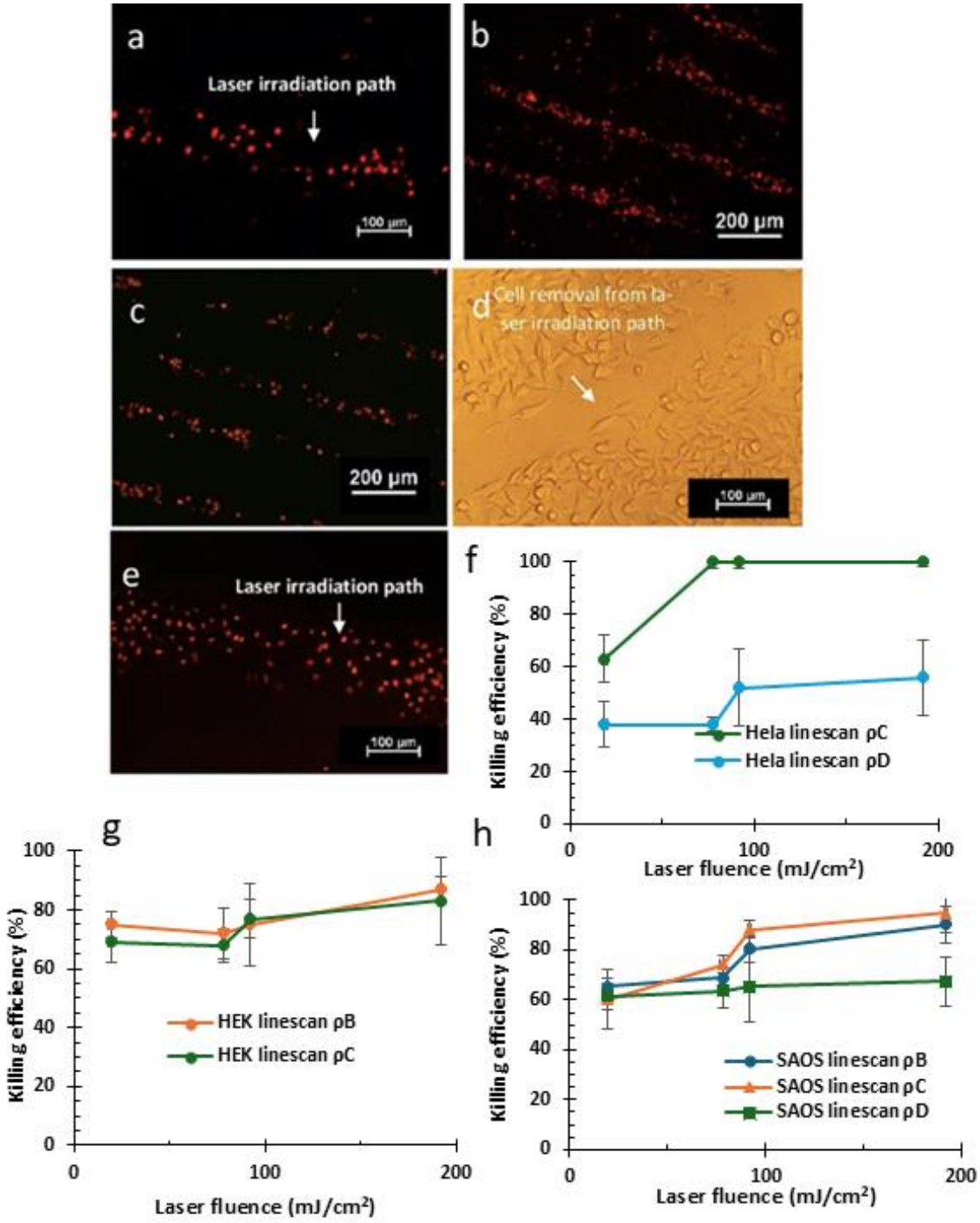

Figure 4.6 High Throughput scanning laser irradiation killing in HeLa cells (a) At ρ_C at 92 mJ/cm^2. (b) At ρ_B at 78 mJ/cm^2. (c) At ρ_C at 78 mJ/cm^2. (d) Peeling off of cells at higher laser fluence at ρ_A at 78 mJ/cm^2. (e) Scanning laser irradiation of SAOS-2 cells at 192 mJ/cm^2 at ρ_B. Cell killing Efficiency vs. Laser Fluence curve at various concentrations. (f) HeLa cells. (g) HEK-293 cells. (h) SAOS-2 cells.

4.4.4 Negative Control Experiments

Control experiments were carried out to confirm PVP-capped GNS-assisted visible pulsed laser-induced site-specific killing of cancer cells. The laser was not irradiated to a sample, and cells incubated with PVP-capped GNS control images were taken (Fig. 4.7 (a, b) HeLa cells). Cells without photo absorber incubation and laser irradiation (Figure 4.7 (c, d) HEK cells). Most cells were alive in both cases, which concludes that both particle incubation and laser irradiation are necessary for killing cancer cells.

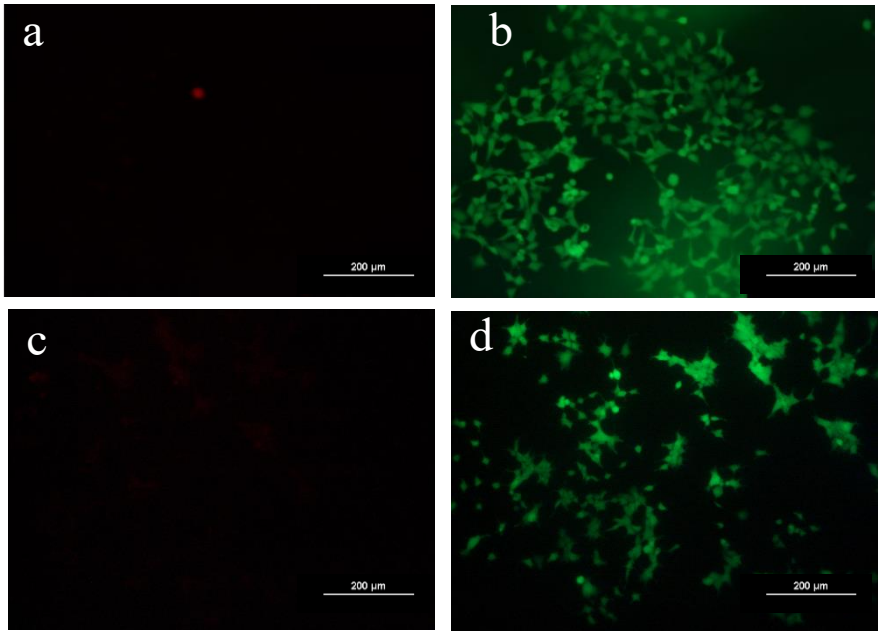

Figure 4.7 Negative control image without laser irradiation. (a) Dead cells (PI staining). (b) Live cells (Calcein-AM staining) HeLa cells and without photo absorber. (c) Dead cells. (d) Live cells (HEK-293 cells).

4.5 Discussion

The potential use of nanomaterials in a PTT strategy against cancer cells has been noted in several studies. Most of these studies have concentrated on using NIR to locally increase temperature and selectively induce cell death. However, visible light irradiation for PTT has been disregarded despite the greater visible light-to-heat conversion that occurs when

nanoparticles are irradiated with a laser, and only a few studies have reported the use of visible pulsed lasers in biomedical applications [39,40].

Several parameters play a crucial role in the photothermal treatment of cancer concerning photosensitizer particles; for example, the absorption efficiency for nanoparticles with a branched structure is more than that of spherical particles [41]. The size of nanoparticles can also affect the absorption efficiency, as smaller particles tend to absorb more light. The danger of adjacent cell damage and endocytosis is present; hence, for biomedical photothermal experiments, relatively bigger particles are preferred [39, 42]. Similarly, concentration also plays a crucial role in photothermal efficiency, while lower concentration results in insufficient absorption of light for treatment, while high concentration can result in damage to adjacent non-target cells.

The laser energy absorption of GNS can be explained by SPR. The prepared GNS absorbed the laser and converted it into heat. Efficient conversion needs the overlap of the absorption spectrum and the laser wavelength; less overlap reduces the absorbance. The laser wavelength 532 nm was in the absorbance region of the prepared GNS with a peak of 550 nm. Our study used a visible pulsed laser for the PTT of cancer cells. In addition to a nanosecond pulse laser, picosecond and femtosecond pulse lasers can be irradiated to GNS and are considered to lead to a smaller heat-affected zone.

According to the above model mentioned in the simulation results, when PVP-capped GNS are exposed to a nanosecond pulsed laser beam, the laser exposure raises the temperature of the electrons inside the GNS. This temperature rise, in turn, increases the lattice temperature of the GNS. After only a few picoseconds, the medium's temperature starts to rise because of electron–phonon interaction [43]. This increase in temperature causes the surrounding medium to produce vapor nanobubbles [44–46], which, when collapsed, cause stress on the membrane

and generate transitory pores. Cell death results from an imbalance in the concentration of electrolytes after the formation of holes in the cell membrane [47,48], as depicted in Figure 4.8. The other possible mechanism for cell death is heat transfer between GNS [49–51] and the cell membrane. Upon heat transfer to the cell membrane, local phase transition may occur in the lipid bilayer. Thermal denaturation of glycoproteins can take place [52], which might result in the opening of transient hydrophilic pores on the cell membrane, thus creating the electrolyte imbalance and initiating cell death.

The usual tumor size ranges from millimeters to centimeters, and for the site-specific killing of cancer cells, a highly fluent laser beam was focused on the sample by using a convex lens in dimensions of μm [53]. Certain skin pre-malignancies and cancers, as well as pre-cancers or extremely early stages of the cervix and nearby cancers, can be treated using this strategy of cancer therapeutics. Inside the body, cancers obstructing the airway and progressing from other locations to the lungs can be treated with lasers. Tumors in the breast, brain, skin, head, neck, cervical area, and lung can be eliminated using precise lasers; thus, this PTT can be used for the treatment of the same organs.

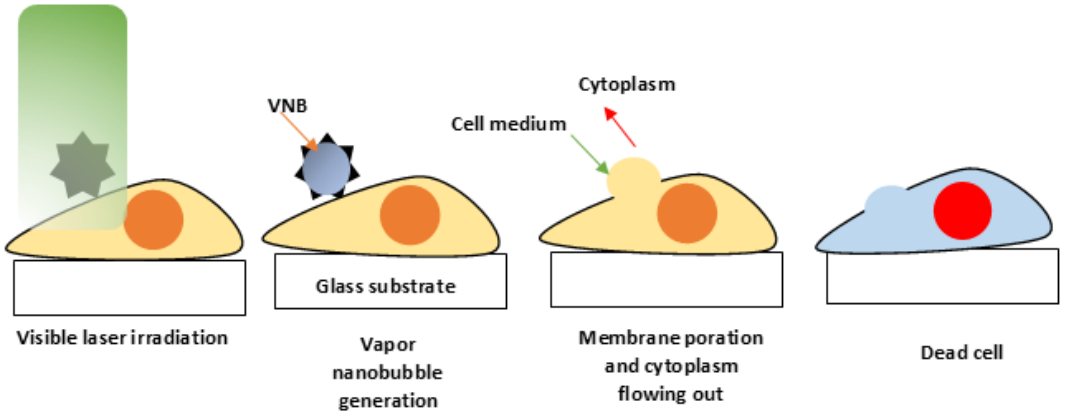

Figure 4.8 Schematic of cell death mechanism.

The other possible mechanism for cell death may be due to heat transfer that occurs between gold nanostars and the cell membrane, upon heat transfer to the cell membrane local phase transition may occur in the lipid bilayer or thermal denaturation of glycoproteins can take place that might result in the opening of transient hydrophilic pores on the cell membrane thus creating the electrolyte imbalance and initiating cell death.

4.6 Conclusions

In this chapter, we advanced our study of photoabsorber-assisted laser irradiation for pore creation to photothermal therapy with Gold nanostars. A nanosecond pulse laser was used to increase the throughput of the process as it can be utilized for selectively killing cancer cells in a small duration of time, a precisely to eliminate cancer cells with PVP-capped GNS. The nanostars were made using facile synthesis methods, and their characteristics were determined using FESEM, UV-visible spectroscopy, and XRD. Cancer cells cultivated on a glass petri dish were incubated with nanoparticles. The cells were exposed to the nanosecond pulse laser, and cell death was confirmed by observing PI-stained cell nuclei under a fluorescence microscope. The effect of variation of cell killing efficiency concerning laser fluence and particle concentration was analyzed, and we successfully analyzed three cell lines (HeLa, HEK-293, and SAOS-2). The efficiency of single-spot and high-throughput laser scanning cell killing was evaluated.

References

1. Brigger, I.; Dubernet, C.; Couvreur, P. Nanoparticles in Cancer Therapy and Diagnosis. Adv. Drug Deliv. Rev. 2012, 64, 24–36.
2. Yu, Z.; Gao, L.; Chen, K.; Zhang, W.; Zhang, Q.; Li, Q.; Hu, K. Nanoparticles: A New Approach to Upgrade Cancer Diagnosis and Treatment. Nanoscale Res. Lett. 2021, 16, 88.
3. Si, P.; Razmi, N.; Nur, O.; Solanki, S.; Pandey, C.M.; Gupta, R.K.; Malhotra, B.D.; Willander, M.; de La Zerda, A. Gold Nanomaterials for Optical Biosensing and Bioimaging. Nanosale Adv. 2021, 3, 2679–2698.
4. Shang, L.; Zhou, X.; Zhang, J.; Shi, Y.; Zhong, L. Metal Nanoparticles for Photodynamic Therapy: A Potential Treatment for Breast Cancer. Molecules 2021, 26, 6532.

5. Tian, E.K.; Wang, Y.; Ren, R.; Zheng, W.; Liao, W. Gold Nanoparticle: Recent Progress on Its Antibacterial Applications and Mechanisms. J. Nanomater. 2021, 2021, 2501345.

6. El-Gendy, A.O.; Obaid, Y.; Ahmed, E.; Enwemeka, C.S.; Hassan, M.; Mohamed, T. The Antimicrobial Effect of Gold Quantum Dots and Femtosecond Laser Irradiation on the Growth Kinetics of Common Infectious Eye Pathogens: An In Vitro Study. Nanomaterials 2022, 12, 3757.

7. Wilson, A.M.; Mazzaferri, J.; Bergeron, É.; Patskovsky, S.; Marcoux-Valiquette, P.; Costantino, S.; Sapieha, P.; Meunier, M. In Vivo Laser-Mediated Retinal Ganglion Cell Optoporation Using KV1.1 Conjugated Gold Nanoparticles. Nano Lett. 2018, 18, 6981–6988.

8. Santra, T.S.; Kar, S.; Chen, T.C.; Chen, C.W.; Borana, J.; Lee, M.C.; Tseng, F.G. Near-Infrared Nanosecond-Pulsed Laser-Activated Highly Efficient Intracellular Delivery Mediated by Nano-Corrugated Mushroom-Shaped Gold-Coated Polystyrene Nanoparticles. Nanoscale 2020, 12, 12057–12067.

9. Scaffardi, L.B.; Schinca, D.C.; Lester, M.; Videla, F.A.; Santillan, J.M.J.; Abraham Ekeroth, R.M. Size-Dependent Optical Properties of Metallic Nanostructures. In UV-VIS and Photoluminescence Spectroscopy for Nanomaterials Characterization; Springer: Berlin/Heidelberg, Germany, 2013; pp. 179–229.

10. Hua, Y.; Chandra, K.; Dam, D.H.M.; Wiederrecht, G.P.; Odom, T.W. Shape-Dependent Nonlinear Optical Properties of Anisotropic Gold Nanoparticles. J. Phys. Chem. Lett. 2015, 6, 4904–4908.

11. Urbieta, M.; Barbry, M.; Zhang, Y.; Koval, P.; Sánchez-Portal, D.; Zabala, N.; Aizpurua, J. Atomic-Scale Lightning Rod Effect in Plasmonic Picocavities: A Classical View to a Quantum Effect. ACS Nano 2018, 12, 585–595.

12. Liu, Y.; Ashton, J.R.; Moding, E.J.; Yuan, H.; Register, J.K.; Fales, A.M.; Choi, J.; Whitley, M.J.; Zhao, X.; Qi, Y.; et al. A Plasmonic Gold Nanostar Theranostic Probe for in Vivo Tumor Imaging and Photothermal Therapy. Theranostics 2015, 5, 946–960.

13. Vo-Dinh, T.; Liu, Y.; Crawford, B.M.; Wang, H.-N.; Yuan, H.; Register, J.K.; Khoury, C.G. Shining gold nanostars: From cancer diagnostics to photothermal treatment and immunotherapy. J. Immunol. Sci. 2018, 2, 1–8.

14. Yuan, H.; Khoury, C.G.; Wilson, C.M.; Grant, G.A.; Bennett, A.J.; Vo-Dinh, T. In Vivo Particle Tracking and Photothermal Ablation Using Plasmon-Resonant Gold Nanostars. Nanomedicine 2012, 8, 1355–1363.

15. Dondapati, S.K.; Sau, T.K.; Hrelescu, C.; Klar, T.A.; Stefani, F.D.; Feldmann, J. Label-Free Biosensing Based on Single Gold Nanostars as Plasmonic Transducers. ACS Nano 2010, 4, 6318–6322.

16. Fales, A.M.; Yuan, H.; Vo-Dinh, T. Silica-Coated Gold Nanostars for Combined Surface-Enhanced Raman Scattering (SERS) Detection and Singlet-Oxygen Generation: A Potential Nanoplatform for Theranostics. Langmuir 2011, 27, 12186–12190.

17. Zhang, Y.; Newton, B.; Lewis, E.; Fu, P.P.; Kafoury, R.; Ray, P.C.; Yu, H. Cytotoxicity of Organic Surface Coating Agents Used for Nanoparticles Synthesis and Stability. Toxicology In Vitro 2015, 29, 762–768.

18. Taha, S.; Mohamed, W.R.; Elhemely, M.A.; El-Gendy, A.O.; Mohamed, T. Tunable Femtosecond Laser Suppresses the Proliferation of Breast Cancer in Vitro. J. Photochem. Photobiol. B. 2023, 240, 112665.

19. Zhao, X.; Tang, W.; Wang, H.; He, H. Femtosecond-Laser Stimulation Induces Senescence of Tumor Cells in Vitro and in Vivo. Biomed. Opt. Express 2022, 13, 791.

20. Li, X.; Lovell, J.F.; Yoon, J.; Chen, X. Clinical Development and Potential of Photothermal and Photodynamic Therapies for Cancer. Nat. Rev. Clin. Oncol. 2020, 17, 657–674.

21. Huang, X.; El-Sayed, M.A. Plasmonic Photo-Thermal Therapy (PPTT). Alex. J. Med. 2011, 47, 1–9.

22. Chatterjee, H.; Rahman, D.S.; Sengupta, M.; Ghosh, S.K. Gold Nanostars in Plasmonic Photothermal Therapy: The Role of Tip Heads in the Thermoplasmonic Landscape. J. Phys. Chem. C 2018, 122, 13082–13094.

23. Liu, X.; Zhou, W.; Wang, T.; Miao, S.; Lan, S.; Wei, Z.; Meng, Z.; Dai, Q.; Fan, H. Highly Localized, Efficient, and Rapid Photothermal Therapy Using Gold Nanobipyramids for Liver Cancer Cells Triggered by Femtosecond Laser. Sci. Rep. 2023, 13, 3372.

24. Kharey, P.; Goel, M.; Husain, Z.; Gupta, R.; Sharma, D.; Manikandan, M.; Palani, I.A.; Gupta, S. Green Synthesis of Biocompatible Superparamagnetic Iron Oxide-Gold Composite Nanoparticles for Magnetic Resonance Imaging, Hyperthermia and Photothermal Therapeutic Applications. Mater. Chem. Phys. 2023, 293, 126859.

25. Shinde, A.; Shinde, P.; Kar, S.; Illath, K.; Dey, S.; Mahapatra, N.R.; Nagai, M.; Santra, T.S. Metallic Micro-Ring Device for Highly Efficient Large Cargo Delivery in Mammalian Cells Using Infrared Light Pulses. Lab. Chip 2023, 23, 2175-2192.

26. Li, Y.; Wang, X.; Gao, L.; Hu, P.; Jiang, L.; Ren, T.; Fu, R.; Yang, D.; Jiang, X. Aptamer-Conjugated Gold Nanostars for Targeted Cancer Photothermal Therapy. J. Mater. Sci. 2018, 53, 14138–14148.

27. Raghavan, V.; O'Flatharta, C.; Dwyer, R.; Breathnach, A.; Zafar, H.; Dockery, P.; Wheatley, A.; Keogh, I.; Leahy, M.; Olivo, M. Dual Plasmonic Gold Nanostars for Photoacoustic Imaging and Photothermal Therapy. Nanomedicine 2017, 12, 457–471.

28. Gao, J.; Sanchez-Purra, M.; Huang, H.; Wang, S.; Chen, Y.; Yu, X.; Luo, Q.; Hamad-Schifferli, K.; Liu, S. Synthesis of Different-Sized Gold Nanostars for Raman Bioimaging and Photothermal Therapy in Cancer Nanotheranostics. Sci. China Chem. 2017, 60, 1219–1229.

29. Wang, S.; Huang, P.; Nie, L.; Xing, R.; Liu, D.; Wang, Z.; Lin, J.; Chen, S.; Niu, G.; Lu, G.; et al. Single Continuous Wave Laser Induced Photodynamic/Plasmonic Photothermal Therapy Using Photosensitizer-Functionalized Gold Nanostars. Adv. Mater. 2013, 25, 3055–3061.

30. Sasidharan, S.; Bahadur, D.; Srivastava, R. Rapid, One-Pot, Protein-Mediated Green Synthesis of Gold Nanostars for Computed Tomographic Imaging and Photothermal Therapy of Cancer. ACS Sustain. Chem. Eng. 2017, 5, 10163–10175.

31. Mahmoodzadeh, F.; Abbasian, M.; Jaymand, M.; Salehi, R.; Bagherzadeh-Khajehmarjan, E. A Novel Gold-Based Stimuli-Responsive Theranostic Nanomedicine for Chemo-Photothermal Therapy of Solid Tumors. Mater. Sci. Eng. C 2018, 93, 880–889.

32. Zharov, V.P.; Galitovsky, V.; Viegas, M. Photothermal Detection of Local Thermal Effects during Selective Nanophotothermolysis. Appl. Phys. Lett. 2003, 83, 4897–4899.

33. Demille, T.B.; Hughes, R.A.; Dominique, N.; Olson, J.E.; Rouvimov, S.; Camden, J.P.; Neretina, S. Large-Area Periodic Arrays of Gold Nanostars Derived from HEPES-, DMF-, and Ascorbic-Acid-Driven Syntheses. Nanoscale 2020, 12, 16489–16500.

34. Maiorano, G.; Rizzello, L.; Malvindi, M.A.; Shankar, S.S.; Martiradonna, L.; Falqui, A.; Cingolani, R.; Pompa, P.P. Monodispersed and Size-Controlled Multibranched Gold Nanoparticles with Nanoscale Tuning of Surface Morphology. Nanoscale 2011, 3, 2227–2232.

35. Radue, E.L.; Tomko, J.A.; Giri, A.; Braun, J.L.; Zhou, X.; Prezhdo, O.V.; Runnerstrom, E.L.; Maria, J.P.; Hopkins, P.E. Hot Electron Thermoreflectance Coefficient of Gold during Electron-Phonon Nonequilibrium. ACS Photonics 2018, 5, 4880–4887.

36. Wang, S.H.; Lee, C.W.; Chiou, A.; Wei, P.K. Size-Dependent Endocytosis of Gold Nanoparticles Studied by Three-Dimensional Mapping of Plasmonic Scattering Images. J. Nanobiotechnology 2010, 8, 1–13.

37. Kalies, S.; Keil, S.; Sender, S.; Hammer, S.C.; Antonopoulos, G.C.; Schomaker, M.; Ripken, T.; Escobar, H.M.; Meyer, H.; Heinemann, D. Characterization of the Cellular Response Triggered by Gold Nanoparticle–Mediated Laser Manipulation. J. Biomed. Opt. 2015, 20, 115005.

38. Sengupta, A.; Kelly, S.C.; Dwivedi, N.; Thadhani, N.; Prausnitz, M.R. Efficient Intracellular Delivery of Molecules with High Cell Viability Using Nanosecond-Pulsed Laser-Activated Carbon Nanoparticles. ACS Nano 2014, 8, 2889–2899.

39. Azadgoli, B.; Baker, R.Y. Laser Applications in Surgery. Ann. Transl. Med. 2016, 4. Dierickx, C.C.; Anderson, R.R. Visible Light Treatment of Photoaging. Dermatol. Ther. 2005, 18, 191–208.

40. Nehl, C.L.; Hafner, J.H. Shape-Dependent Plasmon Resonances of Gold Nanoparticles. J. Mater. Chem. 2008, 18, 2415–2419.

41. Shafiqa, A.R.; Abdul Aziz, A.; Mehrdel, B. Nanoparticle Optical Properties: Size Dependence of a Single Gold Spherical Nanoparticle. Proc. J. Phys. Conf. Ser. 2018, 1083, 012040.

42. Munafò, A.; Alberti, A.; Pantano, C.; Freund, J.B.; Panesi, M. A Computational Model for Nanosecond Pulse Laser-Plasma Interactions. J. Comput. Phys. 2020, 406, 109190.

43. Lukianova-Hleb, E.; Hu, Y.; Latterini, L.; Tarpani, L.; Lee, S.; Drezek, R.A.; Hafner, J.H.; Lapotko, D.O. Plasmonic Nanobubbles as Transient Vapor Nanobubbles Generated around Plasmonic Nanoparticles. ACS Nano 2010, 4, 2109–2123.

44. Lombard, J.; Biben, T.; Merabia, S. Threshold for Vapor Nanobubble Generation Around Plasmonic Nanoparticles. J. Phys. Chem. C 2017, 121, 15402–15415.

45. Shinde, P.; Kar, S.; Loganathan, M.; Chang, H.Y.; Tseng, F.G.; Nagai, M.; Santra, T.S. Infrared Pulse Laser-Activated Highly Efficient Intracellular Delivery Using Titanium Microdish Device. ACS Biomater. Sci. Eng. 2020, 6, 5645–5652.

46. Weiss, J.; Garnon, J.; Dalili, D.; Cazzato, R.L.; Koch, G.; Auloge, P.; Gangi, A. The Feasibility of Combined Microwave Ablation and Irreversible Electroporation for Central Liver Metastases. Cardiovasc. Intervent Radiol. 2021, 44, 999–1001.

47. Canatella, P.J.; Karr, J.F.; Petros, J.A.; Prausnitz, M.R. Quantitative Study of Electroporation-Mediated Molecular Uptake and Cell Viability. Biophys. J. 2001, 80, 755–764.

48. Mohan, L.; Kar, S.; Nagai, M.; Santra, T.S. Electrochemical Fabrication of TiO2 Micro-Flowers for an Efficient Intracellular Delivery Using Nanosecond Light Pulse. Mater. Chem. Phys. 2021, 267, 124604.

49. Boulais, E.; Lachaine, R.; Hatef, A.; Meunier, M. Plasmonics for Pulsed-Laser Cell Nanosurgery: Fundamentals and Applications. J. Photochem. Photobiol. C Photochem. Rev. 2013, 17, 26–49.

50. Hatef, A.; Meunier, M. Plasma-Mediated Photothermal Effects in Ultrafast Laser Irradiation of Gold Nanoparticle Dimers in Water. Opt. Express 2015, 23, 1967.

51. Urban, A.S.; Fedoruk, M.; Horton, M.R.; Rädler, J.O.; Stefani, F.D.; Feldmann, J. Controlled Nanometric Phase Transitions of Phospholipid Membranes by Plasmonic Heating of Single Gold Nanoparticles. Nano Lett. 2009, 9, 2903–2908.

52. Vogl, T.J.; Straub, R.; Eichler, K.; Söllner, O.; Mack, M.G. Colorectal Carcinoma Metastases in Liver: Laser-Induced Interstitial Thermotherapy—Local Tumor Control Rate and Survival Data. Radiology 2004, 230, 450–458.

Chapter 5: Cell Perforation with Prussian Blue Nanocube Cluster for Intracellular Delivery and Cell Patterning

5.1 Introduction

As described earlier, intracellular delivery and photothermal therapy have been successfully demonstrated using various photoabsorber-based approaches, particularly micropattern-assisted methods [1–3] and gold nanoparticle (AuNP)-based systems [4–16]. These strategies have shown considerable promise in biomedical fields such as regenerative medicine, cell therapy, and oncological phototherapy, primarily due to their ability to enable localized, efficient, and minimally invasive cellular manipulation. For example, micropatterns enable site-specific delivery by precisely defining irradiation zones, while gold nanoparticles, with their strong surface plasmon resonance properties, are widely utilized for effective light-to-heat conversion during laser treatment.

However, despite their functional success in experimental and preclinical models, the widespread adoption and commercialization of these technologies face significant obstacles. A major bottleneck lies in the high cost and technical complexity associated with the fabrication of micropatterned substrates. Producing reproducible and high-resolution micropatterns often involves sophisticated microfabrication techniques (e.g., photolithography, reactive ion etching), cleanroom facilities, and expensive raw materials, all of which limit scalability and raise production costs.

Similarly, while gold nanoparticles are effective photothermal agents, the high market price of gold poses a substantial economic barrier. Furthermore, the batch-to-batch variability, surface chemistry control, and potential long-term toxicity of gold nanoparticles remain critical concerns for clinical translation. Regulatory approval for therapeutic systems involving noble metals is also stringent, making commercialization even more challenging.

Prussian Blue nanoparticles (PBNPs), historically known as low-cost inorganic dyes, have recently attracted considerable attention in the biomedical field due to their unique physicochemical properties, excellent biocompatibility, and ease of synthesis. These nanoparticles offer a cost-effective alternative to conventional materials such as gold nanoparticles, whose high price and complex surface modifications significantly limit their feasibility for large-scale biomedical applications. In contrast, PBNPs can be synthesized through simple aqueous-based protocols under ambient conditions, making them highly suitable for scalable and reproducible production.

The biocompatibility and photothermal responsiveness of Prussian Blue nanoparticles make them especially attractive for therapeutic and diagnostic applications, including photothermal therapy (PTT) and intracellular delivery [17–20]. Their photothermal nature allows efficient conversion of laser energy into localized heat, which can be harnessed for multiple purposes—such as transient pore formation on cell membranes (optoporation), localized thermal damage to malignant cells, and facilitating molecular diffusion into cytoplasm.

In this study, we report the use of Prussian Blue Nanocube Clusters (PBNCCs) as a functional and economical substitute for conventional gold nanoparticles to enable efficient intracellular delivery and cell patterning via photothermal effects. Prussian Nanocube Clusters were used instead of Prussian nanoparticles to avoid the intake of nanoparticles into cells by endocytosis. Specifically, PBNCCs were incubated with HeLa cells, followed by nanosecond pulsed laser irradiation, which induced localized heating and generated photothermal shockwaves capable of transiently disrupting the cell membrane, thereby allowing uptake of otherwise impermeable molecules like FITC-dextran (4 kDa). Fluorescence imaging analysis confirmed successful cytosolic delivery of FITC-dextran in a spatially selective manner, with high delivery efficiency and minimal cell death under optimized conditions.

In addition to intracellular delivery, we further observed that patterned irradiation of PBNCCs on a cell monolayer surface induced distinct cell patterning effects, where regions exposed to laser energy exhibited targeted cell perforation or removal, enabling the creation of precise cellular patterns. This phenomenon is attributed to the localized heat and mechanical stress produced during nanobubble collapse or rapid thermal expansion, leading to selective ablation of cells in the irradiated zones. Such spatially controlled cell manipulation has important implications for tissue engineering, *in vitro* model development, and site-specific drug delivery research.

5.2 Experimental Methods

5.2.1 Preparation of Prussian Blue Clusters

Polyethylene Glycol (PEG) was dissolved in water to create a 50% PEG aqueous solution, which was then maintained at 50°C on a hot plate. To initiate the reaction, aqueous solutions of $K_3[FeIII(CN)_6]$ and $Fe(NO_3)_3$ were added to the PEG solution under magnetic stirring. The final concentrations of $K_3[FeIII(CN)_6]$ and $Fe(NO_3)_3$ were adjusted to 0.018 mol/L and 0.024 mol/L, respectively. After that, the reacting mixture was magnetically stirred for 48 hours. Synthesized PBNCCs were collected by centrifugation at 5000 rpm and redispersed in deionized (DI) water [21]. The prepared nanocubes were dried at 500 °C for one day, and flakes were obtained. Before experiments, these flakes were suspended in DI water and sonicated for 30 minutes to obtain Prussian nanocube clusters (PBNCCs). To confirm the preparation of Prussian Blue nanocubes, the prepared particles were analyzed using SEM and UV-Vis spectroscopy.

5.2.2 Procedure for Optoporation

HeLa cells were cultured on a 35mm Petri dish in minimum essential medium at 37°C in a 5% CO2 incubator for intracellular delivery. After the cell growth overnight, PBNCCs

were incubated over the cells at a final concentration of 0.1 mM and 0.2 mM for 2 hours. The cells were washed thrice with PBS, and then FITC-Dextran (4 kDa) (1mM) was added to the Petri dish, followed by laser irradiation. The cells were incubated for 10 minutes post laser irradiation and then washed three times to remove the background fluorescence of FITC. After this, PI (4 μM) was used to assess the viability of the cells.

5.2.3 Procedure for Cell Patterning

HeLa cells were cultured on a 35 mm Petri dish in minimum essential medium at 37°C in a 5% CO2 incubator for intracellular delivery. After the cell growth overnight, PBNCCs were incubated over the cells at the desired concentration for 2 hours. After 2 hours, the cells were washed with PBS, and Calcein-AM was added to the cells. After 20 minutes of incubation, PI was added to the cells, and the cells were irradiated at the laser parameters mentioned in the later sections.

5.2.4 Data Analysis

The cells were examined with a fluorescent microscope (Ti-E, Nikon, Japan). The microscope was equipped with G2A and B2A fluorescence cubes and a camera (DS-Fi3, Nikon, Japan). Three images were examined for each experimental condition, and the multipoint tool in ImageJ was used to manually count the cells along the laser irradiation path. Delivery efficiency was calculated as the percentage of FITC dextran-loaded cells and total number of cells along the path of laser irradiation, and viability was measured by determining the percentage of total number of alive cells to total number of cells along the laser irradiation path post optoporation.

For cell patterning analysis the irradiation range of cell patterning (d) was calculated by calculating the width of irradiation in path in imageJ software for a given laser path and cell killing efficiency along the laser path calculated as the ratio of dead cells (PI stained cells) and

total number of cells (PI stained cells and Calcein-AM stained cells) along the path of laser irradiation by using multipoint tool of ImageJ to obtain the optimum parameters or cell patterning.

To pattern cells at optimized parameters, the path of laser irradiation was determined concerning irradiation width (d). The pitch of laser irradiation in the raster irradiation path was determined by adding the target width (T) of the cell pattern to the irradiation range of cell patterning (d) of the laser at the optimized parameters as described in Figure 5.1.

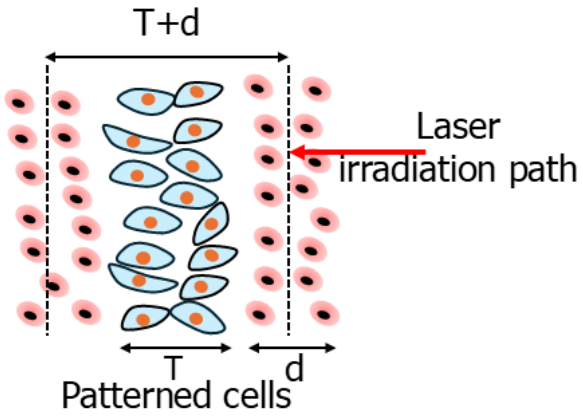

Figure 5.1 Calculation of scanning pitch of laser irradiation.

After obtaining the cells' parameters at optimized laser parameters, the width of the formed micropattern is obtained in ImageJ. For each target micropattern dimension, 5 cell patterns were analyzed and 5 measurment of width were performed for each micropattern, leading to a total of 25 measurements. The obtained values of the cell micropattern were analyzed in MS Excel software using statistics (Mean and standard deviation), and results were summarized to evaluate the accuracy and precision of formation of micropattern structures.

5.3 Result

5.3.1 Characterization of Prussian Blue Clusters

PBNCCs were characterized using scanning electron microscopy and UV vis spectroscopy analysis (Figure 5.2). SEM confirmed the successful formation of PBNCCs, revealing microclusters of around 1-2 µm (Figure 5.2(a)). Figure 5.2(a) SEM and 5(b) UV-Vis analysis of PBNCC UV/VIS spectra (Figure 5.2(b)) show the absorbance of light at the wavelength of 532 nm, but it is lower at 532 nm than the absorbance in the UV and NIR range. PBNCCs act as interfaces for light-to-thermal energy conversion, differing from the conventional optopotiation. To make up for that laser parameters were accordingly optimized. PBNCCs amplify the dispersed near field instead of greatly absorbing photon energy, which causes a highly localized electronic plasma and bubbles (optical breakdown) in cell culture medium that cause intracellular delivery.

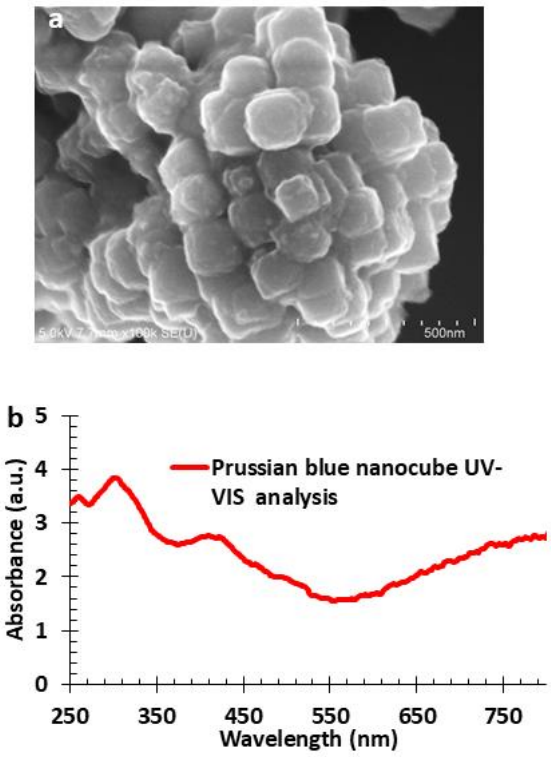

Figure 5.2 Characterization of PBNCCs. (a) SEM. (b) UV-Vis analysis of PBNCCs.

5.3.2 Results of Optoporation with Prussian Blue Clusters

The intracellular delivery into cells critically depends on various factors such as Laser fluence, photosensitizer concentration, scanning velocity, and repetition rate of the laser. In the experiments, we kept the stage velocity and repetition rate constant at 100 mm/s and 1kHz. We tried to optimize the delivery efficiency by first varying the laser fluence at a constant concentration of the PBNCCs.

Figure 5.3 represents intracellular delivery and cell viability analysis of FITC-Dextran (4 kDa) delivery into the HeLa cells along the path of laser Irradiation for the sample with 0.1 mM PBNCCs. Figure 5.3(a) and (c) depict the HeLa cells showing green fluorescence, confirming intracellular uptake of fluorescent cargo material. Delivery efficiency was around 35% (29 cells/500μm) for the laser fluence of 5.78 mJ/cm^2. Cell viability in our chosen range of laser fluences was around 100% for all chosen values of laser fluences.

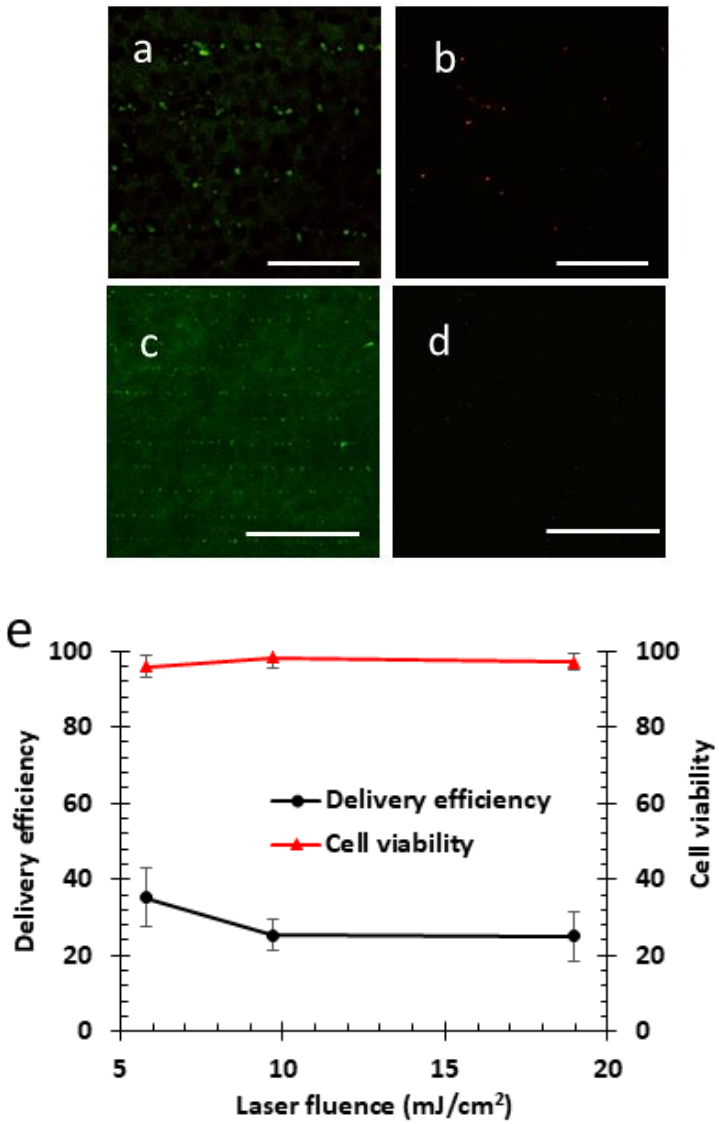

Figure 5.3 Optoporated HeLa cells at 18.97 mJ/cm^2 with 0.1 mM of PBNCCs. (a-b) Intracellular delivery and cell death at lower magnification. Scale bars are 250 µm. (c-d) Intracellular delivery and cell death at higher magnification. Scale bars are 500 µm. (e) Delivery efficiency and cell viability post optoporation.

We further increased the PBNCCs concentration to 0.2M. Figure 4 represents the dye-loaded cells, dead cells, and analysis of delivery efficiency and cell viability post optoporation along the laser irradiation path. Increasing the PBNCC concentration boosted delivery efficiency, reaching a peak of 63% (28cells/500µm) at 18.97 mJ/cm^2 while maintaining

minimal cell death (Figure 5.4(b)). We observed an increase in delivery efficiency upon increasing the laser fluence at this particular concentration of PBNCCs (Figure 5.4(e)). The experimental results indicate that further optimization of the experimental parameters can further increase the delivery efficiency.

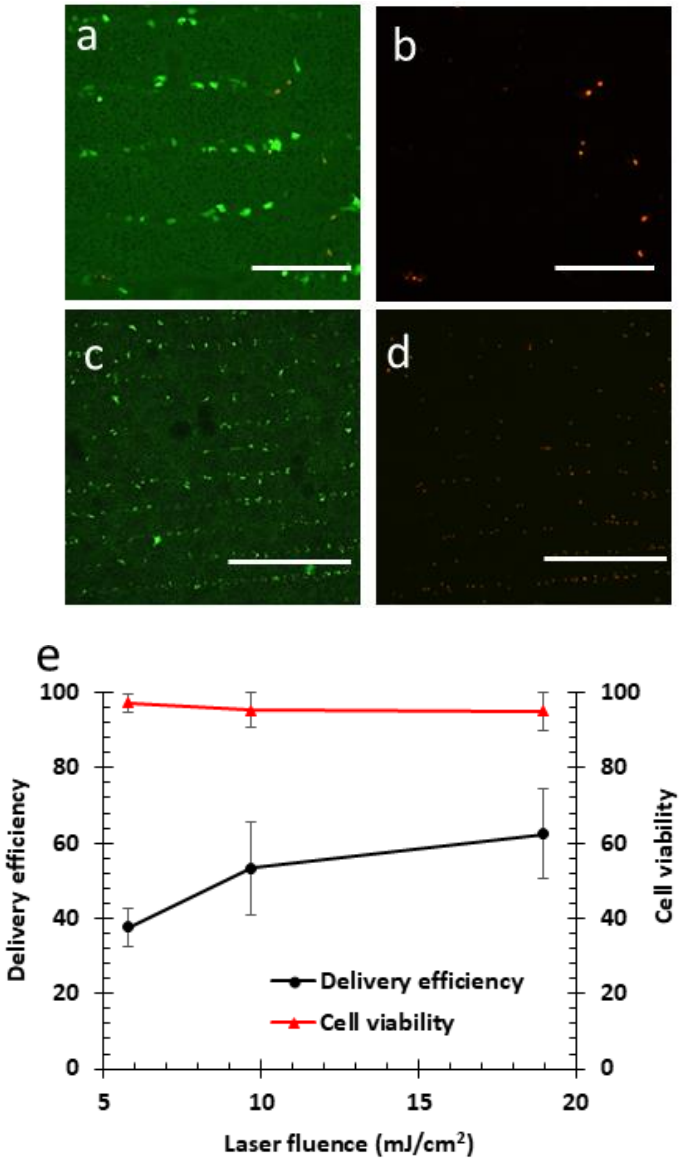

Figure 5.4 Optoporated HeLa cells at 18.97 mJ/cm^2 with 0.2 mM of PBNCCs. (a-b) Intracellular delivery and cell death at lower magnification. Scale bars are 250 µm. (c-d) Intracellular delivery and cell death at higher magnification. Scale bars are 500 µm. (e). Delivery efficiency and cell viability post optoporation.

Laser fluence and nanoparticle concentration are the key factors controlling optoporation, and maximum optimization would result in minimum invasiveness. On increasing both these parameters, the conversion of light to thermal energy increases, which heats the cell culture medium in the vicinity. Heating of cell culture medium results in the formation of vapor bubbles, which eventually collapse and cause a shockwave in the vicinity. The magnitude of this shockwave plays an important role in the optoporation process. Because if the magnitude of the shock wave is less, the cells will remain unaffected; on the other hand, if the magnitude of the shockwave is more than required, the cells will peel off from the petri dish, or cell death might be triggered due to disability to reseal the transient pores on the cell membrane.

Upon investigating the number of cells along the laser irradiation path post optoporation, cell count (per 500 µm along the laser irradiation path) revealed a lower average cell number at 18.97 mJ/cm² with 0.2 mM PBNCCs compared to the lower concentration (Figure 5.5). This observation warrants further investigation and indicates that further optimization of parameters might be required.

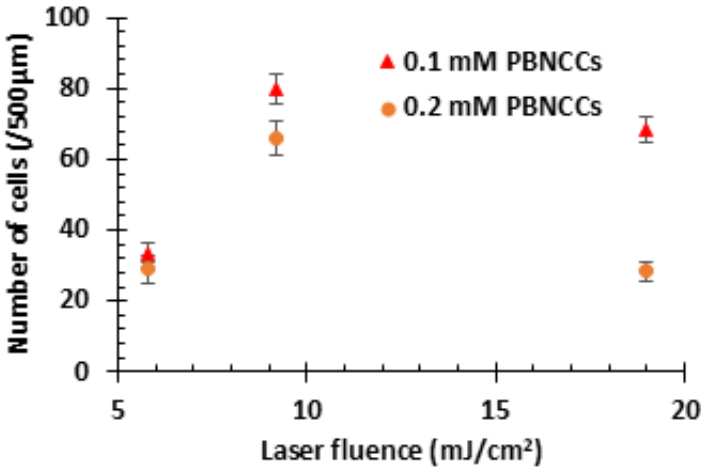

Figure 5.5 Cell count along the laser irradiation path post optoporation.

5.3.3 Optimization of Cell Patterning Parameters

Firstly, we investigated the use of PBNCCs in combination with laser irradiation for achieving spatially controlled cell patterning. Specifically, we aimed to determine the optimal experimental parameters—namely, nanoparticle concentration, laser fluence, and stage velocity—that result in maximum cell elimination efficiency and clearly defined irradiation range along the laser path. These three parameters are critical to ensuring effective patterning with minimal off-target effects in biomedical applications such as photothermal therapy or spatially resolved cell elimination.

To begin with, we optimized the concentration of PBNCCs incubated with the cells. Cells were treated with three different concentrations: 0.1 mM, 0.2 mM, and 0.5 mM. Upon exposure to laser irradiation under identical fluence, both the irradiation range (d) and cell elimination efficiency showed a positive correlation with nanoparticle concentration (Figure 5.6). Fluorescence microscopy images revealed increasingly distinct laser tracks with rising concentrations of PBNCCs. Quantitative analysis showed that the irradiation range (d)—measured as the width of the laser-affected zone—increased from 89.2±14.2 μm at 0.1 mM to 128±14.4 μm at 0.5 mM. Concurrently, the cell elimination efficiency increased from 11.8±2.8 at the lowest concentration to 76.38±3.3 at 0.5mM. These results suggest that a higher density of nanoparticles enhances local photothermal conversion, thereby expanding the laser's effective range and increasing the extent of cell damage within the irradiation path.

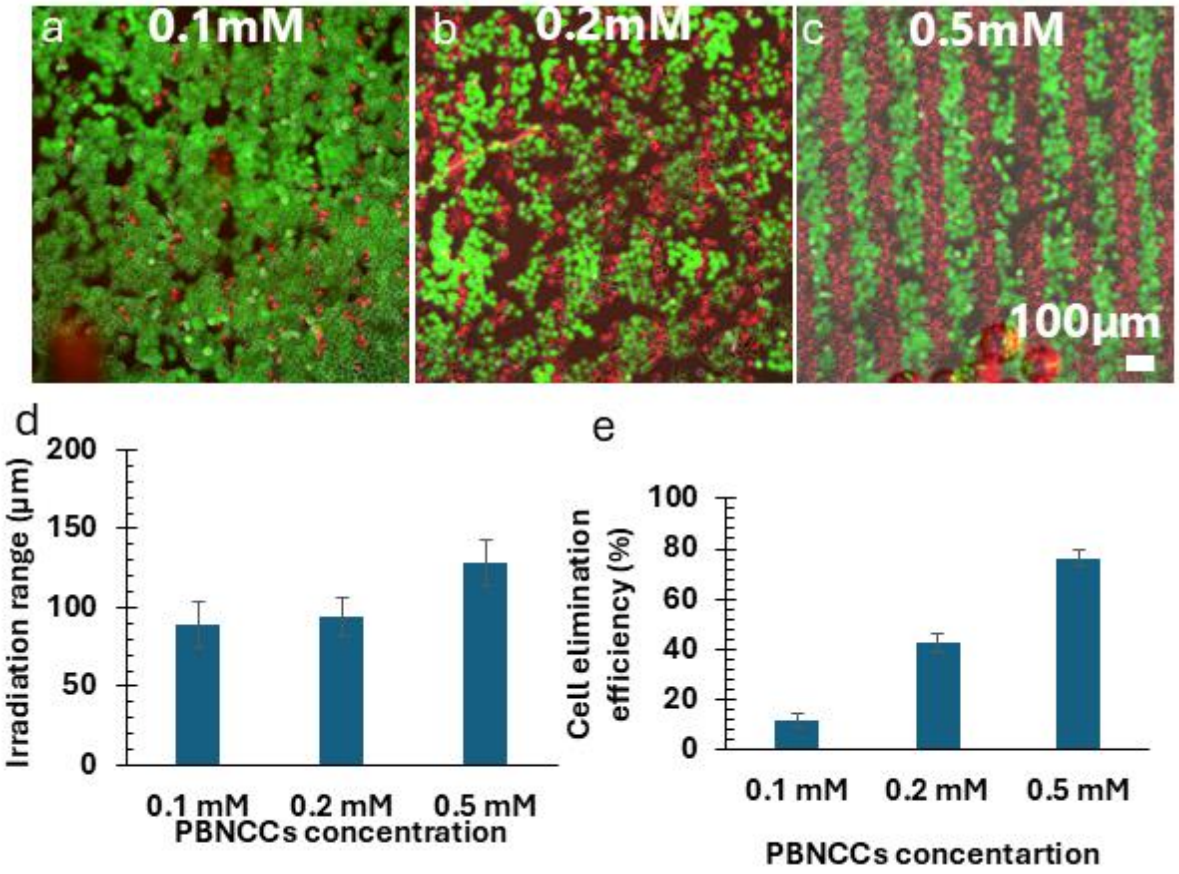

Figure 5.6 Optimizing of PBNCCs concentration for cell patterning. Obtained patterns at PBNCCs concentration (a) 0.1 mM. (b) 0.2 mM. (c) 0.5 mM. (d) Irradiation range of cell patterning at various concentrations. (e) Cell elimination efficiency along laser path of irradiation at various concentrations.

Next, we investigated the effect of laser fluence while keeping the nanoparticle concentration constant. Laser fluences of 126 mJ/cm², 200 mJ/cm², and 514 mJ/cm² were tested. As anticipated, both the irradiation range and the efficiency of cell killing increased with laser energy. The laser tracks became more continuous and intense at higher fluences, indicating stronger photothermal effects (Figure 5.7). Quantitative analysis showed a steady rise in irradiation range (d) from 80±9.1 µm at 126 mJ/cm² to 128±14.4 µm at 514 mJ/cm². Similarly, cell elimination efficiency increased from 28.76±4.2 to approximately 76.38±3.3 across the

same fluence range. These observations confirm that higher fluence levels deliver more energy to the nanoparticle-cell interface, leading to greater heat generation, which in turn enhances cellular ablation.

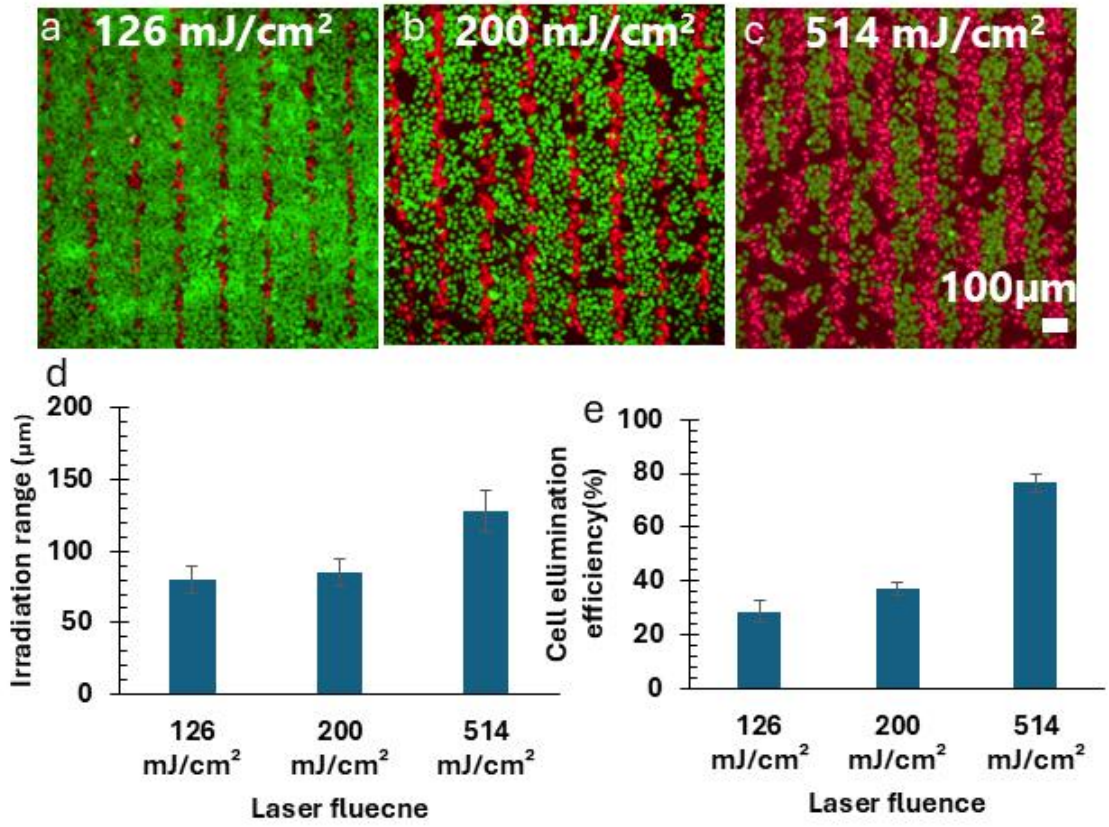

Figure 5.7 Optimizing laser fluence for cell patterning. Obtained patterns at laser fluence (a) 126mJ/cm^2. (b) 200 mJ/cm^2. (c) 514 mJ/cm^2. (d) Irradiation range of cell patterning at various laser fluences. (e) Cell elimination efficiency along the laser path of irradiation at various laser fluences.

Fluorescence microscopy images Figure 5.8 (a–c) show laser-irradiated cell monolayers treated with Prussian Blue nanoparticles at 0.5 mM and exposed to a laser fluence of 514 mJ/cm², while varying the stage scan velocity. The stage velocities used were 10 mm/s (a), 100 mm/s (b), and 200 mm/s (c). The irradiated paths appear in red (damaged/dead cells), while viable cells are stained green.

At the lowest stage velocity of 10 mm/s (a), the laser path appears well-defined and intense, with significant cellular damage evident along the irradiated lines. The slower scan allows more laser pulses to be delivered per unit length, resulting in strong photothermal effects and consistent cell death across the pattern. As the velocity increases to 100 mm/s (b), the laser tracks begin to show signs of irregularity. Though the pattern remains largely visible, some fluctuation in the straightness of the lines is observed. This is attributed to increased mechanical vibration of the motorized stage at intermediate speed, which compromises path accuracy. Additionally, fewer laser pulses are deposited per unit area, leading to slightly reduced cell killing efficiency and a smaller irradiation range. At the highest velocity of 200 mm/s (c), the degradation in pattern quality becomes more pronounced. The tracks appear discontinuous and curved, a result of compounded stage vibration and insufficient laser dwell time. Consequently, laser energy delivery becomes sparse, and the photothermal effect is not strong enough to consistently eliminate cells along the path. This leads to a significant drop in cell death efficiency.

In summary, these images demonstrate that higher stage velocities reduce the spatial precision of laser irradiation and compromise cell ablation efficiency, primarily due to mechanical instability and a lower number of effective laser pulses per unit length.

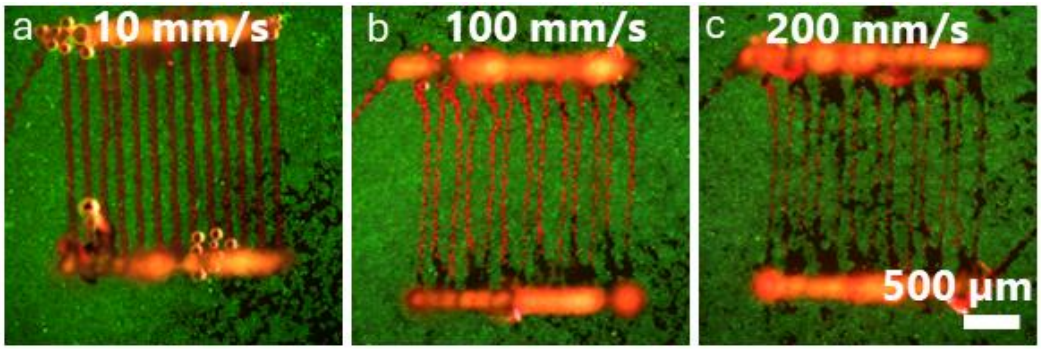

Figure 5.8 Optimizing stage velocity for cell patterning (a) 10 mm/s, (b) 100 mm/s, (c) 200 mm/s.

Taken together, the results from both optimization experiments indicate that the combination of 0.5 mM PBNCCs concentration with 514 mJ/cm² laser fluence at 10mm/s velocity produces the most effective outcome for cell patterning. This condition results in the widest irradiation path and the highest cell elimination efficiency. Therefore, these parameters were identified as the optimal setting for applications requiring precise and efficient patterned cell ablation.

5.3.4 Cell Patterning with Optimized Parameters

Figure 5.9 shows the distribution of measured pattern dimensions for target sizes (T) of 100 μm, 150 μm, 200 μm, 250 μm, and 300 μm, with 25 measurements per group. The red dashed lines indicate the respective target sizes. This analysis evaluates the performance of cell patterning under optimized laser and nanoparticle conditions in terms of dimensional accuracy (closeness to target) and precision (consistency across replicates).

The descriptive statistics indicate that the actual diameters of the laser-formed micropatterns consistently undershoot the target diameters across all groups. For the 100 μm target, the mean diameter is 89.5 μm, showing a deviation of −10.4 μm, while for the 150 μm target, the mean is 141.5 μm, indicating a −8.4 μm error. The 200 μm and 250 μm patterns show larger deviations of −15.4 μm and −14.2 μm, with mean values of 184.5 μm and 235.7 μm, respectively. The 300 μm group has a mean of 291.4 μm, resulting in a −8.5 μm deviation.

In terms of precision, which is reflected by the standard deviation, the 100 μm patterns exhibit the highest precision, with a standard deviation of 7.0 μm. The 150 μm and 300 μm groups show lower precision, with standard deviations of 14.9 μm and 17.2 μm, respectively, indicating greater variability in pattern formation. The 200 μm and 250 μm groups display moderate precision, with standard deviations of 11.1 μm and 13.6 μm, respectively. The reason

for the precision not following a strict trend might be due to the variability of cell distribution in the petri dish, which results in different widths of formed micropatterns.

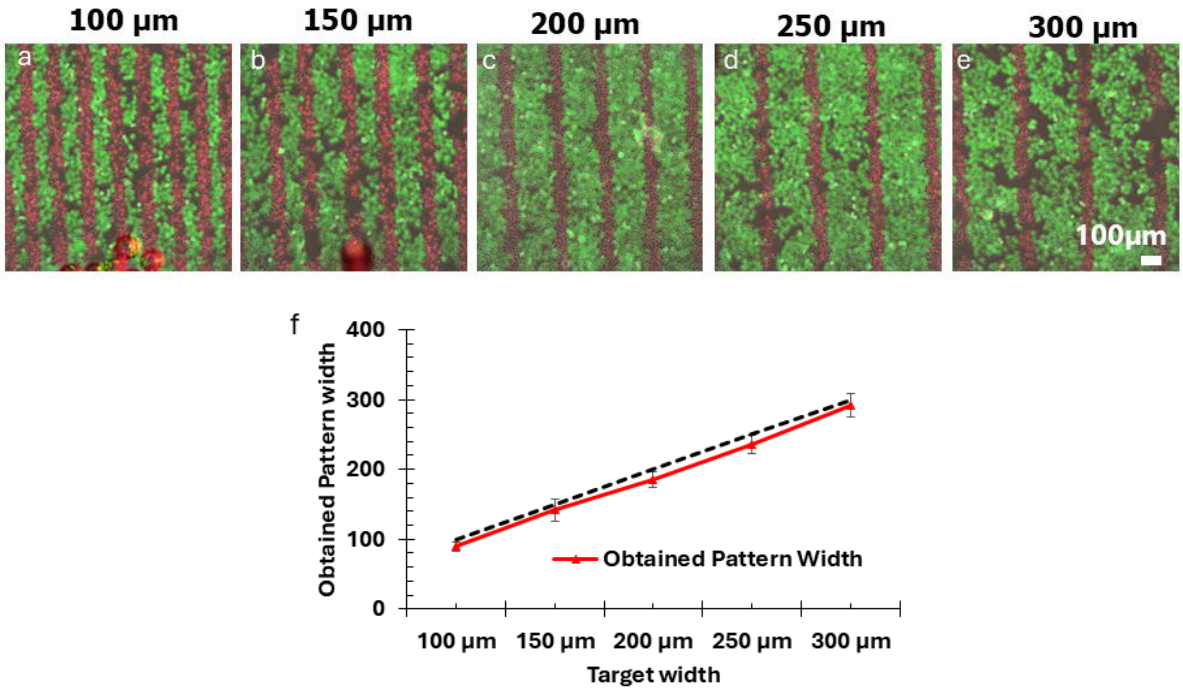

Figure 5.9 Cell patterning for target pattern width (a) 100 µm. (b) 150 µm. (c) 200 µm. (d) 250 µm. (e) 300 µm. (f) Obtained pattern width.

5.4 Discussion

Like gold nanoparticles, the mechanism by which Prussian Blue Nanoclusters (PBNCCs) facilitate intracellular delivery involves the absorption of laser energy and its rapid conversion into localized heat. Upon laser irradiation (Figure 5.10(a)), the intense and highly localized heating around the PBNCCs leads to the formation of vapor nanobubbles within the surrounding aqueous cellular environment (Figure 5.10(b)). These vapor nanobubbles rapidly expand and eventually collapse, producing a strong, localized shockwave. The mechanical forces generated during this expansion-collapse cycle induce transient disruptions in the cell membrane, a process known as membrane permeabilization (Figure 5.10(c)). These transient pores allow therapeutic molecules or other cargo present in the extracellular medium to enter the cytoplasm without causing permanent cell damage. This mechanism provides a highly

spatially selective, minimally invasive, and controllable approach for intracellular delivery, making PBNCC-assisted laser optoporation a promising alternative to traditional physical or chemical delivery techniques. Similarly, if sufficiently high laser fluence is provided where the nature of pores is permanent instead of transient, the process results in the death of cells, which is utilized in the patterning of cells.

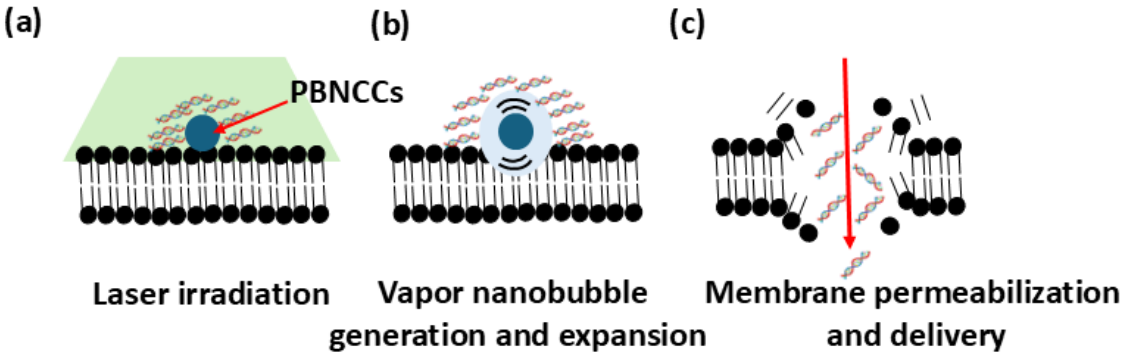

Figure 5.10 Mechanism of membrane permeabilization with Prussian Blue nanoclusters.

Compared with the PR-254/SU-8 micropattern platform and gold nanostars (GNS), Prussian Blue nanocube clusters (PBNCCs) sit in a pragmatic middle ground. Micropatterns excel in built-in registration and parallelism—cells are processed in well-defined sites with high spatial fidelity and easy visual targeting—yet they demand lithography, are less flexible for arbitrary targeting, and typically require higher fluence because the absorber is non-metallic. GNS deliver the lowest fluence thresholds and crisp, site-specific ablation thanks to strong plasmonic absorption, but they are costly, can aggregate, often need surface functionalization, and raise persistence/toxicity and regulatory concerns; distributing them uniformly without off-target uptake also complicates high-throughput use. PBNCCs avoid microfabrication and precious metals, are inexpensive and scalable, and enable dual-mode operation (transient delivery or permanent ablation) with the same 532-nm, ns-pulse setup; however, their perforation window is more parameter-sensitive, outcomes depend on particle

concentration/clustering and local distribution, and pattern fidelity can suffer if coverage is uneven. In short, micropatterns support throughput and reproducibility but are fabrication-bound; while GNS has maximal efficiency but high cost and complexity; and PBNCCs have low-cost versatility with lower light to heat conversion.

5.5 Conclusion

In this study, we demonstrated the feasibility of using Prussian Blue Nanocube Clusters (PBNCCs) as a photosensitizing agent for laser-assisted intracellular delivery and cell patterning in HeLa cells. By systematically optimizing key experimental parameters such as laser fluence, nanoparticle concentration, and stage velocity, we achieved high intracellular delivery efficiency of FITC-dextran with minimal loss of cell viability. At optimal conditions (0.2 mM PBNCCs and 18.97 mJ/cm² laser fluence), a delivery efficiency of up to 63% was obtained while maintaining low cytotoxicity.

In addition to delivery, we explored PBNCC-assisted laser cell patterning. We observed that increasing nanoparticle concentration and laser fluence significantly enhanced both the irradiation range and cell elimination efficiency. Notably, the combination of 0.5 mM PBNCCs with 514 mJ/cm² laser fluence and 10 μm/s scan velocity resulted in the highest ablation performance with well-defined laser tracks. Precision and reproducibility were further validated through dimensional analysis of patterned regions.

Overall, our findings highlight the dual functionality of PBNCCs in enabling both efficient intracellular delivery and spatially controlled cell ablation. Future work will focus on fine-tuning these parameters to improve delivery yield while minimizing invasiveness and optimizing pattern resolution for advanced biofabrication and therapeutic applications. Altogether, these results establish Prussian Blue nanoparticles—particularly in the form of nanocube clusters—as a versatile, biocompatible, and low-cost photoabsorber platform for enabling high-throughput intracellular delivery and patterned cell processing via photothermal

optoporation. Their ease of synthesis and proven biosafety further support their potential for translational research and future clinical applications.

References

1. Shinde, A.; Shinde, P.; Kar, S.; Illath, K.; Dey, S.; Mahapatra, N.R.; Nagai, M.; Santra, T.S. Metallic Micro-Ring Device for Highly Efficient Large Cargo Delivery in Mammalian Cells Using Infrared Light Pulses. Lab Chip 2023, 23, 2175, 2192.
2. Mishra, A.; Okamoto, S.; Shibata, T.; Nagai, .M, PR-254 Micropattern Assisted Optoporation of Mammalian Cells Using Light Pulses. MAG 電気学会研究会資料. 2023; 114-13, 39-42.
3. Shinde, P.; Kar, S.; Loganathan, M.; Chang, H.Y.; Tseng, F.G.; Nagai, M.; Santra, T.S. Infrared Pulse Laser-Activated Highly Efficient Intracellular Delivery Using Titanium Microdish Device. ACS Biomater Sci Eng 2020, 6, 5645–5652.
4. Mahmoodzadeh, F.; Abbasian, M.; Jaymand, M.; Salehi, R.; Bagherzadeh-Khajehmarjan, E. A Novel Gold-Based Stimuli-Responsive Theranostic Nanomedicine for Chemo-Photothermal Therapy of Solid Tumors. Mater Sci Eng C Mater Biol Appl 2018, 93, 880–889.
5. Pornnoppadol, G.; Cho, S.; Yu, J.H.; Kim, S.H.; Nam, Y.S. Cancer-Targeting Gold-Decorated Melanin Nanoparticles for in Vivo near-Infrared Photothermal Therapy. Mol Syst Des Eng 2024, 9, 507–517.
6. Hasan, M.; Bethell, D.; Brust, M. The Fate of Sulfur-Bound Hydrogen on Formation of Self-Assembled Thiol Monolayers on Gold: 1H NMR Spectroscopic Evidence from Solutions of Gold Clusters. J Am Chem Soc 2002, 124, 1132–1133.
7. Santra, T.S.; Kar, S.; Chen, T.C.; Chen, C.W.; Borana, J.; Lee, M.C.; Tseng, F.G. Near-Infrared Nanosecond-Pulsed Laser-Activated Highly Efficient Intracellular Delivery Mediated by Nano-Corrugated Mushroom-Shaped Gold-Coated Polystyrene Nanoparticles. Nanoscale 2020, 12, 12057–12067.
8. Huang, X.; Jain, P.K.; El-Sayed, I.H.; El-Sayed, M.A. Plasmonic Photothermal Therapy (PPTT) Using Gold Nanoparticles. Lasers Med Sci 2008, 23, 217–228.
9. Bansal, S.A.; Kumar, V.; Karimi, J.; Singh, A.P.; Kumar, S. Role of Gold Nanoparticles in Advanced Biomedical Applications. Nanoscale Adv 2020, 2, 3764–3787.
10. Raghavan, V.; O'Flatharta, C.; Dwyer, R.; Breathnach, A.; Zafar, H.; Dockery, P.; Wheatley, A.; Keogh, I.; Leahy, M.; Olivo, M. Dual Plasmonic Gold Nanostars for Photoacoustic Imaging and Photothermal Therapy. Nanomedicine 2017, 12, 457–471.
11. Kalies, S.; Keil, S.; Sender, S.; Hammer, S.C.; Antonopoulos, G.C.; Schomaker, M.; Ripken, T.; Escobar, H.M.; Meyer, H.; Heinemann, D. Characterization of the Cellular Response Triggered by Gold Nanoparticle–Mediated Laser Manipulation. J Biomed Opt 2015, 20, 115005.

12. Vo-Dinh, T.; Liu, Y.; Crawford, B.M.; Wang, H.-N.; Yuan, H.; Register, J.K.; Khoury, C.G. Shining Gold Nanostars: From Cancer Diagnostics to Photothermal Treatment and Immunotherapy; J Immunol Sci 2018; Vol. 2(1), 1-8.

13. Heinemann, D.; Kalies, S.; Schomaker, M.; Ertmer, W.; Murua Escobar, H.; Meyer, H.; Ripken, T. Delivery of Proteins to Mammalian Cells via Gold Nanoparticle Mediated Laser Transfection. Nanotechnology 2014, 25(24), 254101.

14. Bergeron, E.; Boutopoulos, C.; Martel, R.; Torres, A.; Rodriguez, C.; Niskanen, J.; Lebrun, J.-J.; Winnik, F.M.; Sapieha, P.; Meunier, M. Cell-Specific Optoporation with near-Infrared Ultrafast Laser and Functionalized Gold Nanoparticles. Nanoscale 2015, 7, 17836–17847.

15. Wang, S.; Huang, P.; Nie, L.; Xing, R.; Liu, D.; Wang, Z.; Lin, J.; Chen, S.; Niu, G.; Lu, G.; et al. Single Continuous Wave Laser Induced Photodynamic/Plasmonic Photothermal Therapy Using Photosensitizer-Functionalized Gold Nanostars. Adv Mater 2013, 25, 3055–3061.

16. Yao, C.; Rudnitzki, F.; He, Y.; Zhang, Z.; Hüttmann, G.; Rahmanzadeh, R. Cancer Cell-Specific Protein Delivery by Optoporation with Laser-Irradiated Gold Nanorods. J Biophotonics 2020, 13, 1–10.

17. Dacarro, G.; Taglietti, A.; Pallavicini, P. Prussian Blue Nanoparticles as a Versatile Photothermal Tool. Molecules 2018, 23.

18. Hoffman, H.A.; Chakrabarti, L.; Dumont, M.F.; Sandler, A.D.; Fernandes, R. Prussian Blue Nanoparticles for Laser-Induced Photothermal Therapy of Tumors. RSC Adv 2014, 4, 29729–29734.

19. Fu, G.; Liu, W.; Feng, S.; Yue, X. Prussian Blue Nanoparticles Operate as a New Generation of Photothermal Ablation Agents for Cancer Therapy. Chemical Communications 2012, 48, 11567–11569.

20. Hong, H.; Kim, M.K.; Lee, W.; Jeon, M.; Lee, C.; Kim, H.; Im, H.J.; Piao, Y. Injectable Biocompatible Nanocomposites of Prussian Blue Nanoparticles and Bacterial Cellulose as a Safe and Effective Photothermal Cancer Therapy. J Nanobiotechnology 2023, 21, 365.

21. T. Zhang.; M. Nishizawa.; T. Ishii.; Y. Miura, K. Motokawa.; H. Yoshikawa, T. Hasobe.; T. Nishimura.; Synthesis of uniform Prussian blue nanoparticles by a polyol process using a polyethylene glycol aqueous solution, RSC Adv., 2019, 9, 23668–23673.

Chapter 6: Conclusion

6.1 Summary

This thesis has comprehensively investigated a modular, laser-based approach for controlled cellular perforation, centering on the use of photoabsorbers with a combination of nanosecond pulse laser to induce either transient or permanent membrane perforation. The schematic in Figure 6.1 maps the design knobs to outcomes in our laser–material platform. The left panel lists the photoabsorber modality (surface micropatterns, gold nanostars, Prussian-blue nanocube clusters). The centre panel summarizes the key parameters for each modality—laser fluence with micropattern size/pitch, particle concentration, and stage velocity. Appropriate combinations yield reproducible biological responses, including membrane permeabilization for intracellular delivery, cell killing at higher energy loading, and spatially controlled delivery/patterning during scanning. The central hypothesis—that laser-activated photoabsorbers can be tailored to control the nature, location, and degree of cellular perforation—was validated through a sequence of experimental modules, each building upon the preceding ones.

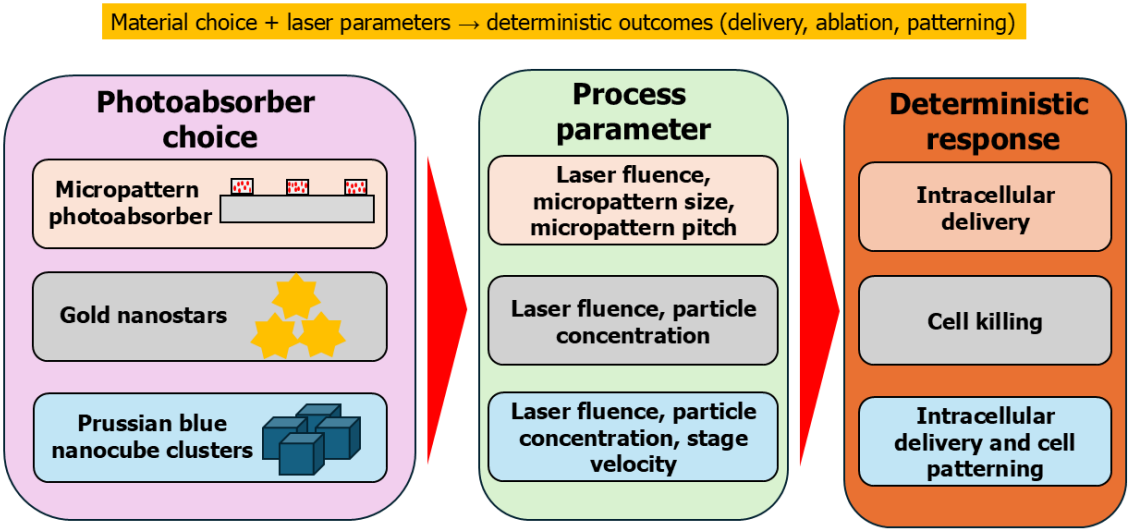

Figure 6.1 Material–Process–Response map for laser-induced bio-effects.

The journey began with the development of micropattern-assisted laser optoporation using pigmented SU-8 microdisks embedded with photoabsorbers. These micropatterns functioned as localized energy transducers, converting nanosecond laser pulses into spatially confined shockwaves, vapor nanobubbles, and localized heating. Chapter 2 focused on understanding the spatial dynamics of optoporation, revealing that micropattern geometry and laser parameters significantly influence pore formation, molecule diffusion, and cell viability. Smaller micropatterns (20 μm) allowed for more localized, high-viability delivery near the irradiation zone, while larger patterns (50 μm) offered broader perforation zones at the cost of increased necrosis. By analysing distance-dependent delivery profiles and accounting for shockwave propagation effects, we identified optimal zones for balancing delivery efficiency and cell survival.

These insights were further extended in Chapter 3, where a "micropattern-on-top" configuration was introduced to enable contactless intracellular delivery. This setup preserved the key advantages of spatial precision and scalability. Through systematic variation of micropattern pitch and laser fluence, we demonstrated a tunable window for achieving either efficient delivery or cell fragmentation. Specifically, smaller pitch values generated denser bubble fields, enhancing perforation at moderate fluences (~66 mJ/cm^2) and leading to cell damage at higher fluences (~100 mJ/cm^2). Notably, the delivery of FITC-dextran molecules of different sizes further highlighted the importance of matching pore size dynamics with cargo properties. Overall, Chapters 2 and 3 established a robust framework for transient, nanoparticle-free intracellular delivery using micropattern-based photothermal transduction.

Having established the feasibility of transient perforation via micropatterns, the thesis transitioned toward permanent perforation for cell ablation in Chapter 4. Here, we introduced gold nanostars (GNS) as potent photothermal transducers capable of mediating cell death via

nanosecond pulsed laser irradiation. Unlike micropatterns, GNS offered the advantage of solution-based, uniform distribution across cell monolayers, making them ideal for photothermal therapy (PTT) applications. Their branched geometry and strong plasmonic resonance in the visible range resulted in localized heating effects far superior to spherical counterparts, as validated by COMSOL simulations.

Experimental studies confirmed that the extent of cellular damage could be precisely tuned by varying GNS concentration and laser fluence. At high concentrations and fluences, the rapid formation and collapse of vapor nanobubbles led to irreversible membrane rupture and cellular detachment. The system demonstrated high-throughput capabilities through raster scanning, achieving targeted ablation in HeLa, SAOS-2, and HEK-293 cells with minimal off-target effects. This phase of the study marked a critical shift from reversible membrane disruption to intentional, spatially resolved cell killing, laying the groundwork for therapeutic applications in oncology.

While gold nanostars proved effective, their high cost and regulatory hurdles limited scalability. To address this, Chapter 5 explored the use of Prussian Blue Nanocube Clusters (PBNCCs) as a low-cost, biocompatible alternative photoabsorber. These clusters offer several advantages: ease of synthesis, and minimal cytotoxicity. We hypothesized that PBNCCs could replicate the dual functionalities—transient perforation for delivery and permanent perforation for ablation—at a fraction of the cost.

Indeed, under optimized conditions, we achieved up to 63% delivery efficiency of FITC-dextran 4 kDa in HeLa cells with negligible cytotoxicity. Raster scanning of PBNCC-treated monolayers also enabled precise cell patterning. Through parameter optimization, we achieved reproducible patterns across varying target widths.

Moreover, analyses of the formed patterns confirmed high precision and dimensional accuracy, making this approach suitable for spatial cell manipulation in biofabrication and tissue engineering. These results affirm that PBNCCs can serve as a dual-function photoabsorber for both intracellular delivery and cell ablation.

Taken together, the progression from micropatterns to gold nanostructures and finally to Prussian Blue nanoclusters represents a deliberate and strategic expansion of laser-assisted cellular manipulation. This thesis has shown that the degree of membrane perforation—transient vs. permanent—can be finely controlled by modulating photoabsorber type, laser energy, and irradiation dynamics. Whether the goal is to gently deliver therapeutic molecules or to ablate diseased cells, this platform offers modular flexibility, high spatial resolution, and scalability.

From a mechanistic standpoint, all approaches converged on a common physical basis: laser-triggered thermal and mechanical phenomena such as bubble generation, shockwave emission, and localized heating. These biophysical effects were harnessed differently across applications: transient perforation (Chapters 2 and 3) focused on enabling intracellular entry while maintaining cell viability, whereas permanent perforation (Chapters 4 and 5) aimed to disrupt membranes irreversibly for targeted ablation.

Beyond demonstrating individual techniques, this study contributes a design framework for future laser-based biomedical systems. The tunable interplay between materials, laser parameters, and biological outcomes enables optimization for specific clinical or research needs. Moreover, the transition to cost-effective materials like PBNCCs paves the way for practical implementation in resource-limited settings.

In conclusion, this thesis explores the following photoabsorber-assisted site-specific cell perforation methods, which are explored by investigating various photoabsorbers with different features for applications of intracellular delivery, photothermal therapy, and cell patterning. The concise comparison of various methods explored can be found in the following Table 6.1:

Table 6.1 Comparison of features of photoabsorber-assisted cell perforation methods

Research dimension	**Chapter 2-3**	**Chapter 4**	**Chapter 5**
Material platform	SU-8/PR-254 micropatterns	Gold nanostars	Prussian blue nanoparticles
Cost consideration	Moderate (fabrication)	High (gold-based)	Low (cost-effective)
Application scope	Intracellular delivery focus	Cancer therapy focus	Versatile dual-purpose
Technical complexity	High (fabrication)	Moderate (synthesis)	Low (simple preparation)
Scalability	High (parallel processing)	Moderate (targeted therapy)	High (programmable patterning)

6.2 Future Works

This research lays the groundwork using photo absorbers with nanosecond pulsed lasers for combined biomedical applications, which require high spatial precision and scalability. For example, the micropattern-assisted single pulse optoporation method can be utilized to deliver foreign molecules into cells at a specific site, and the cellular interaction with cells without intracellular delivery can be studied using advanced imaging techniques.

The high-throughput cell irradiation with micropatterned substrate will be utilized in the combined treatment of cancer tumors by performing intracellular delivery of tumor antigens

and photothermal therapy of tumors in parallel, so that upon laser irradiation, the remaining cells also get eliminated with tumor antigens to stop the recurrence of cancer tumors.

We plan to extend the gold nanostars-assisted method, combining it with 3D spheroid models instead of conventional monolayers. We plan to study the 3D tumour ablation, which mimics the structure of human organs more closely than conventional cell monolayer culture.

We plan to apply the Prussian blue-assisted photoabsorber method in a combined application where cells with very high delivery efficiency are required. We plan to perform intracellular delivery at our specific site of interest and eliminate the cells at the site where molecules have not been delivered.

Together, in the future, we aim to contribute towards the advanced integration of laser-based biotechnologies with next-generation therapies in cancer treatment, regenerative medicine, and cell engineering.

Publication List

International Journal Articles

1. Mishra, A.; Inaam, R.; Okamoto, S.; Shibata, T.; Santra, T.S.; Nagai, M.; Visible Pulsed Laser-Assisted Selective Killing of Cancer Cells with PVP-Capped Plasmonic Gold Nanostars. Micromachines (Basel) 2023, 14(6), 1173.
2. Mishra, A.; Okamoto, S.; Shibata, T.; Santra T. S.; Ryu, S.; Nagai, M.; Distance-Dependent Spatial Analysis of Micropattern-Generated Shockwave for Cell-Type Specific Intracellular Delivery. Biomed Microdevices 2025, 27, 30.

International Conference

1. Mishra, A.; Nagabhoosnam, S.; Okamoto, S.; Shibata, T.; Santra T. S.; Ryu, S.; Nagai, M.; Prussian Blue Nanocube Clusters for Pulsed Laser Optoporation of Cells, IEEE-NEMS, Paper ID: 7272, Kyoto, May 2024.

Acknowledgement

I would like to express my deepest gratitude to the following individuals and institutions for their invaluable support throughout my research journey.

I would like to express my sincere gratitude to Professor Moeto Nagai for accepting me as a student under his esteemed guidance. Without his continuous support, this thesis would not be possible. He is not only a great researcher, but also an excellent human being. I am very fortunate to receive his exceptional guidance.

I sincerely thank my thesis committee members, Professor Takayuki Shibata and Professor Tadaharu Adachi, for their insightful comments and feedback during my graduation defense process.

My heartfelt appreciation goes to my project mates Hirofumi Yamamoto, Yohei Kanamori, Kubo Tomohiro, and all my current and former lab mates for their assistance with experiments.

I am grateful to Toyohashi University of Technology for providing this wonderful opportunity to continue my research, and to the Amano Institution and other funding agencies for their financial support.

I would like to thank my family and friends for their unwavering emotional support during my research in Japan.

Aniket Mishra

Submission Date: 2025/07